### 3.6. Structure Determination of Near Surface Layers by DCEMS

The application of DCEMS requires the use of scatterers whose properties are well known and stable. These requirements are met by the iron and stainless steel system which is widely used in CEMS. A feature of DCEMS is its capacity to study layers which are thinner than in CEMS. This results in a low count rate

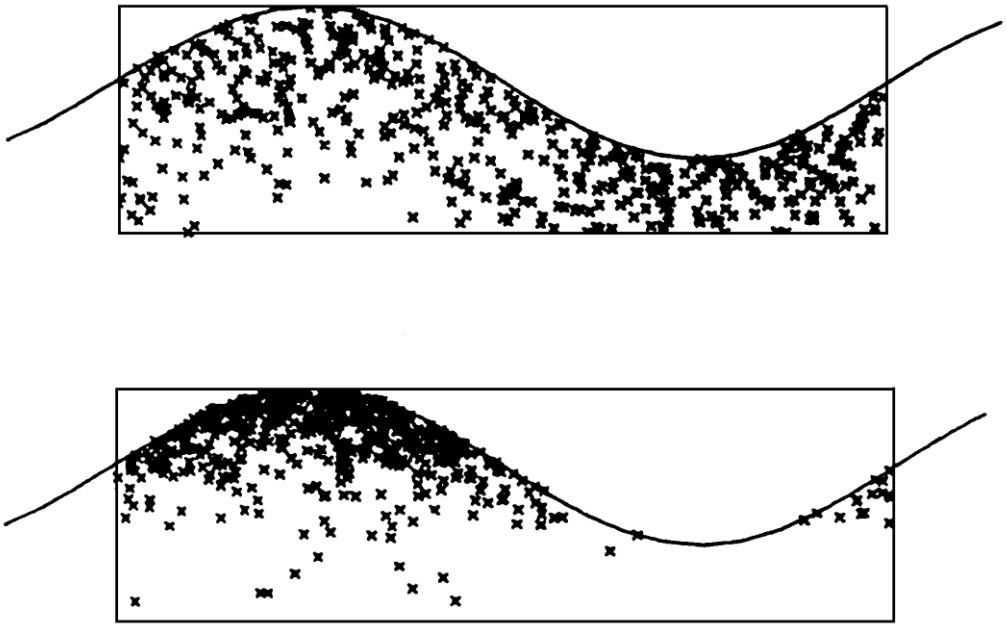

Fig.3.37 Cut through a (Å = 100, W = 1000) surface along the y = W/4 plane, showing computer-plotted starting points of the 7.3 keV electrons emerging with energy losses < 100 eV to normal ($0^\circ < \theta < 37^\circ$, upper figure) and into glancing angles ( $79^\circ < \theta < 90^\circ$), lower figure (from [3.18]).

of the order of several counts/sec and puts a higher demands on the scatterers used in DCEMS. The surface of the stainless steel backing should be highly polished and the iron evaporation be thoroughly controlled. The enrichment in the resonant isotope of both the surface layer and the backing is usually high. An essential parameter is the effective density $n_{eff}^{i}$ of Mőssbauer atoms in a given phase. For most of these standard scatterers the ratio of $n_{eff}^{Fe}$ values for $\alpha$-Fe to $n_{eff}^{ss}$ values for stainless steel is in the range 1.70 - 1.85.

Consider now the spectra from two typical standard scatterers with iron layer thicknesses of 360 A| and 210 A| (Fig.3.38). It is natural to expect the signal from $\alpha$ -Fe for the first scatterer to be larger than for the second one. This is confirmed by Fig.3.38 if the spectra obtained at a β-spectrometer energy setting for the detection of electrons that have lost a significant fraction of their energy are compared. At a spectrometer setting for the detection of electrons with energies close to that of K-conversion electrons, one could expect that the signal from the iron layer 360 A| thick (see Fig.3.38a) would be further increased in comparison with the fraction from the 210 Å thick layer (see Fig.3.38b). However, the opposite result is observed. The reason for this is in the different energy resolution of the spectrometers used to record the spectra. Thus, it is evident that without sufficient information on the weight functions a correct interpretation of experimental data is hardly possible.

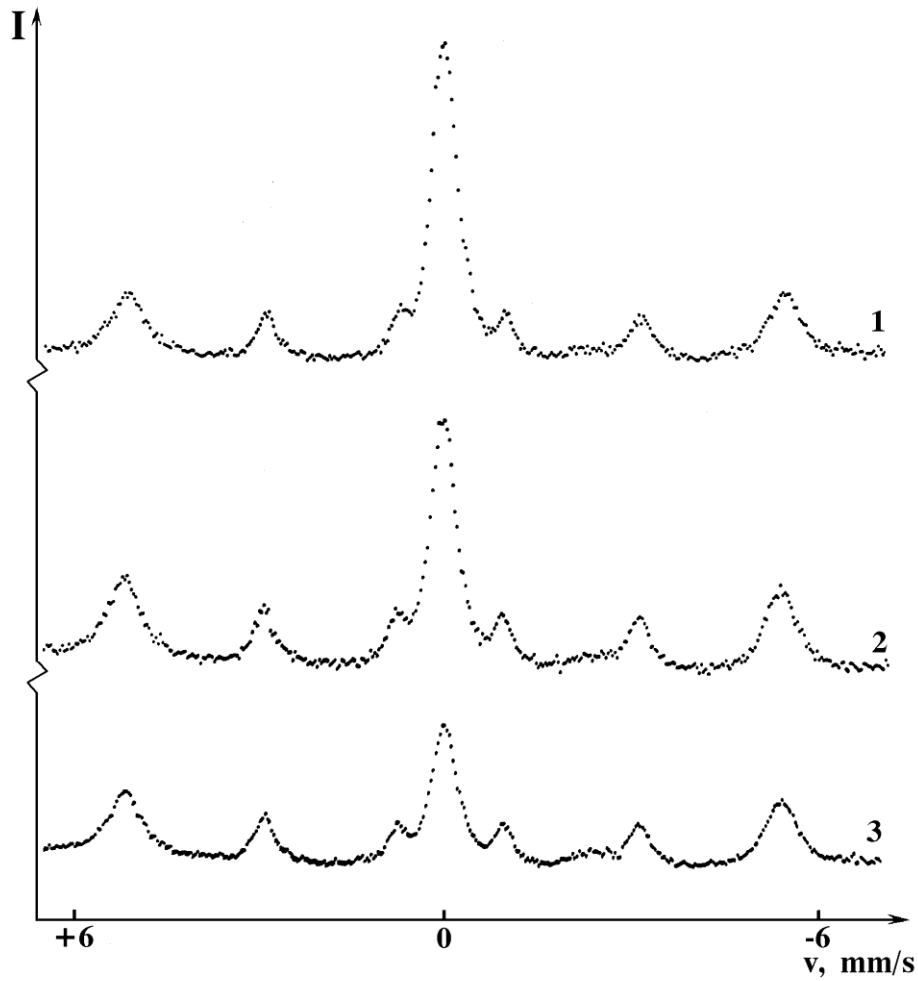


Fig.3.38a DCEMS spectra from a stainless steel scatterer (a = 90 %) covered with an iron layer (a = 90 %) d = 360 Å; β-spectrometer with θ = 45°, R = 8 % at three energy settings: 1 - 6.80 keV; 2 - 7.04 keV; 3 - 7.30 keV (from [3.43]).

In addition to the $T_V(x)$ weight functions, the instrumental line profile of the spectrometer (see Sect.3.4) should be known. In order to determine $S'(V,E)$, areas are measured under the spectra (which are normalized to the same measuring time) as a function of the energy of detected electrons (i.e. the V parameter). An instrumental line profile is given in Fig.3.39 which was obtained in the following procedure [3.83]. A layer of $\alpha$-$^{57}$Fe 30 ± 5 Å thick was evaporated onto an epitaxial film of $\alpha$-$^{56}$Fe 1200 Å thick on a LiF backing with a (100) orientation. The Mőssbauer spectrum shape from this layer did not differ from that of the bulk. The area under the spectrum may be described by the expression

$$A_{\theta,V} \simeq \int_0^{30\ \text{Å}} T^K_{\theta,V}(x)\, dx \,. \qquad (3.51)$$

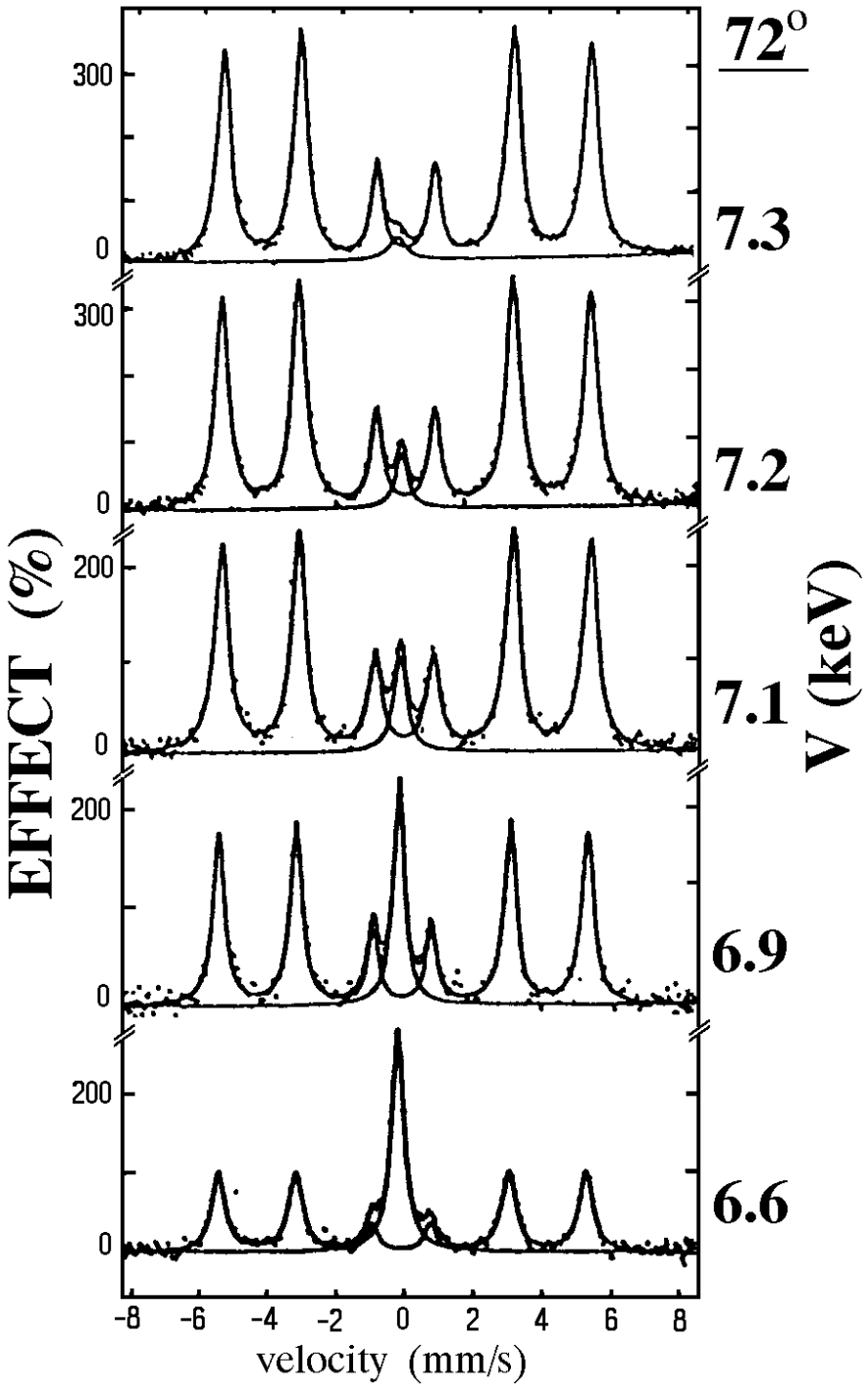


Fig.3.38b DCEMS spectra from a stainless steel scatterer (a = 90 %) covered with an iron layer (a = 90 %) d = 210 A|; θ = 72°, R = 2.7 %; at five energy settings: 1 - 6.6 keV; 2 - 6.9 keV; 3 - 7.1 keV; 4 - 7.2 keV; 5 - 7.3 keV (from [3.83]).

The $T_{\theta,V}^{K}(x)$ functions are given in [3.83] with the angle θ used to obtain the $S'(V,E)$ dependence of Fig.3.39 being 15° ± 6°.

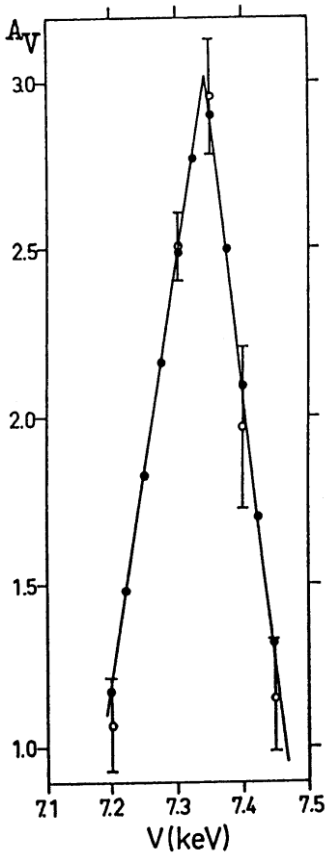


Fig.3.39 Experimental (open circles) and theoretical (closed circles) DCEMS signal $A_{\theta,v}$ vs. spectrometer setting V for θ = 15° ± 6° (from [3.83]).

The resonant layer thickness in this case is so small that electron energy losses may be neglected and the layer may be considered an ideal source of K-conversion electrons. The photoelectrons emitted by the α -$^{56}$Fe layer are also detected by the spectrometer but they do not make a significant contribution to $A_{\theta,V}$. Hence the experimentally observed $A_{\theta,V}$ values accurately reproduce the $S'(V,E)$ function for the 7.3 keV electrons. The energy resolution of the spectrometer, defined as the full width at half maximum, is 2.7 % which is somewhat worse than the previously reported value [3.61]. The $S'(V,E)$ function is practically independent of θ and allows the computation $T_{V,\theta}^{K}(x)$ for different values of θ by using the experimentally obtained $S'(V,E)$ function [3.83].

The depth sensitivity of DCEMS is affected by the average angle value within which electrons are collected. The effect is demonstrated by the spectra shown in Fig.3.40 which was obtained by detecting electrons of the same energy but at different angles to the surface.

Comparison of the spectra shown in Fig.3.38a with those of Fig.3.40 ($\theta = 46^{\circ}$) illustrates the role of the energy resolution of β-spectrometers.

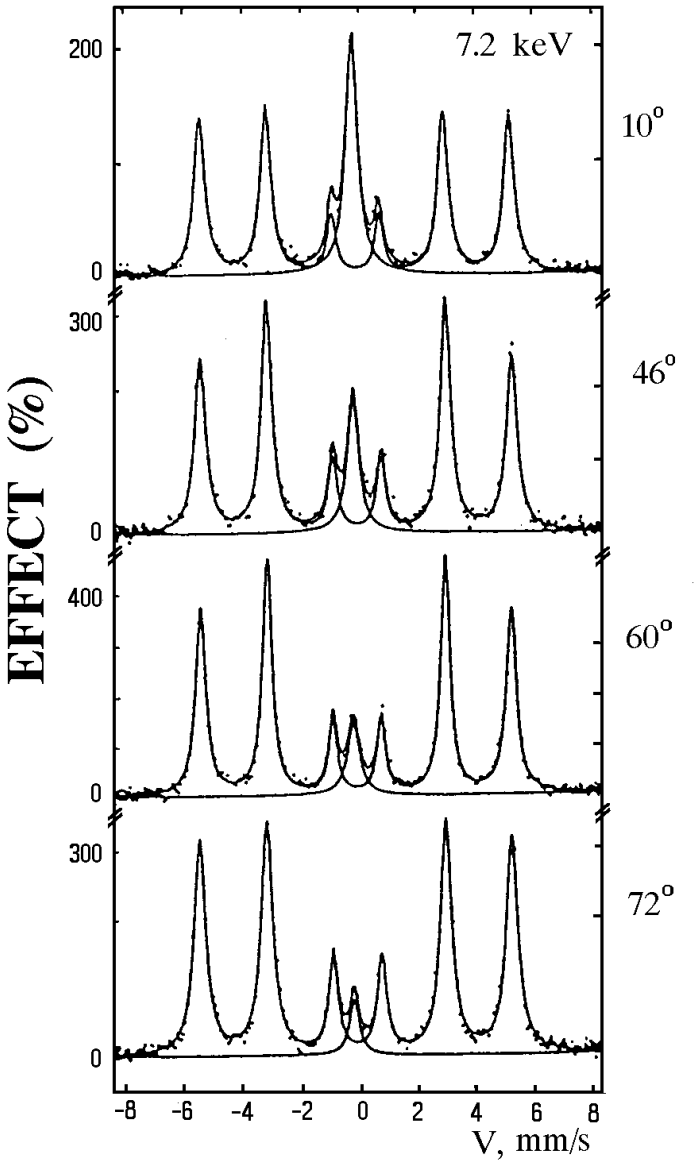


Fig.3.40 DCEM spectra at the electron-energy setting V = 7.2 keV from the same scatterer as in Fig.3.38 a but for electron- emission angles $\theta = 10^{\circ}$, $46^{\circ}$, $60^{\circ}$ and $72^{\circ}$ ; R = 2.7 % (from [3.83]).

It is now necessary to consider the analysis of (3.50) which describes the Mőssbauer spectrum shape from the bulk sample. Assume that Mőssbauer radiation is normally incident to the sample surface. Since the thickness of the analyzed layer in DCEMS is small, the incident γ-radiation may be assumed to be almost unattenuated in this layer.

It follows from Sect.3.2 that if this thickness is less the 700 Å then, even at a = 90 %, the only deformation of the spectrum shape might be a small departure of the line intensity ratios from 3 : 2 : 1 : 1 : 2 : 3. This results from the change of spectral composition of Mőssbauer radiation when penetrating into the sample. Evaluations show also that electrons detected in the spectrometer may be considered to appear due to K-shell internal conversion only. It follows that $T_V(x) = T_V^K(x)$ and the spectrum shape may be written as [3.9,84-86]:

$$I_V(v) \sim S_K(v) \int_0^\infty T_V^K(x)\, dx = S_K(v)\, U_V^K(\infty) \ . \qquad (3.52)$$

$I_V(v) \sim S_K(v)\ 1T_V^K(x)\ dx = S_K(v)\ U_V^K(\infty)$ . (3.52)

Mőssbauer atoms in the near surface layer may be in different phases (environments). Assume that the number of such phases (and of respective partial Mőssbauer spectra $I_{V,j}(v)$) equals N(j = 1...N). The expression for the shape of the Mőssbauer spectrum from such a scatterer (provided that the total spectrum is a superposition of the partial spectra) may be written in the following form:

$$I_V(v) = \sum_{j=1}^{N} C_j S_{K,j}(v) \int_0^\infty T_V^K(x)\, K_j(x)\, dx \ , \qquad (3.53)$$

$I_V(v) = 2\ C_j S_{K,j}(v)\ 3T_V^K(x)\ K_j(x)\ dx$ , (3.53)

where $C_j$ is a constant.

The $K_j(x)$ function determines the fraction of the sample area which at a depth x consists of j phase. All quantities in (3.53) are known, except the $K_j(x)$ functions. The purpose of DCEMS is to obtain the phase distribution in the sample. To obtain the $K_j(x)$ functions from experimental data it is necessary to record not less than N spectra at different parameter V values and to find the $A_{j,V}$ areas under the spectrum of each phase. In order to find $A_{j,V}$,(3.53) is integrated over v

$$A_{j,v} = C\, n_{eff}^j \int_0^\infty T_V^K(x)\, K_j(x)\, dx \ , \qquad (3.54)$$

$A_{j,v} = C\ n_{eff}^j\ 4T_V^K(x)\ K_j(x)\ dx$ , (3.54)

where $n_{eff}^j = 1$ for an α-F scatterer; for the j-th phase $n_{eff}^j = f5N_j/(M_j\ f6_e)$, where $M_j$ is the formula weight of the compound divided into the atomic weight of iron; $N_j$ is the number of iron atoms in the formula, C is a constant which is the same for each phase and for all V values.

Mőssbauer signals $A_{j,V}$ obtained by (3.54) give a certain dependence $L_j(V)$, which may be called the resonant profile of the j-th phase (at N = 1 and $d \to 0$ $L_j(V)$ transforms into $S'(V,E)$). Thus, an integral equation is obtained which relates the resonant profile of the given phase to the depth distribution of that phase. The weight function may be presented as an operator to find the $K_j(x)$ function.

$$T^{K}_{op}\ (K_j(x)) = L_j(V) \quad . \tag{3.55}$$

Taking the $L_j(V)$ function from the experiment one can perform the inverse transformation:

$$K_j(x) = T^{-1}_{op}\ (L_j(V)) \ .$$

Taking the $L_j(V)$ function from the experiment one can perform the inverse transformation:

This approach does not require any a priori assumptions and allows each phase to be investigated independently. However, it requires highly accurate statistical measurements. The $L_j(V)$ function is obtained as a histogram with a small number of points. It restricts the method substantially and has not found wide practical application.

Another approach is of more practical importance. In this approach the sample is treated as an entirety, and the signals from all phases are taken into consideration together. A consistency is required of the results for a particular spectrometer setting V and within a series of V values. To appreciate the approach a model of the absorber must be introduced which may be accepted or discarded depending on whether it can be reconciled with the measured data. The simplest model is the one where the j-th phase constitutes a layer spreading from depth $d_{j-1}$ to depth $d_j$. The signal from this phase may be written by means of the U-functions:

$$A_{j,V} = C\, n_j^{}{}_{eff}\ [U_V(d_j) - U_V(d_{j-1})] \ ,$$

$$U_V(d) = \int_0^{\infty} U(d,E)\ S'(V,E)\ dE \ , \tag{3.56}$$

where U(d,E) refers to a layer of thickness d and a very good resolution of the spectrometer [3.86].

Let us take an $\alpha$-Fe plate whose CEM spectrum also shows the presence of $\gamma$ -iron. In a general case we could neither determine the amount of this phase nor its distribution on the sample surface. Let us place the sample in a DCEM spectrometer

[3.9,85], calculate the $U_V(x)$ functions for three parameter V values (Fig.3.41), and from the three corresponding Mőssbauer spectra determine the experimental values of Mőssbauer signals $A_V$ and $A_V'$ for $\alpha$ -Fe and $\gamma$-Fe, respectively (Table 3.4). A simple

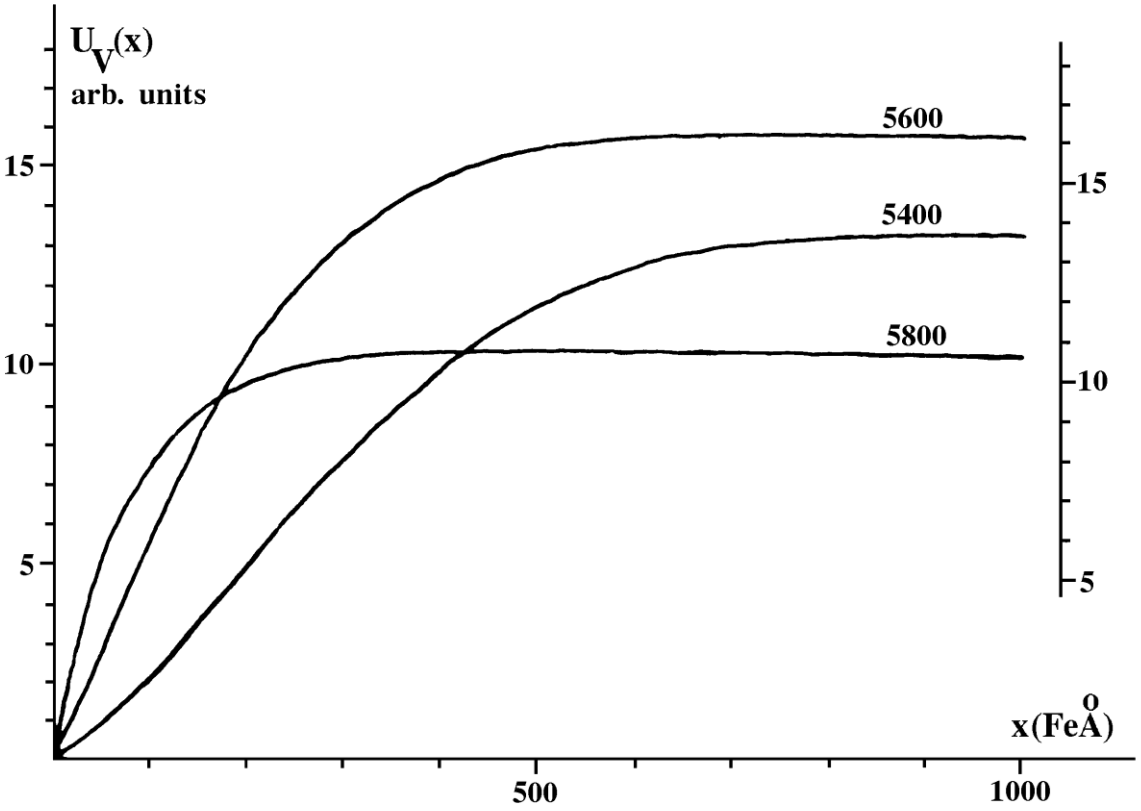


Fig.3.41 $U_V(x)$ functions computed for V = 5800 V, 5600 V and 5400 V. C = 0.796 (from [3.9]).

model assuming a continuous thin $\gamma$-Fe layer allows the thickness of the layer to be found from a single measurement by means of the relation:

$$A_V' = C\, n_{eff}'\,[U_V(\infty) - U_V(d)] \,, \qquad (3.57)$$

$A_V' = C\, n_{eff}'\,[U_V(\infty) - U_V(d)]$ , (3.57)

since the $U_V$ functions are known and given in Fig.3.41. The d values, thus obtained for the three parameter V values, are quite different. It means that the near surface layer is of a more complex structure which will be described by a continuous K(x) function satisfying the condition $0 \le K(x) \le 1$.

Generally, an inert region may be present, which does not produce a detectable Mőssbauer signal. If the $K_0(x)$ function refers to the fraction of this region, then for any cut through the sample at a depth x, the following relation pertains:

$$K_0(x) + \sum_{j=1}^{N} K_j(x) = 1 \,. \qquad (3.58)$$

Table 3.4
Experimental and calculated values of Mőssbauer signals from austenite ($A_V'$) and ferrite ($A_V$) phases.

| Electron energy, eV | $U_V(\infty)$ | C | $A_V'$ | | $A_V$ | |
|---|---|---|---|---|---|---|
| | | | experimental | calculated | experimental | calculated |
| 7.300 (*V*=5800 V) | 10.6 | 0.0919 | 0.18 | 0.17 | 0.79 | 0.80 |
| 7.050 (*V*=5600 V) | 16.1 | 0.0901 | 0.17 | 0.18 | 1.28 | 1.29 |
| 6.800 (*V*=5400 V) | 13.6 | 0.0919 | 0.11 | 0.09 | 1.14 | 1.15 |

By means of (3.54), (3.56) and (3.58) the relation which is known as a sum rule [3.9] can be obtained

$$C = \frac{\sum_{j=1}^{N} A_{j,V} / n_{eff}^{j}}{U_V(\infty) - \int_0^{\infty} T_V(x)\, K_0(x)\, dx} . \qquad (3.59)$$

If there are no inert ("unidentified") regions present, then the sum rule becomes

$$C = \frac{1}{U_V(\infty)} \sum_{j=1}^{N} A_{j,V} / n_{eff}^{j} . \qquad (3.60)$$

Returning to the case of a small amount of an austenite phase on top of a ferrite phase, assume now that $\alpha$-Fe covers only a part K of the sample surface down to a depth d (the rest is $\alpha$ -Fe). Signals from the two phases may be described by the expressions

$$A_V' = C\, K\, n_{eff}'\, U_V(d) , \qquad (3.61)$$

$$A_V = C\, n_{eff}^{Fe} [U_V(\infty) - K\, U_V(d)] \qquad (3.62)$$

Here $n_{eff}^{Fe}$ may be taken to be equal to $n_{eff}'$ and to unity. To find d and K the following procedure is used. The constant C is determined and the sum rule is checked (The values of $U_V(\infty)$ and the experimental values for the signals from the two phases

together with the C parameters are given in Table 3.4). The mean value of C is 0.0912. The good agreement between the C values and the mean indicates that there is no inert region. From the U functions (Fig.3.41) a d value is to be found to satisfy the relation

$$A'_{V_1} / A'_{V_2} = U_{V_1}(d) / U_{V_2}(d) \quad . \tag{3.63}$$

Knowing d and the corresponding $U_V(d)$ value, K can be found using (3.61) and substituted into (3.62) to check the consistency of the results. The values of d which are obtained from three ratios (3.63) (see Table 3.4) are somewhat different. The best agreement is for d = 200 Å and K = 0.19. The $A_V$ values calculated for these parameters by means of (3.61) and (3.62) are also given in Table 3.4. The consistency is better if the austenite phase is envisaged as a pyramid as opposed to a rectangular block. The practice is achieved by a computerized search for a least-squares fit. Various techniques to determine the near-surface structure together with computer programs and particular examples are given in [3.87].

It is more difficult to investigate samples when inert regions are present. However, DCEMS allows the surface structure to be determined. Thus, by a thorough analysis of DCEM spectra from iron foils (a = 90 %) cold-rolled to a thickness of 25 μm and annealed at 900° C for six hours in an hydrogen atmosphere and subsequently exposed to air for several months, no signs of extraneous phases were detected (see Fig.3.42a and b). In contrast ESCA spectra have shown the presence of ferric ions and OOH-groups, but no lines of $\alpha$-Fe (see Fig.3.43) [3.88]. This means that the upper layer is inert, at least at room temperature.

The weight functions for the experiment are presented in Fig.3.44. The electrons emerging from the layer 20 A| thick (which is equivalent to the inert layer from the ESCA measurement) constitute the major part of the signal, especially when the spectrometer setting is 7.3 keV. This would be much more if the energy resolution of the spectrometer could be improved. With the spectrometer used in [3.88] a resonant layer about 10 A| thick was observed.

The inert layer should cause a damping effect. This may be considered as a subtraction of the signal produced by the resonant layer as thick as the inert one from the total signal. Since the electron beam from a very thin surface layer mainly determines the total beam of the 7.3 keV electrons, the subtraction of this signal as shown in Fig.3.44, will shift the centre of gravity of the weight functions towards larger depths as well as the instrumental line $S'(V,E)$ maximum to the lower V region.

The shift of the instrumental line may be evaluated approximately. The stopping power for the 7.3 keV electrons in

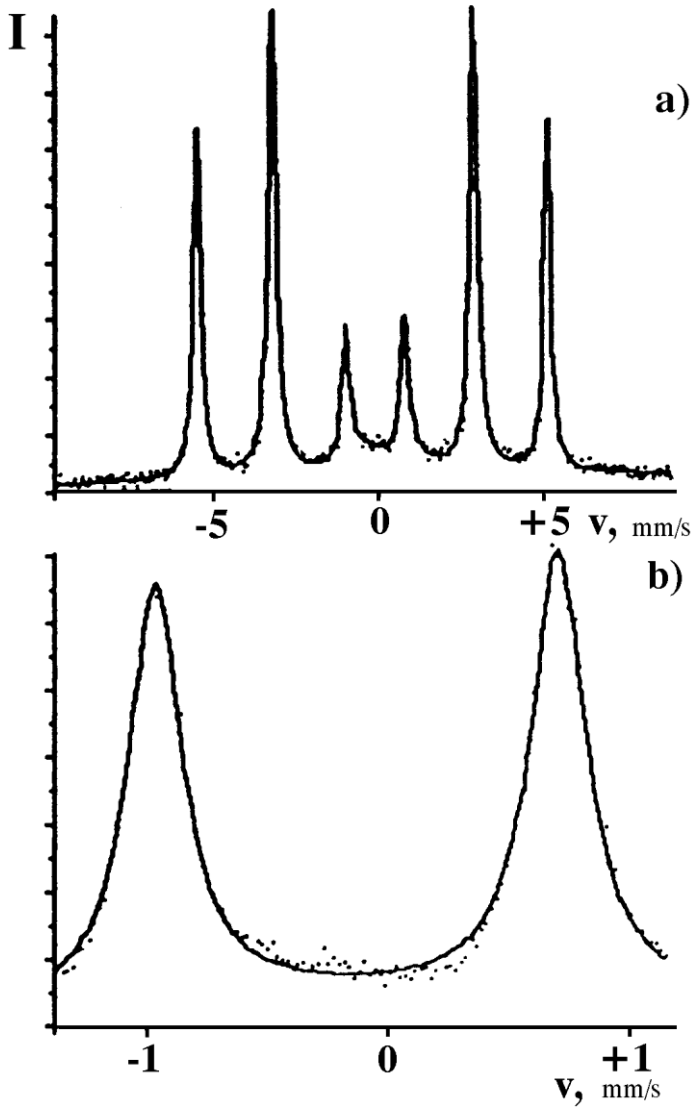


Fig.3.42 DCEM spectra from $\alpha$ -$^{57}$Fe (a = 90 %) prior to reduction. The β-spectrometer ( $\theta = 45^{o}$, R = 2.8 %) is set to detect the 7.3 keV electrons. The spectrum B shows the two innermost lines (3 and 4) of the α-iron spectrum (from [3.88]).

$\alpha$ -Fe is ca. 1.4 eV/ Å. A layer 20 Fe Å thick will cause an energy loss of nearly 30 eV, and a shift of the line profile by V = 0.796·30 V = 24 V (C = 0.796).

Annealing the sample in the spectrometer at 600°C for one hour in hydrogen ($10^{-3}$ Torr) resulted in the removal of the inert layer and in a shift of the line profile towards higher V values. No extra lines appeared in the Mőssbauer spectra. The instrumental lines obtained before and after reduction in hydrogen are seen to be crossing since annealing in a hydrogen atmosphere causes the signals occurring at lower V values to

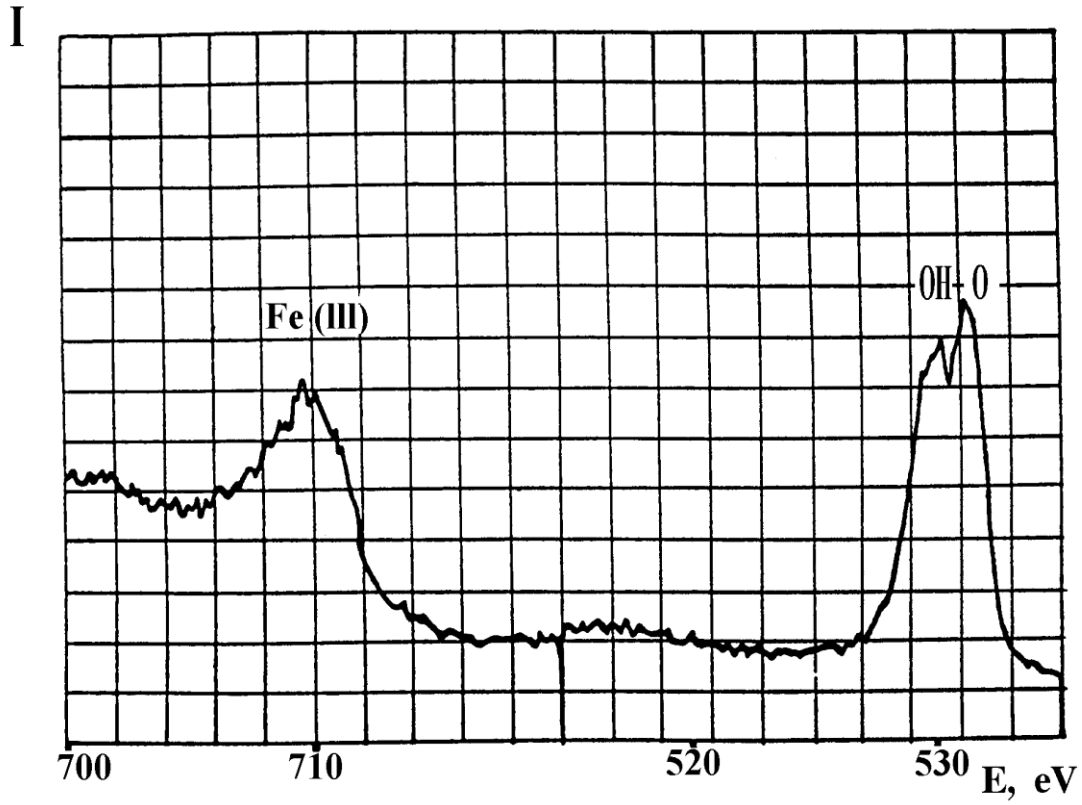


Fig.3.43 ESCA spectrum of an $\alpha$ -$^{57}$Fe foil, whose DCEMS spectra are in Fig.3.42.

decrease. The decrease is caused by the change of the signal from the bulk rather than from the surface layer which makes a negligibly small contribution to the weight function. A comparison of the Mőssbauer line widths shows that after reduction in hydrogen the lines become narrower indicating that the sample becomes more homogeneous. The best agreement between the calculated and experimental results is achieved when the inert layer thickness is (25 ± 10) Å.

In all the considerations described above the progress in DCEMS has been linked with the availability of β-spectrometers with better energy resolutions at fairly good luminosity. At an energy resolution of 2 % to 3 %, a depth resolution of about 20 Å for a layer less than 150 Å, and of better than 100 Å for deeper layers can be achieved. The energy resolution of 0.5 % allows a detailed investigation of the upper layer of about 30 A| thickness, although the measuring time increases considerably.

DCEM spectra obtained by detecting the 7.3 keV electrons at glancing angles allow a near-surface layer several tens Ängstrom thick [3.82] to be examined. The same 10 A| may also be studied by detecting the ≅ 590 eV Auger electrons leaving normal to the sample surface [3.89]. By using a β-spectrometer for separating the line of secondary electrons (E < 50 eV) from the total spectrum, and energy selecting within the line width, the signal produced in a layer 10 to 20 A| thick can be identified [3.62]. High vacuum and thoroughly cleaned surfaces are necessary for studies of such thin near-surface layers.

When the analysis of such thin layers is not required,

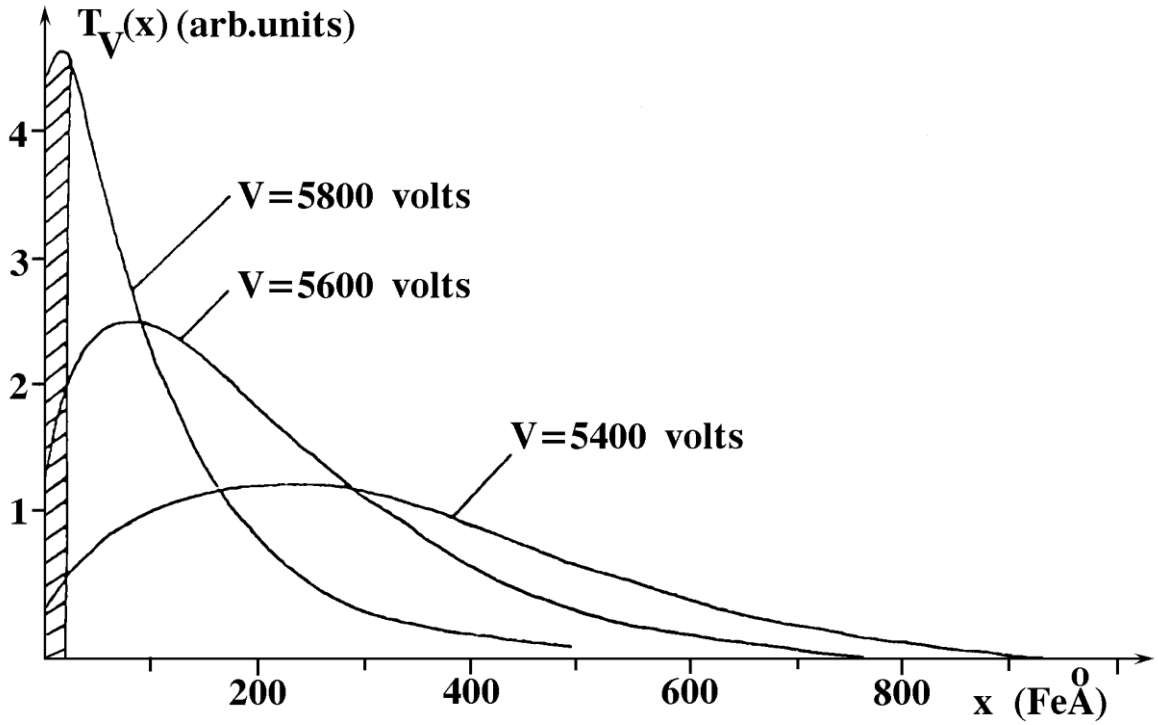


Fig.3.44 Weight functions $T_V(x)$ for the same spectrometer settings V as in Fig.3.41. The shaded area indicates the contribution to a spectrum measured at V = 5800 V from the outermost 20 FeA| (from [3.88]).

DCEMS can be developed in another way. This is related to a sharp increase of the spectrometer luminosity and hence to the reduction of measuring time required to reach a specified statistical accuracy. An example is a DCEM spectrometer (Fig.3.45 [3.72]) using a non-dispersive electrostatic analyzer consisting of an elliptical mirror and a spheric retarding grid which are confocal. Electrons with an energy less than E = Ue (eV) (see Fig.3.45) which are emitted by the sample placed near to the focus of the elliptical mirror, are focused onto the detector entrance window near the second focus. The applied voltage V and the voltage difference ΔV between the mirror and retarding grid determine the energy interval within which the electrons reach the detector. An elliptical grid in front of the mirror and spherical grids around the retarding grid are ground and serve to screen the sample and detector from any electric fields.

Although the mirror should collect electrons emerging in the solid angle of 2π, the grids reduce the transmission to 35% of 2π. Mőssbauer radiation through a beryllium window enters the spectrometer chamber where the operating pressure is $\cong 10^{-11}$ Torr. The energy resolution is about $\cong$ 9 % at the sample and the detector entrance window diameter is about 10 mm. It is also possible to work in the integral mode at energy settings for detection of LMM-Auger electrons. The spectrometer is a part of the "combine" [3.72] incorporating several instruments for surface studies. The weight functions computed by Liljequist et al. [3.79] for R = 8 % and θ = 45° may be used to interpret the spectra recorded by the spectrometer.

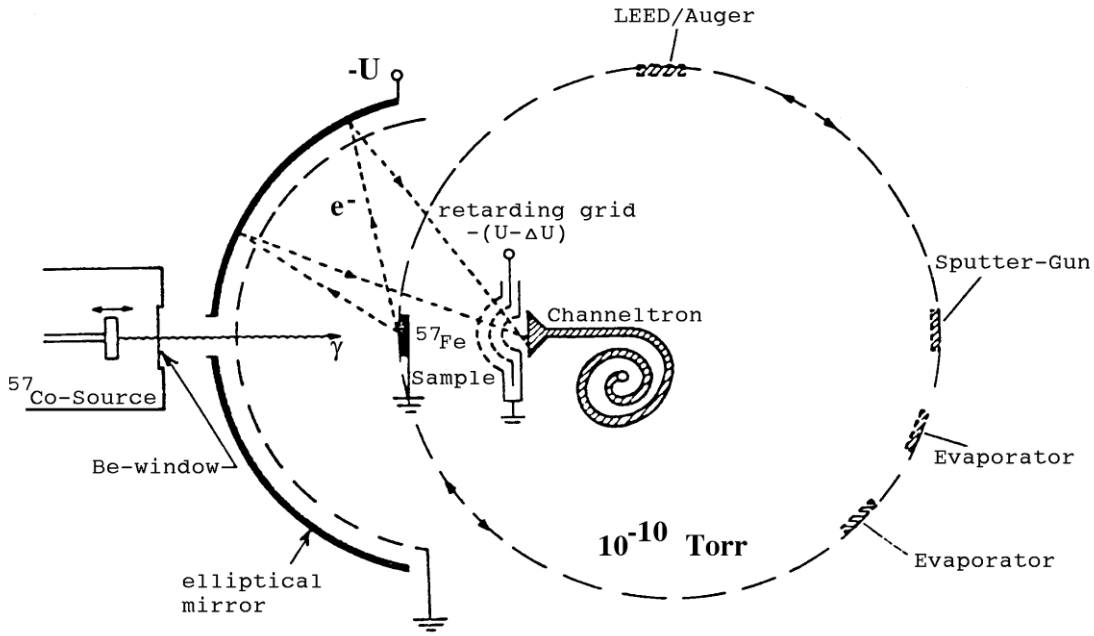


Fig.3.45 DCEM spectrometer based on a non-dispersive electrostatic analyzer (from [3.72]).

An alternative way to reach a depth selection in DCEMS involves a simplification of the technique and the use of other detectors of electrons such as the gas-filled proportional counters.

### 3.7. Proportional Counters as Electron Detectors in CEMS

The development of CEMS as an independent analytical method is connected with the use of gas-filled proportional counters for the detection of electrons (see e.g. [2.72, 74; 3.90-119]). Figure 3.46 illustrates the operating principle of such a CEM spectrometer. The proportional counter in CEMS detects all the electrons in the energy interval from about 1 keV up to the Mőssbauer transition energy. The counters designed earlier were revised and new designs and operation models were developed. In addition to the high efficiency, the proportional counters have an energy resolution allowing a certain depth selectivity to be obtained.

Electrons emitted from the sample surface under investigation (see Fig.3.46) ionize the gas filling the active counter volume. The ionization process will last until the energy of primary electrons and secondary electrons becomes less than the ionization potential of molecules and atoms of the gas mixture, or until the electron leaves the active counter volume. Electrons and positive ions move to the corresponding electrodes. The electric field at the anode is so strong that every primary electron produces an avalanche of electrons and

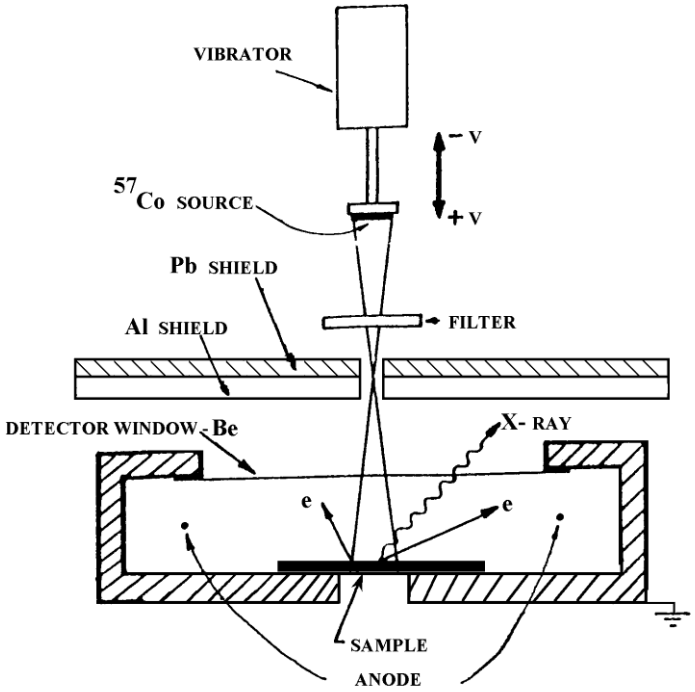


Fig.3.46 Schematic picture of a spectrometer for backscattering studies.

positive ions (secondary ionization). The number of electrons per initial ion pair is the gas multiplication factor (M). In proportional counters this factor may vary from 10 up to $10^5$.

During an avalanche, excitation of molecules can lead to the emission of photons. If the photons reach the counter walls they eject electrons and start a new avalanche. The avalanche will spread along the entire counter and become independent of the primary ionization. The same undesirable effect may also be caused by positive ions hitting the cathode to give secondary electron and photon emission.

There are two methods to suppress the secondary electron emission and quench the discharge: (i) the addition of a quench gas to the main filling gas, (ii) the use of special circuits. In CEMS the former method is usually used. In proportional counters to be used at room temperature, methane is often used as a quench gas but ethanol and isobutane are sometimes used. The ionization potential of methane is less than that of helium, argon or krypton which are commonly used in CEMS for the detection of $\gamma$ - and X-rays (Table 3.5). The inert gas ions ionize the methane molecules which are neutralized at the cathode where they are present in an excited state. Since the excitation energy is higher than the dissociation energy, the methane molecules dissociate rather than eject electrons from the cathode. Photons produced in a primary avalanche are efficiently absorbed by the quench gas atoms in the vicinity of the anode and do not reach the walls of the counter. Hence, the dissociation of the quench gas molecule disrupts the counter discharge and the quench component is gradually consumed. The quench process is effective when the ionization potential of the main component of the gas filling $I_m$ is greater than that of the

Table 3.5

| Gas | $\rho$, $\mu g \cdot cm^{-3}$ | $I$, eV | $E_{dis}$, eV | $w$, eV | $F$ | $w/I$ | $r^K_{eff}$, mm | $\sigma_{tot}$, $cm^2/g$ | $\sigma_{ph}$, $cm^2/g$ | $\epsilon_{ph}$, % | $\epsilon_{tot}$, % | $l_{ph}$, cm |
|---|---|---|---|---|---|---|---|---|---|---|---|---|
| He | 178.5 | 24.6 | | 45.6 | 0.21 | 1.79 | 9 | 0.185 | 0.025 | 0.0004 | 0.003 | $1.5 \cdot 10^5$ |
| Ar | 1784 | 15.8 | | 26.2 | 0.19 | 1.70 | 0.9 | 60.5 | 59.6 | 0.94 | 0.96 | 6.5 |
| | | | | | 0.1 | | | | | | | |
| | | | | | 0.17 | | | | | | | |
| Kr | 3740 | 14.0 | | | | | 0.4 | 51 | 49 | | 0.8 | 3.8 |
| Xe | 5890 | 12.1 | | 21.5 | 0.17 | | 0.3 | 167 | 164 | 2.6 | | 0.72 |
| $H_2$ | 89.9 | 15.5 | 4.5 | | 0.34 | 2.27 | 17.5 | 0.36 | 0.003 | $4\ 10^{-5}$ | 0.006 | $2.8 \cdot 10^6$ |
| $N_2$ | 1250 | 15.6,16.7,18.8 | 9.8 | | 0.3 | 2.3 | 1.3 | | | | | |
| CO | 1250 | 14.0,16.5,19.7 | 11.2 | | | | 1.3 | 3.93 | 3.52 | 0.056 | 0.062 | 158 |
| $CO_2$ | 1977 | 13.8,17.3, | 5.5 | | | 2.3 | 0.8 | 4.44 | 4.02 | 0.063 | 0.07 | 87 |
| | | 18.1,19.4 | | | | | | | | | | |
| $CH_4$ | 717 | 13.0,22.4 | 4.5 | | 0.26 | | 2.2 | 1.635 | 1.29 | 0.02 | 0.026 | 750 |
| $C_2H_4$ | 1260 | 10.5,12.5,14.4, | 4.5 | | 0.3 | 2.3 | 1.2 | | | | | |
| | | 15.8,18.8,22.8 | | | | | | | | | | |
| $C_2H_5OH$ | | 10.7,12.2,13.3, | 4.0 | | | | | | | | | |
| | | 13.8,15.9,17.4 | | | | | | | | | | |
| $C_2H_{10}$ | | 10.8,12.5,14.5, | 4.4 | | | | | | | | | |
| | | 18.6,19.9 | | | | | | | | | | |
| Air | 1293 | | | | 0.17 | | | | | | | |
| Ne | | | | 36.2 | 0.13 | | | | | | | |





222

Tables 3.5 (continued)

Notes:

1. $\rho$ is the gas density at 0°C and 1 atm,
I is the ionization potential of the gas,
$E_{dis}$ is the dissociation energy,
w is the average energy required for ion-pair formation,
F is the Fano factor [3.120],
$r_{eff}$ is the effective range of the 7.3 keV electrons,
$\sigma_{tot}$ and $\sigma_{ph}$ are the total cross-section and photo- electric cross section for the 10 keV $\gamma$ -quanta,
$\in$ and $\in_{ph}$ are the corresponding probabilities of the absorption in the $r_{eff}$ layer,
$l_{ph}$ is the thickness of a gas layer at 0°C and 1 atm, necessary to absorb photoelectrically 50 % of $\gamma$ -quanta.
2. For hydrogen and helium the $\sigma_{tot}$ value is given with the coherent scattering cross section subtracted; for krypton at approximately 10 keV there is a minimum due to the K- absorption edge.

quench component $I_q$ and the following relation is fulfilled $I_q - \phi > E_{dis}$, where $E_{dis}$ is the dissociation energy of the quench gas and $\phi$ is the work function for the cathode material.

Aluminium is often used as the wall material in counters and $\phi$ is 4.2 eV. By the use of Table 3.5 one can select a proper composition of the gas filling for a particular experiment. The Table also describes some important parameters for detector design in Mőssbauer spectroscopy, e.g., $r_{eff}$ - the gas thickness to absorb practically all the 7.3 keV electrons. To absorb these electrons, a layer of iron should be $r_{eff} \approx$ 200 nm (≈160 μg $cm^{-2}$) (see Fig.3.12). Assuming, as a first approximation, the $r_{eff}$ value to be Z-independent, and knowing the gas density $\rho$, it is easy to calculate $r_{eff}$ for any gas mixture. The $r_{eff}$ value of 9 mm for helium is in a good agreement with the data found elsewhere [3.107].

If the total interaction cross section for $\gamma$-quanta $\sigma_{tot}$ and the photoelectric effect cross section $\sigma_{ph}$ are known, the detection efficiency $\in_{tot}$ and $\in_{ph}$ can be easily evaluated for $\gamma$-quanta in the counter where the distance between walls is $r_{eff}$. The data in Table 3.5 are given for the 10 keV $\gamma$ -quanta. The addition of a quench gas to helium generally results in the absorption of the greater part of energy in the active counter volume. However, the detection efficiency of the (undesirable) direct radiation is enhanced. For a counter 9 mm thick filled alternately with: He, He + 10 % vol. $CH_4$ and

He + 10 % vol. $CO_2$, the $r_{eff}$ values for the detection of electrons are in the ratio 1 : 0.77 : 0.48, whereas $\sigma_{ph}$ for the 10 keV quanta are in the ratio 1 : 21 : 179, respectively.

In CEMS the observed effect (2.31) may be written as

$$\varepsilon(v) = \frac{I(v) - I(\infty)}{I(\infty) + I_{back}}, \qquad (3.64)$$

where I(v) and I(∞) are the total electron beams at and off resonance. The background - $I_{back}$ is caused by electrons ejected from the walls and produced by interactions of the source radiation with the gas filling.

For bulk samples, the effect can be enhanced only at the expense of $I_{back}$. To do this, the $\gamma$ -quanta must be properly collimated and a counter should be used with a small active volume. For this purpose, a flat counter has been designed having the thickness of the active volume equal to only 2 mm (inner dimensions are 200 $mm^2$ x 2 mm) [3.90,91]. The 7.3 keV electrons having passed through the 2 mm thick helium layer, will lose the 4 keV energy and be easily detected. A substantial contribution to the background in $^{57}$Fe CEMS results from electrons produced photoelectrically by the higher energy $\gamma$-radiation. These electrons lose less than 1 keV of the energy in the counter and can be easily discriminated.

The pulse shape at the output of the proportional counter is also important. The addition of a quench component often leads to an increase in the electron drift rate and hence to a decrease in the rise-time for the output pulse. Thus, for example, if the rise-time for a He filled counter is about 15 μs, the addition of 6 % isobutane reduces the value to 2 μs. This allows shorter output pulses to form and an enhancement of the statistical accuracy by using higher intensities. A pulse shape discrimination can be used at a fixed source strength to improve the statistical accuracy and allow the signals to be distinguished from low-energy ($E \leq 10$ keV) and high-energy electrons. This produces a smaller ionization effect per path length and, consequently, a longer rise-time [3.121,122].

Hence, in summary, it is important that the beam of Mőssbauer quanta should always be properly collimated. If the sample is thin, it is desirable that the beam leaves the active counter volume to diminish back scattering. Electron ejection from the counter walls lowers the effect substantially (see (3.64)). The main contribution into the background from bulk samples is the "wall effect". If the sample is thin, the suppression of the "wall effect" is justified, and the walls are best made of a light material - aluminium, beryllium or mylar.

Soft radiation present in the spectrum of the source e.g. the 6.46 keV X-rays from $^{57}$Co should be filtered (see Sect.2.8). Otherwise, the large photoelectric cross section for low-energy $\gamma$ -quanta causes a large intensity beam of photoelectrons to be produced which lowers the observed effect. Collimation, counter design and pulse-shape discrimination do help in this situation. Aluminium foils or plastic plates are commonly used as filters [3.91,108,123].

Sometimes two, or even four parallel anode wires are used in the counter but our experience has shown that this does not produce a significant gain. The voltage applied to the counter is determined by the counter dimension, particularly the diameter of the anode wire(s), by the composition and pressure of the gas, the required gas multiplication factor M, and some other factors. Voltages from 400 V to 1500 V are commonly used. The counter performance is to a large extent determined by the gas flow rate. Usually it is 1 - 3 $cm^3min^{-1}$, though a higher rate (up to 50 $cm^3min^{-1}$) may improve the counter performance.

Phase analysis of multiphase mixtures, fine particles and disordered substances, as well as surface studies, require Mőssbauer spectra to be recorded over a wide range of temperatures. In nuclear- and X-ray-spectroscopy, where the proportional counter has been used, the problem of the counter operation at temperatures other than the ambient one has not received significant attention. The operation of the proportional counter at liquid nitrogen temperatures was first investigated in Kyoto [3.92-94] and in Cracow [3.102-104].

There are two approaches to the use of proportional counters in CEMS at low temperatures. The first approach is based on the use of pure helium without any quench gas. Since any admixture to helium substantially affects the counter performance, helium should be purified using a liquid nitrogen trap. It is convenient to use helium evaporating from a dewar. Counter designs for operation with pure helium and the appropriate operating modes are described in [3.92,104,115- 117,119]. The absence of the quench component increases the gas multiplication factor. This means that the dependence on the applied voltage is more sharp and narrows the voltage region wherein the counter operates as a proportional counter. Lowering of the temperature requires substantially higher voltages to be applied to the counter. Since the M factor is strongly temperature-dependent, the filling gas temperature should be kept constant within ±2 K. The long-term stability problems for this detector are not easily solved.

The output pulses of proportional counters at 80 K are considerably longer than at room temperature and are characterized by a steeper leading edge with some being of a zigzag shape. This shape is due to the high energy electrons which can be avoided by pulse-shape discrimination [3.92,121, 122]. The voltages at which the counter operates in the proportional mode at 80 K are determined by the counter design and by the presence of admixtures. For example, in [3.92] the counter with the quenching component was operated at room temperature at voltages $U_q$ = 450 V ... 650 V, and

with pure helium at 80 K in the proportional region at $U_p$ = 410 ...440 V, i.e. the voltage range ΔU is 30 V. To solve the stability problems mentioned above, an electronic feed back has been used which controls the anode voltage $U_p$ to keep the M factor constant. It allows long-term measurements at temperatures between 370 K and 50 K to be conducted [3.119].

Sealed counters are also known. The gas pressure in these types of counters is less than 1 atm at room temperature. Typical parameter values are 0.4 atm and 700 V [3.102,104]. On lowering the temperature to that of liquid nitrogen the pressure is lowered to 0.1 atm and the voltage is raised to 1100 V. The lowering of the pressure and the voltage applied to the counter (due to the diminished anode-cathode distance) makes the operation of the proportional counter more stable. The minimal temperature reached for a pure-helium-filled counter is 15 K.

The second approach in the use of proportional counters at low temperatures is based on the use of quench components. Temperature dependences are given in Fig.3.47 of the saturation

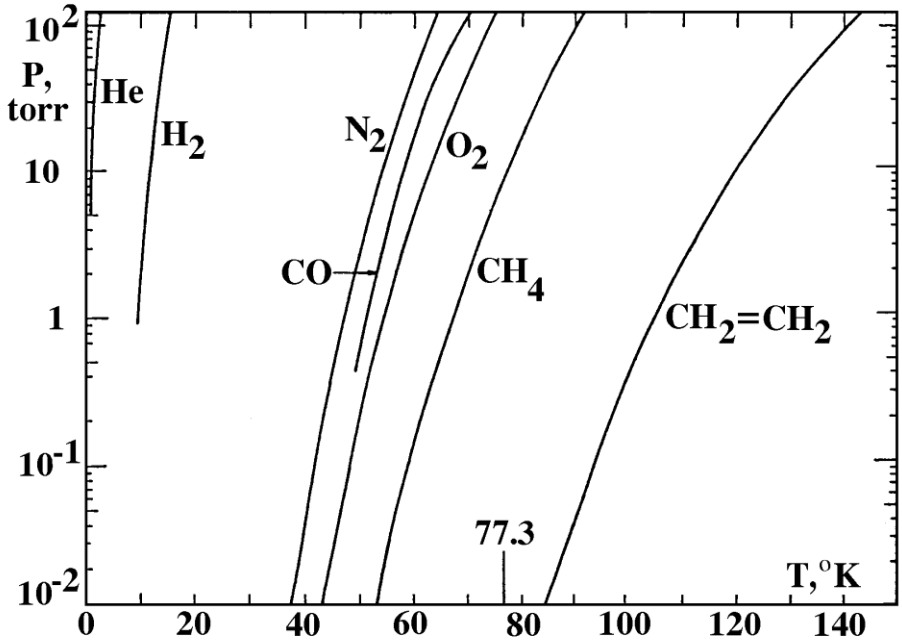


Fig.3.47 Temperature dependences of saturation vapour pressures for gases used in proportional counters (from [3.113]).

pressures of some gases. It is seen that the saturation pressures of $N_2$ and CO are sufficient for these gases to be used as the quench ones. Let a proportional counter [3.95,113] be filled at room temperature with four different gas mixtures to the pressure of 380 Torr. Let one of the following gases (5 vol.%) be used as a quench component: $H_2$, $N_2$, CO and $CH_4$. Hydrogen does not freeze at 77 K, and the nitrogen vapour pressure is too high. Unfortunately, these gases possess a low quenching capability.

Even at room temperature they can be used only over a narrow voltage region (20 - 40 eV). At a multiplication factor value of $\approx 10^5$ the counter goes into the Geiger Müller mode. At 77 K the maximal M value does not exceed $2 \cdot 10^4$, and the output pulse amplitude is not more than 20 mV. Two other gas mixtures are better. Cooling the methane gas mixture down to 77 K leads to the reduction of the methane partial pressure to 4.6 Torr. This is much lower than its vapour pressure at this temperature which is 9.4 Torr (Fig.3.47). At liquid nitrogen temperature the values of the M factor and the output amplitude are: for 5 vol % $CH_4$ - $6 \cdot 10^4$ and 60 mV; for 5 vol % CO - $4 \cdot 10^5$ and 300 mV. Although the gas mixture was not allowed to flow through the counters, the spectral quality was very good. The gas multiplication factor deteriorated with time and discharges occurred in several days so that the gas mixture needed to be changed. Thus, at temperatures down to 77 K methane and carbon monoxide may be used as quench gases.

Pure helium should be used at lower temperatures. Somewhat unexpectedly it was found that on lowering the temperature, the dependence of the factor M on the voltage became weaker. The helium-filled proportional counter was stable at 5 K without any additional electronics. Although the M value was comparatively small ($\approx 170$) the pulse rise-time (2 μs) was constant in the wide range of applied voltages [3.115]. Unfortunately the technique for cryogenic CEMS with a helium- filled proportional counter has not become so popular as one expected.

One of the reasons is some difficulties in operating the helium-filled proportional counter near 4.2 K, which according to [3.116] can be summarized: (i) helium gas is sealed in the counter; (ii) the counter itself is cooled down to low temperatures; (iii) the gas multiplication factor is rather low in the proportional region, at most 200 and (iiii) the applied voltage near 4.2 K becomes much higher than that at higher temperatures (77 - 300 K). A new design for the counters was suggested and high-quality cryogenic CEM spectra at temperatures down to 1.75 K were recorded [3.117].

β-Spectra is the best characteristic of the detector performance. Typical electron spectra measured at various temperatures are shown in Fig.3.48. The best energy resolution and lower noise level are for the counter with a filling gas of He + 1 % $CH_4$ at room temperature (see Fig.3.48 a). With pure helium the spectra are progressively smeared out at 4.2, 2.2 and 1.75 K (see Fig.3.48 b, c, and d) respectively. The anode voltage can be increased to obtain higher output pulses as long as a continuous electric discharge is not induced; a discharge usually makes it impossible to pick out signals caused by radiations. When the gas temperature is decreased the anode voltage must be lowered to avoid the continuous discharge. This is why the noise level increases when the temperature is decreased.

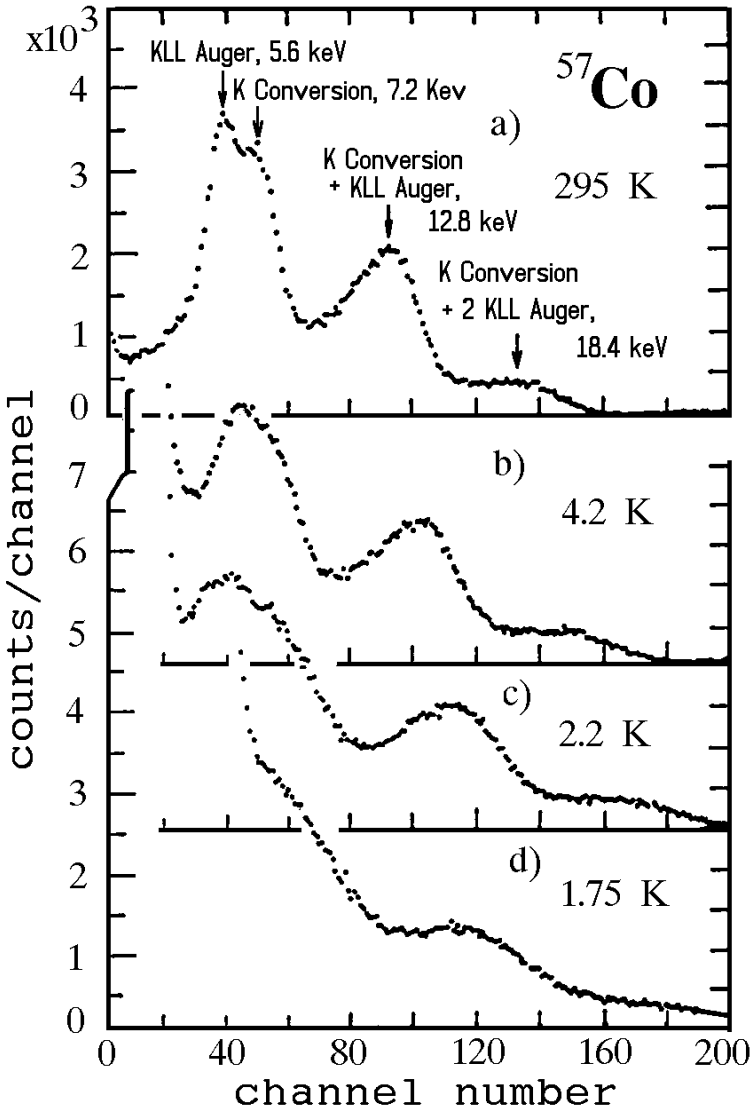


Fig.3.48 Pulse-height spectrum of a 8 nCi $^{57}$Co source inside the counter. The spectrum (a) was obtained with a filling gas mixture of He + 10 % $CH_4$ at room temperature. The spectra (b), (c) and (d) were obtained with pure helium gas at 4.2, 2.2 and 1.75 K, respectively.(from [3.117]).

It is noted that the shape of the gas multiplication curve does not appreciably depend on the gas temperature in this temperature region. The lowest temperature achieved in CEMS was 1.75 K [3.116]. Helium gas in the counter ( 1 atm at room temperature) is partially liquefied below 1.5 K. It is expected that the operation of the proportional counter greatly suffers from the partial liquefaction, as shown by the studies on the gas mixtures of Ar/$CH_4$ and He/$CH_4$ at liquid nitrogen temperature, 77 K [3.95,113]. Further investigations at temperatures below 1.75 K are desirable to search for the low-temperature limit of the method. A stable operation of a cryogenic

proportional counter for CEMS at low temperatures near 4.2 K for more than two weeks has been reported [3.117].

Specific problems connected with the change of surface properties occur when recording Mőssbauer spectra from surface layers at high temperatures. Typical processes involve the thermal decomposition of the surface layer or its reactions with the gas-filling components. This can be considered by examining the designs and operating modes of proportional counters used for high temperature studies. If temperatures not exceeding 600 K are required the sample may be placed on a graphite or beryllium holder and a thermal contact made between them. At 600 K a temperature stability of better than ± 5 K can be easily obtained [3.112]. A gas flow of helium-methane can be used in this counter. On raising the temperature, the voltage applied to the counter needs to be lowered. If the gas mixture density (i.e., the ion mean free path) is kept constant on raising the temperature, the counter operation will be independent of the gas mixture temperature. On further increase of temperature, the electron thermoemission from inside of the counter increases. In addition, electrons will be produced by gas molecules hitting the surfaces. All these electrons will move to the anode creating a charge cloud around it which disrupts the counter operation. The noise level increases sharply, and from a certain temperature no rise in the voltage applied to the anode wire can help in separating signals from the noise. An example is copper where the work function is 4.3 eV. At 540°C the emission rate is 1 electron $cm^{-2}s^{-1}$, and at 770°C it is $10^6$ electrons $cm^{-2}s^{-1}$.

Another serious complication is the substantial deterioration of the insulating properties of the materials on heating. For example, such effects can influence anode holders used to center it relative to the cathode. Thus, the specific electric resistance of fused silica which is $10^{18}$Ohm cm at 300 K, falls to $10^7$ Ohm cm at 1000 K. The drop in resistance on heating leads to the appearance of false output pulses. Hence, on designing counters for high temperature operation, attention should be paid to preventing the insulators from heating. In one such counter, only the active counter volume wherein there are no insulating materials between the anode and cathode was heated. The anode is held and centered by two metallized quartz tubes which are placed outside the active counter volume. The counter can operate at temperatures up to 1100 K [3.94].

A counter can be constructed for the heating of only the sample by placing it on a special holder. In such a counter there is always a temperature gradient between the sample holder and the counter body, hence to record Mőssbauer spectra a reliable temperature control system is required. This design allows a temperature stability of ± 1 K at sample temperatures up to 740 K [3.105] to be achieved. When the entire active counter volume is heated, the entrance window is usually made of boron nitride which has sufficient electric conductivity at 600 K. Furthermore, a layer 1.5 mm thick absorbs 99 % of the 6.46 keV quanta and only 33 % of the 14.4 keV quanta.

Of special importance at high temperatures is the selection of the filling-gas mixture. Although advantageous it is possible to work with pure helium only at low voltages when the output signals are small. At temperatures when the gas mixture begins to react with the surface the signal of a helium-filled counter is lost in the noise unless special electronic circuits are used.

A gas mixture of He + 10 % $CH_4$ is satisfactory up to temperatures of about 700 K. At higher temperatures methane decomposition occurs and, at 811 K, methane can burn. Hence at temperatures above 700 K a gas mixture of He + 10 % $CO_2$ is used which requires a higher voltage. A long exposure of the samples to this mixture at about 900 K also results in irreversible changes of the samples. Pure $H_2$ and $N_2$ may be used as filling gases but this requires higher voltages to be applied, and the output signal is smaller than for the He + 10 % $CO_2$ mixture. These counters are difficult to operate, and they have not found applications in CEMS.

The proportional counters used in CEMS detect electrons over a wide energy interval and a small drift of the multiplication factor during the operation may be tolerated. This allows a wide variety of gas mixtures to be used and, having chosen a proper operation mode for a particular measurement, a small change of the gas mixture composition can be tolerated. For example, oxygen is known to be a poison for gas-filled counters due to its high electron affinity. However, in the case above, the presence of up to 1 % oxygen in the gas mixture still allows CEM spectra to be recorded.

### 3.8. Depth Selection by Means of Proportional Counters

Let us analyze the pulse-height spectrum obtained with proportional counters (see e.g. Fig.2.37) and the effect which can be observed in CEMS. It is also necessary to consider the energy resolution of proportional counters and the prospects of performing a depth-selective analysis with them. Typical pulse height spectra obtained with a flat proportional counter are shown in Fig.3.49. Both the source and absorber are of an austenite stainless steel (a = 50 %). The spectrum obtained in the absence of resonant scattering is so simple (curve a) that the requirement to have an energy resolution of the detector may appear to be superfluous. Nonetheless, if the source and absorber are on resonance (curve b of Fig.3.49) the spectrum shape is slightly deformed, though it is hardly possible to observe any single lines. The intensity increase at energies lower than 2 keV is caused mainly by the Compton effect from the high energy radiation of the source.

In Fig.3.50 (curve a) a pulse height spectrum is presented which was obtained with a counter of another design [3.107] and a better energy resolution. An $\alpha$ -$^{57}$Fe scatterer was used (a = 90 %), and the source velocity was $v_1$. The spectral shape was

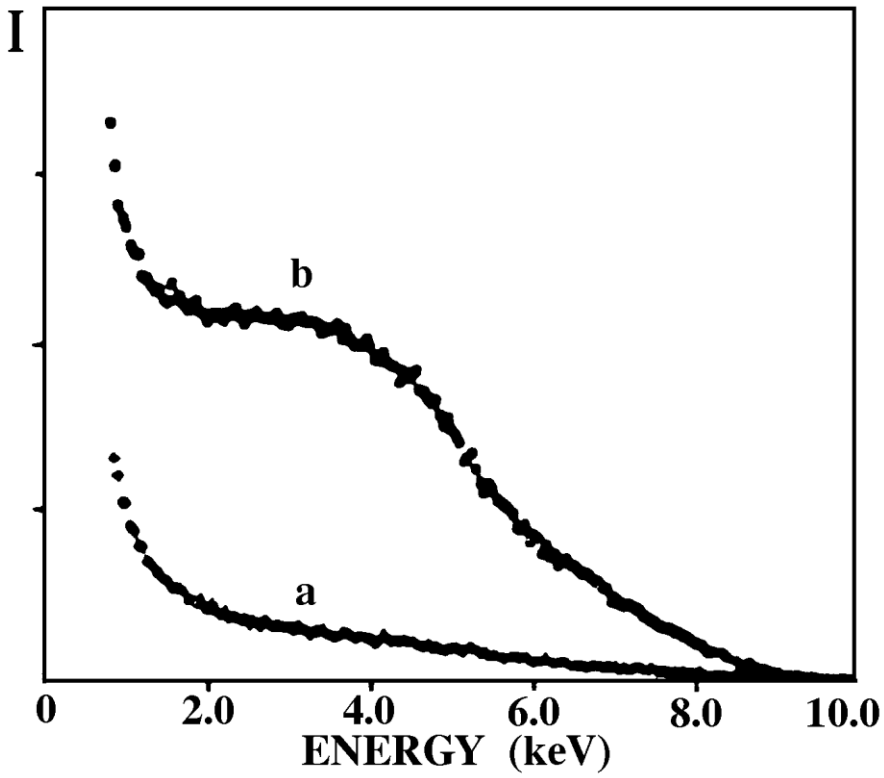


Fig.3.49 Pulse-height spectra for scattering of conversion electrons detected with the counter of Fig.3.46. a - off resonance, b - on resonance.

greatly affected by the fact that the radiation of a $^{57}Co$ source was made monochromatic so as only the 14.4 keV quanta were incident onto the sample. Under this situation there are fewer low-energy electrons and the spectrum may be considered as a superposition of two lines. One of them is due to the K- shell photoelectric effect (K-conversion electrons) and also KLM- and KLL-Auger electrons. The other line is due to L- conversion electrons and is a result of the simultaneous detection of photo- and Auger electrons. The operation of this proportional counter is illustrated by curve b which gives a pulse height spectrum due to Cu $K_\alpha$ X-rays. The spectral shape (Figs.3.49 and 3.50) is determined by the stochastic nature of the energy loss process for electrons on travelling from the depth of origin to the scatterer's surface. This effect could be eliminated if a thin Mőssbauer source (see Fig.3.11) is used as a source of electrons.

A spectrum of a $^{57}Co$ source obtained with a proportional counter is given in Fig.3.48a. The instrumental line broadening (the energy resolution is about 20 %) causes the spectrum to be more like the one shown in Fig.3.50 rather than the spectrum of Fig.3.11. Some peculiarities appear in the spectrum due to the source being placed inside the proportional counter. Auger electrons following the $^{57}Co \rightarrow {}^{57}Fe$ decay may cause output pulses to appear from the proportional counter corresponding to energies of 12 keV and ~18 keV. This occurs if they have been simultaneously detected either with K-conversion electrons or subsequent Auger electrons, or both.

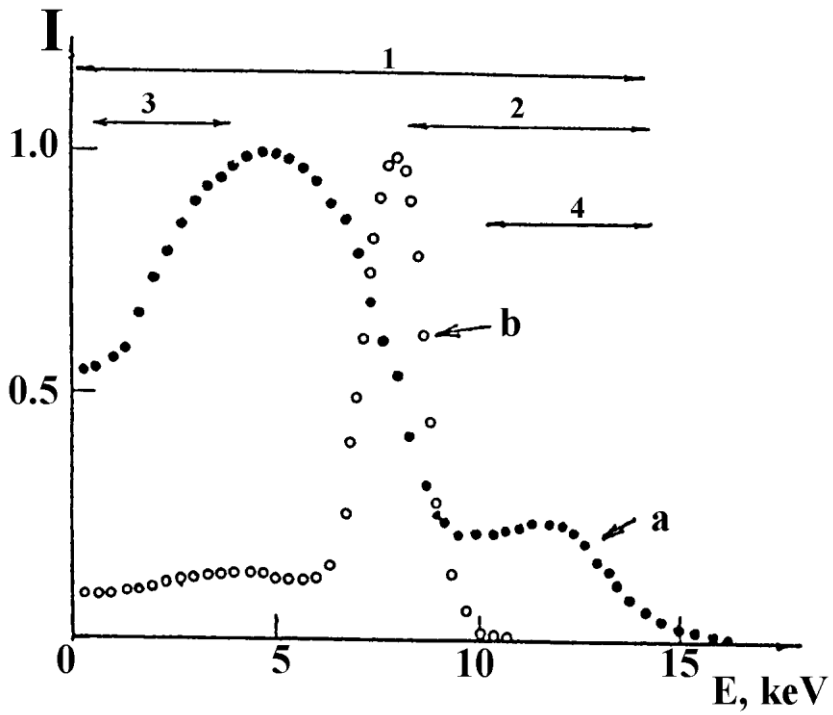


Fig.3.50 Pulse-height spectrum from an $\alpha$ -Fe plate (a = 90 %) (a), and the 8.05 keV Cu $K_\alpha$ X-rays (b). 1 - 4 are the energy intervals used to obtain the weight functions (from [3.107]).

Before conducting a series of measurements the experimentalist needs to select the operating mode of the proportional counter and the pulse discrimination levels at the output so as to optimize the main parameters of the Mőssbauer spectrometer to reach both the maximum effect and count rate. For this purpose, standard scatterers are used which are enriched up to 90 % (see Sect.3.5). Stainless steel scatterers are easier to work with and the observed effect is insignificantly larger than with $\alpha$-Fe. There are several reasons to explain this: the Mőssbauer line is broader, $n_{eff}^{SS}$ is less; there is usually a thicker oxide layer mainly $Cr_2O_3$ on the surface of stainless steel than on the surface of pure $\alpha$ -Fe. Austenite stainless steel is a convenient material for evaluation purposes, and $\alpha$ -Fe should be used for precision calibrations.

The proportional counters used in CEMS may be divided into two groups. Let counters with the active counter volume less than 3 mm thick belong to the first group, and the second group of counters be those with the active volume thicker than 3 mm (usually from 6 mm to 12 mm). There is no energy resolution for the first group of counters since, for example, the 7.3 keV electrons emerging at angles close to the surface normal would lose an energy of about 2 - 3 keV in the active counter volume.

The discrimination level for the first group of counters depends on the need to have a greater effect and/or a high count rate and is determined by the noise level and detector design. It has been reported [3.104] that with a counter of active volume about 1 mm thick, at a threshold setting of > 3 keV, an effect $\varepsilon(0) \approx 1000$ % can be obtained

on stainless steel although at the expense of the count rate. With a $^{57}$FeAl layer 0,2 μm thick (on mica) ε(0) ≈ 1500 % can be achieved practically without any discrimination. On α -$^{57}$Fe foils $\varepsilon_2$ is approximately 300 ÷ 450 % at a threshold setting of ≈ 1 keV. In a series of papers, e.g. in [3.104] it has been reported that at a higher threshold setting the ε(0) value increases significantly. In the authors opinion [3.106] the contribution to the Mőssbauer spectrum from the surface layer increases, but the increase of the effect and of the surface sensitivity lead to a count rate loss of down to two orders of magnitude. Sometimes the increase may be caused by artefacts.

The increase of ε(0) at a higher energy threshold setting is partially due to the fact that the ionization which is produced by both high-energy electrons and by L- and M- conversion electrons is small due to the counter being thin. This does not result in the appearance of signals corresponding to the 10 keV energy interval. Both the background and L- and M-conversion electron contributions are small in this region. At the same time there is an appreciable probability that the K-conversion electrons and the subsequent KLL-Auger electrons being isotropically emitted will reach the active counter volume practically simultaneously and will be detected as one event. If they are emitted from upper layers at an angle to the surface and have lost a small part of their energy in the sample, the total signal even in a thin counter may have an amplitude equivalent to the ionization effect from the 10 to 13 keV electrons. This results in a sharp surface selectivity. Similar pairs of electrons are also produced due to the photoelectric absorption of the 14.4 keV electrons in iron contributing to the background. However, the photoelectrons have a higher probability of ejection perpendicular to the incident quantum direction and the probability for the two electrons to be detected simultaneously is low.

Thus, the detection of output signals corresponding to energies of 10 to 13 keV, is equivalent to the detection of K- conversion and Auger electrons emerging at glancing angles to the surface if the active volume is 1 mm to 2 mm thick. Theoretical evaluations of the weight functions have shown that by detecting electrons emerging at small angles to the surface, the surface selectivity is enhanced. Computations of the weight functions for integral CEMS made by Liljequist, show that even with no energy discrimination, the detection of electrons emerging at glancing angles leads to an effective reduction of the thickness of the analyzed layer (Fig.3.51). This is difficult to use in the development of a quantitative depth- selection technique, since the intensity loss of two or more orders of magnitude devoids the technique of the main advantage over DCEMS. The theoretical concepts of the technique are too complex to be developed due to a strong dependence on detailed experimental features such asstructure, topography and composition of the sample under investigation, the gas-flow rate, the composition of the gas mixture and temperature. Thicker counters are required for studies of real surfaces of bulk samples.

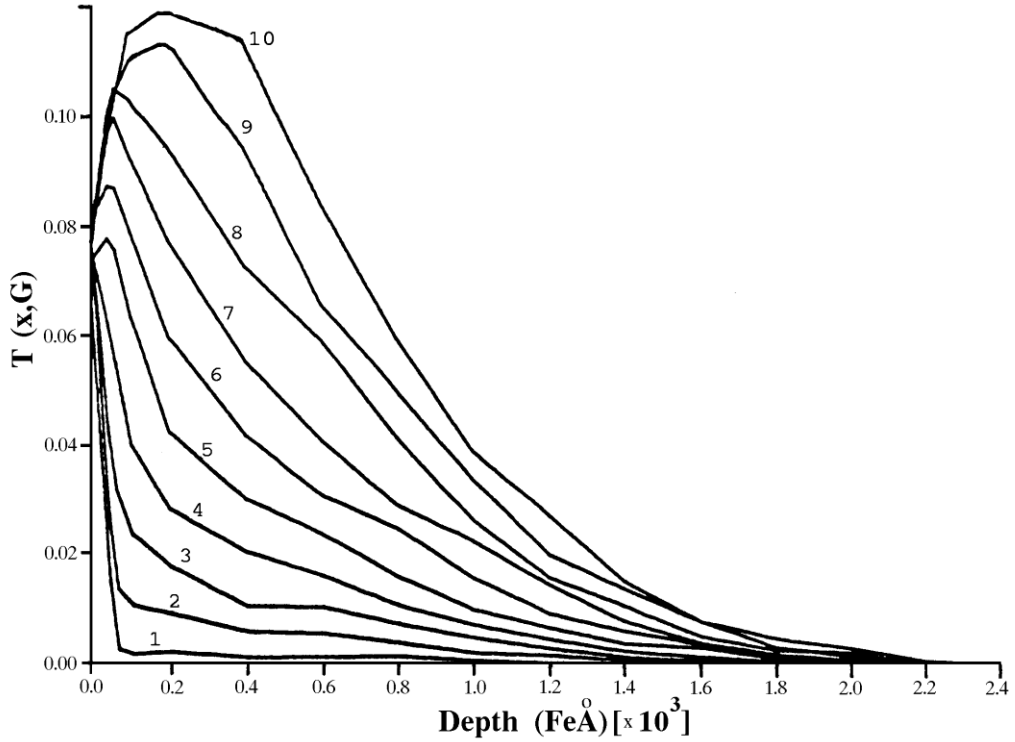


Fig.3.51 $^{57}$Fe K-conversion electron weight functions for detection in the following angular intervals: $0 < \cos\theta < 0.1$ (1); $0.1 < \cos\theta < 0.2$ (2); ... $0.9 < \cos\theta < 1.0$ (10) (from [3.79]).

Let us now examine the operation of a CEMS spectrometer with a thick active counter volume when used to detect electrons. The Mőssbauer spectra of a stainless steel plate covered with an iron layer (a = 2.14 %) 35 nm thick are given in Fig.3.52. The active counter volume was 6 mm thick. A corresponding pulse height spectrum is given to the right of each Mőssbauer spectrum. The regions used are hatched in the figures and the thresholds are indicated. The ratios of the area under the spectrum from stainless steel to the area of the total Mőssbauer spectrum are appreciably different. Formally, this is equivalent to depth selection, therefore the recording of spectra in the integral CEMS mode to obtain reproducible results requires that the discriminator should also operate in an integral mode, i.e., only the low-energy threshold should be set at about 1 keV. In order to achieve depth selection in CEMS, several spectra should be recorded which correspond to different regions of the electron spectrum. A special technique should be developed to obtain the relevant weight functions.

The operating principle of proportional counters allows depth selection to be made in CEMS. However, until the 1980's DCEMS techniques were mainly based on β-spectrometers. Usually K-conversion electrons are considered. The energy resolution of proportional counters in this energy region (i.e. $\approx$ 7 keV) is not better than 15 %, i.e. in the absolute units it is greater than the APK interval. This means that the detector will respond to various groups of electrons and, using the technique developed for DCEMS, the computation of the weight functions is complicated.

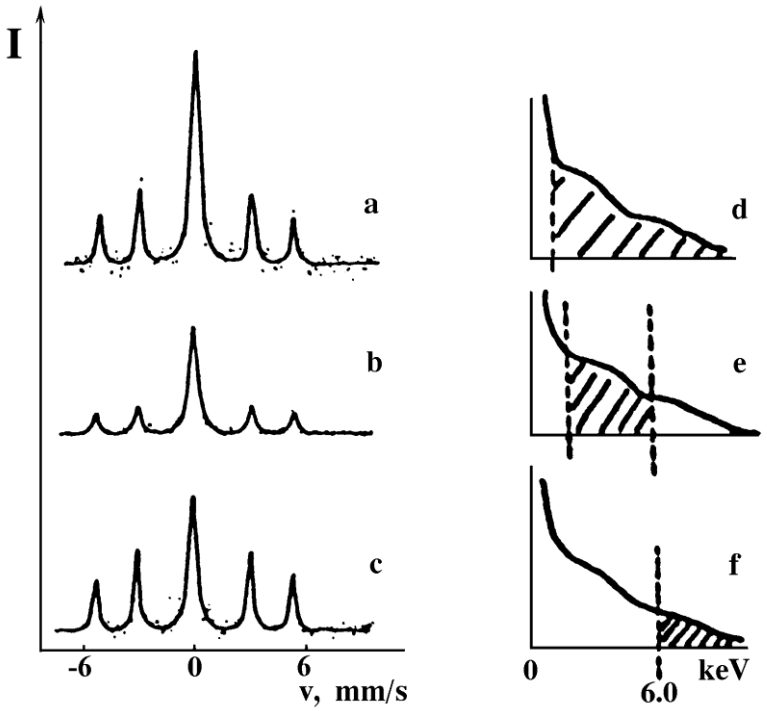


Fig.3.52 Mőssbauer spectra (a, b, c) and pulse-height electron spectra (d, e, f) from a stainless steel plate covered with a 35 nm thick iron layer. The shaded areas in d, e, f spectra indicate the energy intervals used to obtain the corresponding Mőssbauer spectra.

If the discriminator is set to detect the 6.3 keV electrons, and irrespective of how narrow the discriminator window may be, at an energy resolution of 15 % the KLM-Auger electrons, K-conversion electrons that have lost an energy in the 0 - 2 keV interval in the scatterer before reaching the surface, and KLL-Auger electrons, ejected directly from the surface will all be detected. Thus, the theoretical description of the physical picture is complicated. Therefore, as an alternative, an empirical approach may be used if the energy resolution of the detector is satisfactory.

We shall try now to evaluate the energy resolution of proportional counters. This is determined by numerous factors. Two of them are fundamental and cannot be excluded. These are the statistical fluctuations in the number of ion pairs produced by a primary ionizing particle, and statistical fluctuations in the number of secondary electrons produced in avalanches triggered by the primary electron. The energy resolution is also dependent on the counter design, the uniformity of anode wires, electron affinity of admixtures to the filling gas and the amplifier noise level. The resolution may depend on the operating mode of the counter, i.e. on the gas multiplication factor value, the gas-flow rate and the state of the anode wire surface.

Assume that there is no interaction between ions (electrons) produced by primary electrons (either reaching the active counter volume or produced therein) and those formed in avalanches. The accuracy of energy determination is given by the probability theory as

$$\left(\frac{\sigma_p}{\bar{p}}\right)^2 = \left(\frac{\sigma_N}{\bar{N}}\right)^2 + \frac{1}{\bar{N}}\left(\frac{\sigma_M}{\bar{M}}\right)^2 , \qquad (3.65$$

where N 7 is the average number of ion pairs produced by a particle or quantum absorbed in the active counter volume with energy E. M8 is the mean gas multiplication factor, 9 p=NM 10 ; $\sigma_N$, $\sigma_M$ and $\sigma_p$ are the standard deviations of the quantitaties above.

It has been shown by FANO [3.120] that if the energy E is measured by the ionization produced when there is no gas multiplication (M = 1), statistical fluctuations in the ion pairs set an upper limit to the accuracy of the measurement

$$(\sigma_N)^2 = (N - \bar{N})^2 = F\,\bar{N} ; \qquad \left(\frac{\sigma_N}{\bar{N}}\right)^2 = \frac{F}{\bar{N}} , \qquad (3.66$$

where F < 1. For hydrogen, by Fano's evaluations, O.33 < F < O.5. F is called the Fano factor. Fluctuations in the total ionization produced in the active counter volume, statistics of avalanches, the ultimate energy resolution of proportional counters and some other problems have been considered in [3.124-126]. The authors obtained theoretical and experimental values of the F and w parameters (w = E/11) for some gases and their mixtures used in proportional counters. It has been shown that these parameters can be considerably reduced by a proper selection of the gas mixture.

Let F' be the variance of the gas multiplication factor for an avalanche produced by a primary electron; $F' = (\sigma_M/12)^2$. The equation for accuracy of the energy measurement (3.65), taking (3.66) into account, may now be written as

$$\left(\frac{\sigma_p}{\bar{p}}\right)^2 = \frac{(F + F')w}{E} . \qquad (3.67)$$

The ultimate energy resolution of the proportional counter is usually determined by the factor F'. As a lower limit of the factor, 0.61 is often taken. ALKHAZOV et al. [3.125,126] have studied the dependence of F' on various factors and shown that sometimes the F' values may be less than 0.61.

If $F'$ is taken to be 0.61, the ultimate accuracy of energy determination of a particle in an Ar + 10 % $CH_4$ gas-filled counter given by (3.67), may be reduced to

$$\frac{\sigma_p}{\bar{p}} = \frac{C}{\sqrt{E}} = 0.146\ E^{-1/2}\ , \qquad (3.68)$$

where E is in keV. The dependence of the accuracy of measurements on the energy of detected quanta is given in Fig.3.53 [3.127]. The wire anode diameter was 50 μm, and voltages applied were in the 1.5 - 2.1 kV interval.

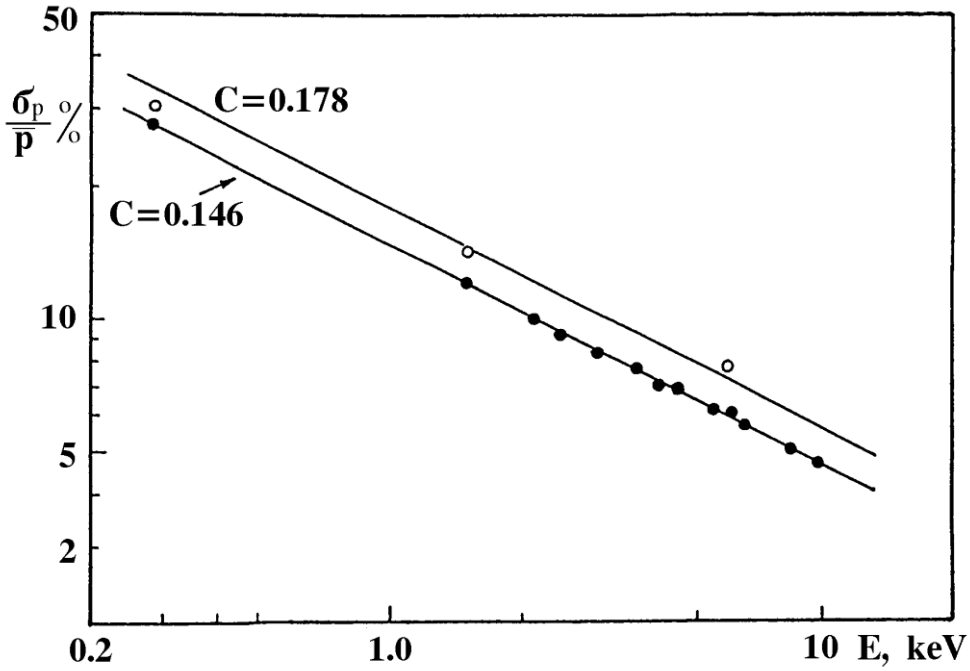


Fig.3.53 Accuracy of energy measurements with a proportional counter. Solid lines are obtained by (3.68) [3.127].

The collimation angle for the quanta incident on the counter window was 3°. In a properly conducted experiment the gas multiplication factor can be made independent of the detected radiation energy in a wide energy range. It has been shown that in order to reach the ultimate accuracy of energy determination there is no need to have a minimal value of the gas multiplication factor. The dependences shown in Fig.3.53 were obtained for $M \approx 10^4$. The anode wire quality greatly affects the energy resolution of the counter. Thus, an ordinary tungsten wire 50 μm diameter may have the diameter fluctuations of up to 1 % within a distance of 1 - 2 mm. Experimental values of the energy measurement accuracy obtained with this anode are given in Fig.3.53 by open circles. The data obtained with the wire whose diameter is constant within 0.25 % are shown by closed circles. It is only by using this wire that it has become experimentally possible to obtain the theoretical value of the factor C in (3.68).

Both in nuclear and X-ray spectroscopy, the experimentalist deals not with the accuracy of energy determinations $\sigma_p$/ 13, but rather with the energy resolution of the spectrometer. On recording an energy spectrum, errors of the energy measurement usually obey the normal distribution law. For this distribution, the full width at half maximum (which determines the relative resolution R of the counter) is 2.35 times the standard deviation of the mean, hence the energy resolution is

$$R = \frac{\Delta E}{E} = 2.35 \sqrt{\frac{(F' + F)\, w}{E}} \quad . \qquad (3.69$$

For the energy interval of interest (1 - 20 keV), the resolution of counters has been experimentally investigated for well-collimated X-rays in cases where the active counter volume thickness (d) is much greater than the total range of photoelectrons (l) [3.125-128]. The counter volume and the gas mixture must be such that if the photoelectric effect has taken place the electron escape may be neglected.

In CEMS there is no collimation at all. If, in addition, $d < l$, fluctuations in an energy loss fraction of the primary electron on traversing the counter volume also determine the energy resolution. This fraction may vary from 0.3 - 0.4 $E_0$ for electrons emitted perpendicularly to the sample surface, to $E_0$ for electrons emitted at a certain angle $\theta > \theta_{crit}(E_0,d)$ in this counter. This results in an extra broadening and distortion of the line.

The best resolution is obtained with helium-acethylene and neon-argon gas mixtures, since the parameters w, F and F' are less than for an argon-methane mixture. For a neon-argon mixture a record energy resolution has been reported for the 5.9 keV X-rays (R = 11 % at M ≈ 100) [3.129]. Theoretically it is possible to obtain an F' parameter of _ 0.4 for helium- methane gas mixtures. For this traditional gas mixture an energy resolution R could be obtained of ~10 % on the 7.3 keV line and a depth selection measurement could be made using the DCEMS weight function approach (see Sect.3.4).

In addition to conventional proportional counters, multiwire proportional chambers are also widely used at present. This allows work to be performed at count rates exceeding $10^5$ counts $sec^{-1}$ and the simultaneous determination of the particle or quantum coordinates (see e.g. [3.130]). Apart from this, gas scintillation proportional counters have also appeared. In these counters which are filled with an inert gas or a mixture of the gases, the energy dissipation by the primary particle or quantum takes place in a low electric field region of the counter. The charged particles are then accelerated in high electric field regions. Electrons which have not acquired sufficient energy for ionization of atoms, will emit ultraviolet photons.

To detect this radiation, whose spectrum is determined by the filling gas, photomultiplier tubes are used. By this, an energy resolution of 8 % on the 5.9 keV line has been achieved [3.131]. The use of this technique is likely to be promising in CEMS. The same fairly good resolution is obtained by a technique using a detecting system based on the proportional counter controlled by the signal from characteristic X-rays produced in the gas mixture and escaping the active counter volume [3.132].

The weight functions $T_{U,\Delta U}(x)$ must be obtained for depth selection. These are analogous to the $T_V(x)$ functions used in DCEMS based on β-spectrometers. There are several means of obtaining these functions using proportional counters. One is based on studies of the passage of electrons through thin layers and has been discussed in Sect.3.4 (see Figs.3.31 and 3.32). In the case of interest, Mőssbauer sources or resonant scattering and the photoelectric effect in the sample are used as a source of electrons. With the effective thickness of the radionuclide of about one monolayer (only 9 nCi $^{57}$Co) and using the proportional counter, an electron spectrum of the source can be obtained. Studies of the electron spectral transformations have enabled the weight functions for a flat proportional counter (R ≈ 23 %) to be obtained [3.133].

By use of a differential discriminator, various regions of the pulse-height spectra have been selected. The intensity of radiation corresponding to a discriminator window is determined by electrons, originally with different energies, being detected together. Pulses produced by the same electrons can be selected by another discriminator window. However, it is more probable that pulses will be selected by this window which correspond to other energy losses and/or for other groups of electrons. The particular group of electrons is dependent on the layer thickness, the position U and the width ΔU of the discriminator window, the distance from the surface of the layer dx from which the electrons have been originated, and the energy resolution of the detector. The better the energy resolution, the smaller the number of electron groups which contribute to the intensity detected, and the less the uncertainty of the depth of origin of a given detected electron.

In the paper mentioned above, resonant scattering in a sample of α-$^{57}$Fe 265 A| thick was considered. $^{56}$Fe layers of 273, 563, 836 1144 and 1512 A| thickness were deposited. The weight functions obtained by the treatment of the experimental electron spectra for three energy intervals were appreciably different (see Fig.3.54a). A disadvantage of this approach, apart from the experimental problems, is the fact that it is not the weight functions that have been determined, but rather the transmission functions similar to those experimentally obtained in studies of electron penetration in thin films.

Methods of obtaining the weight functions by means of photo

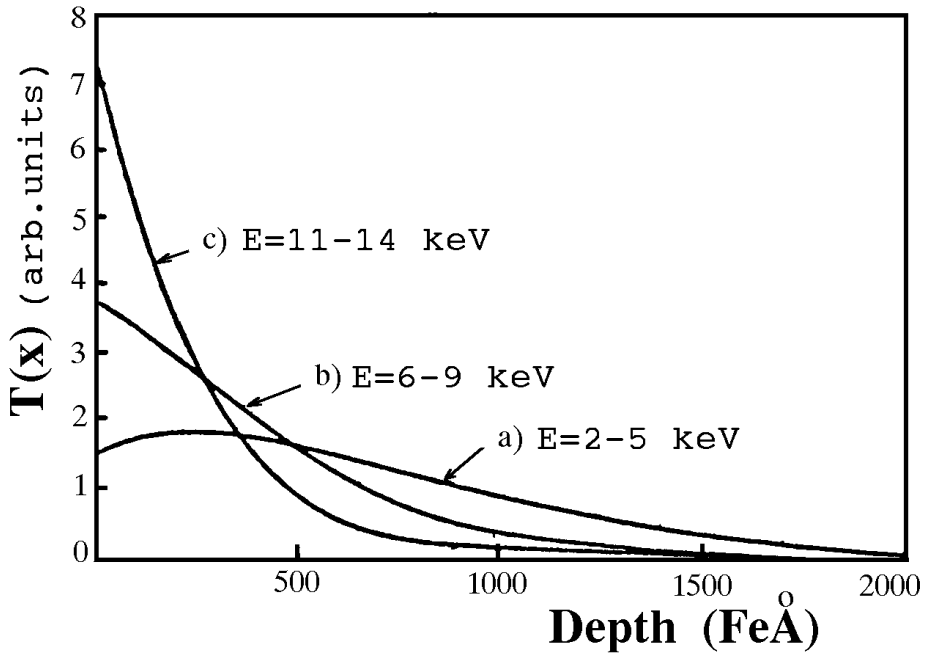


Fig.3.54a Experimentally obtained weight functions for three energy intervals in [3.133] (compare Fig.3.48a). a) - the first energy interval; b) - the second interval; c) - the third energy interval.

emission measurements under conditions of X-ray diffraction are known though not used in practice. A more practical method involves angular dependence studies of photoemission as the angle of incidence decreases to the critical angle [3.134,135]. Interference between the incident and reflected waves then leads to the total reflection (see Sect.2.5).

Let us, instead of photons, detect photoelectrons escaping the surface. As the angle of incidence approaches $\gamma_{cr}$, the electron spectra should be appreciably affected, especially in the vicinity of $\gamma_{cr}$. Indeed, on approaching $\gamma_{cr}$, the photoelectric effect will first cease at a greater depth. Photoemission of electrons reaching the surface from greater depth will be diminished, decreasing thereby the contribution to the total intensity of those groups of electrons that had a higher energy at the time of their emergence.

Angular dependences of the reflected radiation $R(\gamma)$ and those of electrons $\kappa(\gamma)$ may be written [3.135] in this form:

$$R(\gamma) = \left| \frac{\sin\gamma - (\chi + \sin^2\gamma)^{1/2}}{\sin\gamma + (\chi + \sin^2\gamma)^{1/2}} \right|^2 , \qquad (3.70)$$

$$\kappa(\gamma) = \frac{I(\gamma)}{I(90°)} \sim \frac{1}{\sin\gamma} \int_0^\infty Q(\gamma,x)\, T(x)\, dx , \qquad (3.71)$$

where

$$Q(\gamma,x) = \frac{4 \sin^2\gamma \exp(-q(\gamma)x)}{| \sin\gamma + (\chi + \sin^2\gamma)^{1/2} |^2} , \qquad (3.72)$$

$$q(\gamma) = \frac{4\pi}{\lambda} Jm (\chi + \sin^2\gamma)^{1/2} . \qquad (3.73)$$

$I(\gamma)$ is the intensity of electrons detected at a given differential discriminator setting (the number of counts in each channel of the accumulating device when the channel number is related to the angle of incidence $\gamma$); where $Q(\gamma,x)$ is the wave-field intensity in the sample at a depth x; $\chi = \chi_r + i\chi_i$ is the polarizability of the medium; $q(\gamma)$ is the extinction coefficient; $\lambda$ is the wave length of the incident radiation. The pre-integral factor in (3.71) accounts for the increase in the area of the irradiated region as the angle of incidence decreases.

An experimental arrangement used to obtain the weight functions is given in Fig.3.55 [3.135]. The 14.4 keV quanta

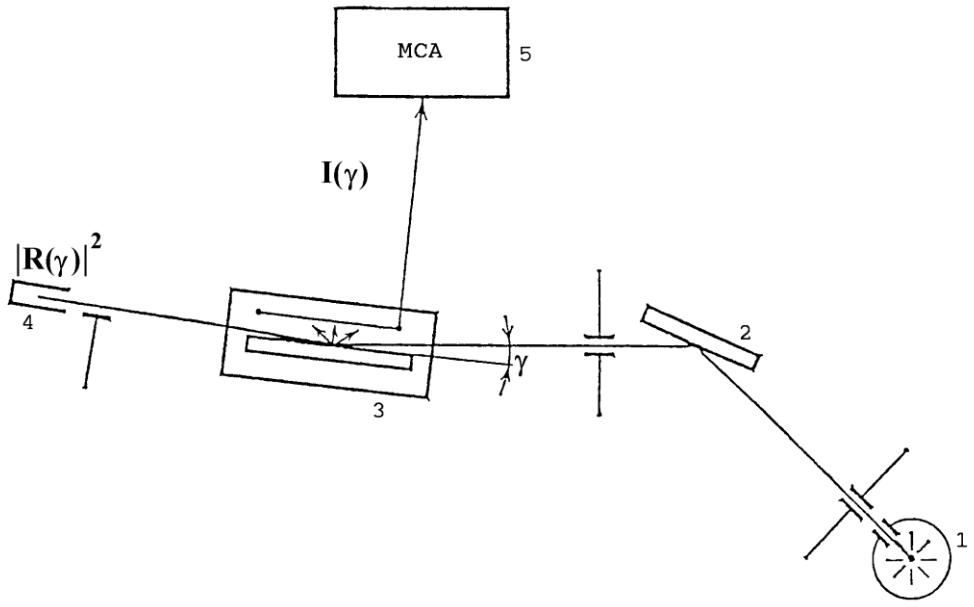


Fig.3.55 Experimental set-up used to obtain the weight functions (from [3.135]). 1 - X-ray tube; 2 - monochromator (Si (111)); 3 - □-Fe sample inside the proportional counter for detecting electrons; 4 - X-ray detector; 5 - data accumulation device.

were separated from the contributions spectra of the X-ray tube by means of a collimator-monochromator (the symmetric reflection (111) of a silicon crystal). The sample was an $\alpha$-$^{57}$Fe plate (the surface roughness being 300 - 500 A|). Four energy intervals in the electron spectrum can be identified and are presented in Fig.3.50. The first interval corresponds to the integral mode of CEMS, i.e. where all the electrons escaping the sample surface are detected.

The second interval is chosen to correspond to the photo- and Auger electrons which emerge from the surface having lost a small amount of energy in the sample. Electrons photoelectrically produced from the L-shell and which have travelled a relatively large distance are also included in this group although their contribution is small. Electrons in the third energy interval will have travelled, on the average, a large distance and lost a considerable part of their initial energy. More accurate calculations of the weight functions require that the fourth energy interval should be considered. This corresponds to those primary electrons that have lost smaller amounts of energy in the sample than electrons of the second interval.

An appreciable difference in the shape of the $\kappa(\gamma)$ curves presented in Fig.3.56, indicates that these dependences give

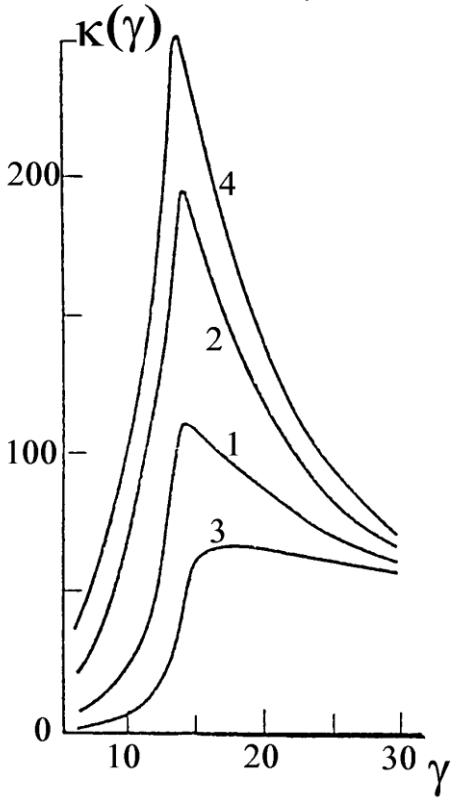


Fig.3.56 Angular dependences of electron photoemission in the energy intervals of Fig.3.49 (from [3.135]).

information on the weight functions. The absolute intensity of the detected electrons is determined by the part of the sample surface from which the electrons are detected, by the depth of the field penetration into the sample ($L$), and by the escape depth of electrons of a given energy interval ($d_i$). Let us consider curve 2 in Fig.3.56 which corresponds to electrons emerging from a relatively thin layer (the second energy interval of Fig.3.50) at angles of incidence greater than the critical angle. $L >> d_2$ and the intensity of photoemission of such electrons is mainly determined by the irradiated area which is inversely proportional to $\sin\gamma$.

At angles smaller than the critical angle, the area to be penetrated by the wave field ($L < d_2$) is narrowed in the jump-wise manner and the electron intensity diminishes. For electrons that have lost a considerable part of their energy in the sample (the third energy interval, see Fig.3.50), even before the critical angle is reached, $d_3$ becomes commensurable with $L$, and then less than $d_3$. At $\gamma > \gamma_{cr}$ the value of $L$ is proportional to $\sin\gamma$ (see Fig.3.57), and hence the product of the irradiated area and the field penetration depth into the sample is almost angular-independent.

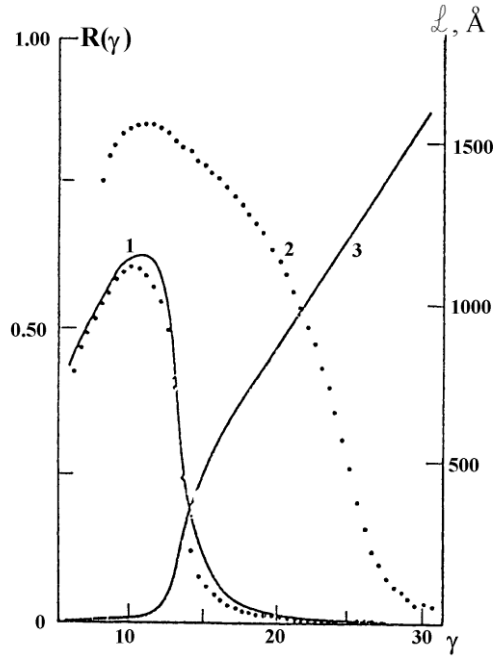


Fig.3.57 Angular dependences of the X-ray intensity (1, 2) and field penetration depth (3). Curves 1 and 3 are for the 14.4 keV X-rays, curve 2 is for the 8.05 keV|Cu $K_\alpha$-X-rays. Dots - experimental data, solid lines - calculated dependences.

To solve the integral equation (3.71) for the energy intervals mentioned above using the experimentally obtained $\kappa(\gamma)$ functions (Fig.3.56), the $Q(\gamma,x)$ function must be known. The parameters required for this purpose can be obtained by an analysis of the experimental dependences $R(\gamma)$ (see Fig.3.57). These parameters obtained within the context of the rough surface model have been used to calculate the $Q(\gamma,x)$ function [3.135]. The angular dependence of the wave field in the sample is determined by two factors: (i) the intensity of the field on the sample surface $J(\gamma)$ and (ii) its penetration depth into the sample $L(\gamma)$. More accurate calculations of the $J(\gamma)$ function require that the angular dependence of the fourth energy interval be studied. A consideration of all these factors enables a solution of (3.71) to be obtained and found to be stable relative to small variations of the $\kappa(\gamma)$ function. The weight functions obtained by such method are presented in Fig.3.54 b. The accuracy is estimated to be 17 % for the second energy interval and 7 % for the first and third intervals.

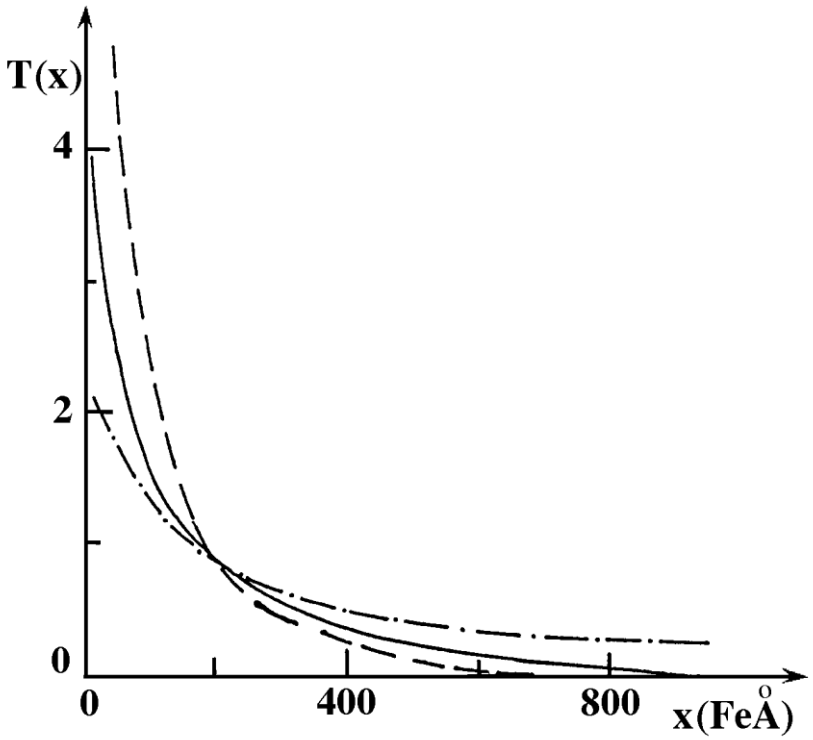


Fig.3.54b Experimentally obtained weight functions for the first three energy intervals in [3.135] (see Fig.3.50). Solid line - the first energy interval; dashed line - the second interval; dot-and-dash - the third energy interval.

A spectrum from the near-surface layer of a particular thickness or a spectrum from the bulk can only be separated in the experimental spectra if the weight functions are known. The shape and position of the layer of interest may be specified by a certain weight function $T'(x)$. This function should be presented as an expansion series over the $T_j(x)$ functions, the expansion coefficients being obtained from the simultaneous equations:

$$\sum_{j=1}^{N} T_j(x_i)\, A_{ij} = T'(x_i) \quad , \quad j = 1...N \quad ,$$

where N is the number of the known weight-functions, $x_i$ are the selected distances from the surface of the sample. Thus, it has been found in [3.136,137] that the weight function

$$T'(x) = -16.2\, T_1(x) + 12.7\, T_2(x) + 4.5\, T_3(x)$$

$T'(x) = -16.2\, T_1(x) + 12.7\, T_2(x) + 4.5\, T_3(x)$ ,

where $T_i(x)$ are given in Fig.3.54b, corresponds to the escape

of electrons from the near-surface layer which is less than 20 nm thick. If the three Moessbauer spectra corresponding to the $T_i(x)$ functions are added using the coefficients given above, a Moessbauer spectrum is produced corresponding to the selected near-surface layer. It should be noted that the quality of the spectra to be added must be high.

To illustrate the technique the authors [3.137] have solved the appropriate equations to give two weight-functions $T'(x)$ that describe the near-surface and deep layers. This allowed the separation of the spectra of Fig.3.38b into the sub-spectra corresponding to the surface layer and to the bulk (in the CEMS' sense). Thus, by means of a relatively simple procedure the depth selectivity of the spectrometer with a good energy resolution and variable angle θ [3.83] can be improved. The technique used above to obtain the weight functions is consistent and allows the functions to be obtained directly from the sample under study. The use of an X-ray tube with an iridium target (the anticathode) allows an intensive beam of the 14 keV X-rays to be produced and enables the procedure to be simplified. A certain degree of experience needs to be accumulated on the use of the weight functions in the analysis of various plane surfaces and then for rough surfaces.

It should be stressed that the weight functions presented in Fig.3.54b correspond to a particular sample-proportional counter combination. The use of another proportional counter or another method of recovering the weight function results in somewhat different weight functions. This is shown in the comparison of dependences presented in Fig.3.54 a and b. Among the reasons for such differences is the strong dependence of the weight functions on: the solid angle of electron collection, the detector efficiency for electrons of various energies and the resolving time of the detector. Thus, for example, electron spectra of very weak specially prepared $^{57}Co$ sources, taken in different laboratories with similar detectors [3.101,133], are slightly different. This is another indication of the effect of the detector design and operating mode of the counter on the detection efficiency of electrons of various energies and which emerge at different angles and appear in the active counter volume immediately after each other.

The difference in spectra discussed above is used in connection with various approaches to the quantitative interpretation of experimental data. At present there are certain empiric relations for semi-quantitative evaluations. Selecting a region of an electron spectra recorded with simultaneous detection of K-conversion and Auger electrons produces a Moessbauer spectrum from a layer of minimal thickness. Thus, if the 12 keV interval is selected, the thickness of this layer is less than $\approx$ 800 A|. On the contrary, if slow electrons (2 to 4 keV) are detected, the thickness of the analyzed layer is maximal ( $\approx$ 2000 A| ) and the relative contribution from the near surface layer is minimal. Detecting electrons in the 4 keV to 7 keV energy interval produces the same Moessbauer spectra as that recorded without any energy discrimination, i.e., the thickness of the analyzed layer turns out to be approximately 1800 A|. All of these refer to counters whose active volume is 6 mm to 8 mm thick with an energy resolution $\approx$ 25 %.

Arrangements based on proportional counters which allow an independent and simultaneous recording of CEM spectra and X-ray Moessbauer spectra in backscattering geometry, and $\gamma$-ray absorption spectra in transmission, have been developed for industrial application purposes in many institutes, e.g. [3.138-143]. Due to the different escape or penetration ranges of the three radiations involved, the spectra give information on phases, depth and orientation. From a practical point of view the counters for $\gamma$-rays, X-rays and electrons must be separated and shielded to ensure independent detection.

Kamzin and Grigor'ev [3.141-143] describe a proportional gas-flow counter for Moessbauer studies at temperatures of 100 - 750 K in which conversion electrons and characteristic X-rays are detected in backscattering geometry and gamma quanta are detected in transmission geometry. The working gases are He+5% $CH_4$ for conversion electron and Ar+5% $CH_4$ or Xe+5% $CH_4$ for X- rays and gamma quanta. The counter is designed for comprehensive Moessbauer studies of the surface and internal properties of materials.

An experimental setup for simultaneous recording of CEM spectra and of X-ray Moessbauer spectra and absorption spectra in transmission developed by Schaaf et al. [3.138-140] is shown in Fig. 3.58. Due to the different penetration depths of the

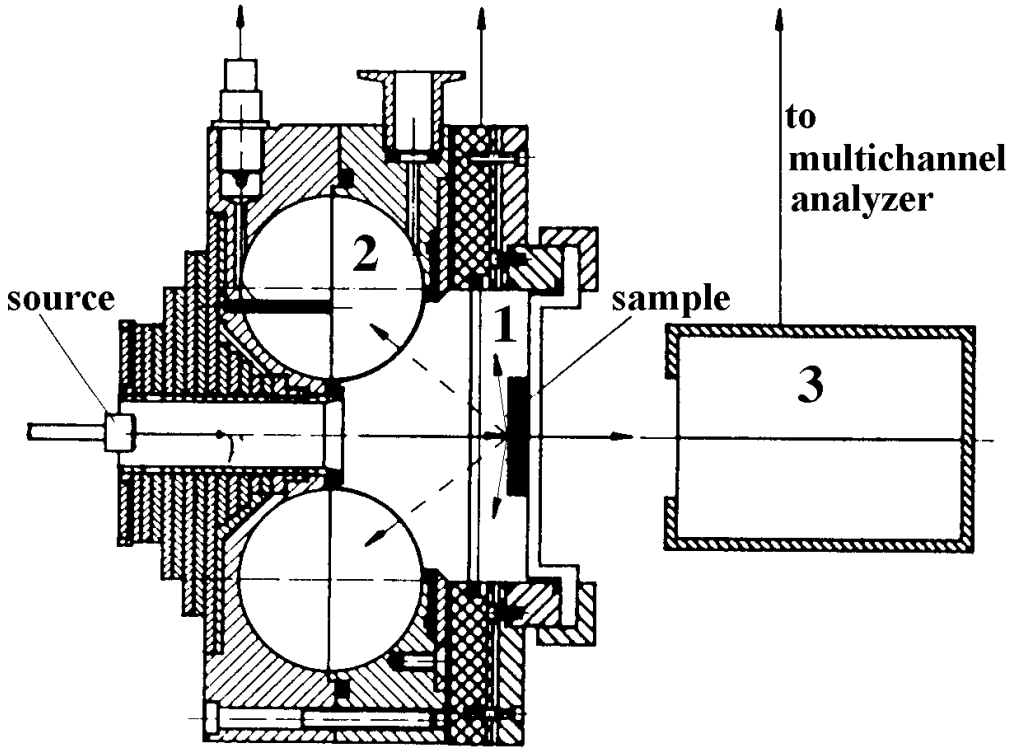


Fig.3.58 Set up for simultaneous recording of CEM spectra (1), X-ray Moessbauer spectra (2) and absorption spectra in transmission (3) developed by Schaaf et al. [3.139].

three kinds of radiation involved, the simultaneous application of these three methods to the same specimen constitutes a discrete depth profile analysis. The authors called it simultaneous triple radiation Mőssbauer spectroscopy (STRMS). The authors demonstrate the simultaneous measurement of the spectra to investigate the changes of the metallurgical state of $Fe_{79}B_{16}Si_5$ foils (Metglas 2605 S2) subjected to pulses of an excimer laser. Before the irradiation no great differences between the three spectra of the Metglas can be seen. After irradiation, dramatic changes are observed in the X-ray Moessbauer spectra and absorption spectra The drastically reduced relative intensity of the $\Delta m = 0$ lines in the spectra can be interpreted by a spin orientation preferentially perpendicular to the plane of the ribbon (see fig. 3.59 from [3.139]).

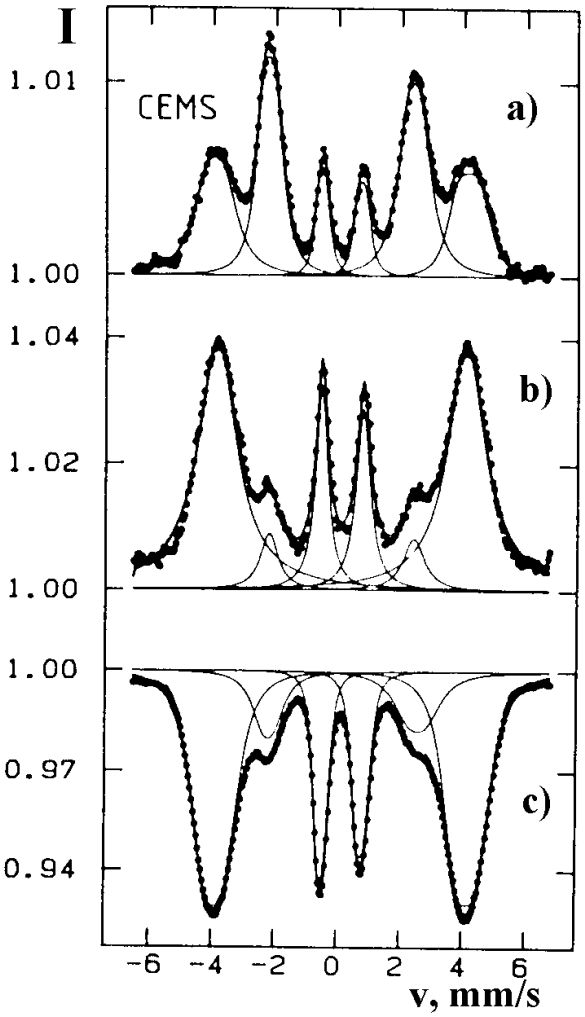


Fig. 3.59 Mőssbauer spectra of laser treated foil of amorphous Metglas 2605 S2 (25 μm thickness); a) CEM spectrum; b) X-ray Mőssbauer spectrum; c) absorption spectrum.

## 3.9. Analysis of Thin Layers under Total External Reflection of Mössbauer Radiation

As has been shown in Sect.3.6 the thinnest layers to be studied in Mössbauer spectroscopy are those studied by GA DCEMS. Nearly the same thin layers may be studied by detection of all back-scattered electrons when the radiation is incident at a glancing angle $\gamma \leq \gamma_{cr}$. A similar situation has been discussed in Sect.2.5, where scattering experiments were considered with the detection of $\gamma$-quanta. For a scatterer of $\alpha$-Fe, the field penetration depth into the sample is approximately $\cong$ 3 nm and $\gamma_{cr} \cong$ 3.8 mrad. On Fig.3.60 a typical set of TER spectra obtained at angles in the region of $\gamma_{cr}$ are shown. The sample under investigation was an $\alpha$-$^{57}$Fe (a = 90%) layer about 30 nm thick deposited on a polished beryllium disk 50 mm diameter and 10 mm thick. In this case the nonresonant backscattering was small and this results in diminishing background counts and an increase in the Mössbauer effect value in comparison with the same sample on a glass substrate. The layer thickness was determined from reflection curves for $CuK_{á}$ radiation using Kiessig oscillations. The sample has been sawn into two parts in order to use one of them as reference. This sample was put into a vacuum chamber. CEM spectra from these two samples measured after an interval of several months were identical in the limits of statistical error. That is, oxide layers on the top of the samples under investigation were created before the beginning of the first measurements, and further oxidation did not occur. Most probably the oxidation took place during the evaporation of iron onto the substrate.

The spectra of these samples at $\gamma$ = 2.2 mrad (see Fig.3.60a) are similar to the sextet from metallic iron. The spectra in Fig.3.60b and c are typical interference spectra at TER conditions. At energies greater than the greatest resonance energy constructive interference enhances the counting rate and at energies less than the smallest resonance energy destructive interference takes place. It results evidently in the difference in the baselines of the Mössbauer spectra in Figs.3.60b and c at positive and negative velocities. Interference also leads to an asymmetry of the resonant scattering peak. The asymmetry agrees with a classical model of scattering by a damped resonator (an isolated atom), i.e. resonant scattering is in phase with Rayleigh scattering when the incident radiation energy is above resonance but is in anti-phase when below resonance and in quadrature when on exact resonance. Because interference effects are observed in scattering from a real sample and not from an isolated atom the interference pattern may be unambiguously connected with the composition and effective thickness of the layer under investigation, crystallographic and electronic structure and so on. However it is very difficult practically to extract the information on the phase composition from such spectra.

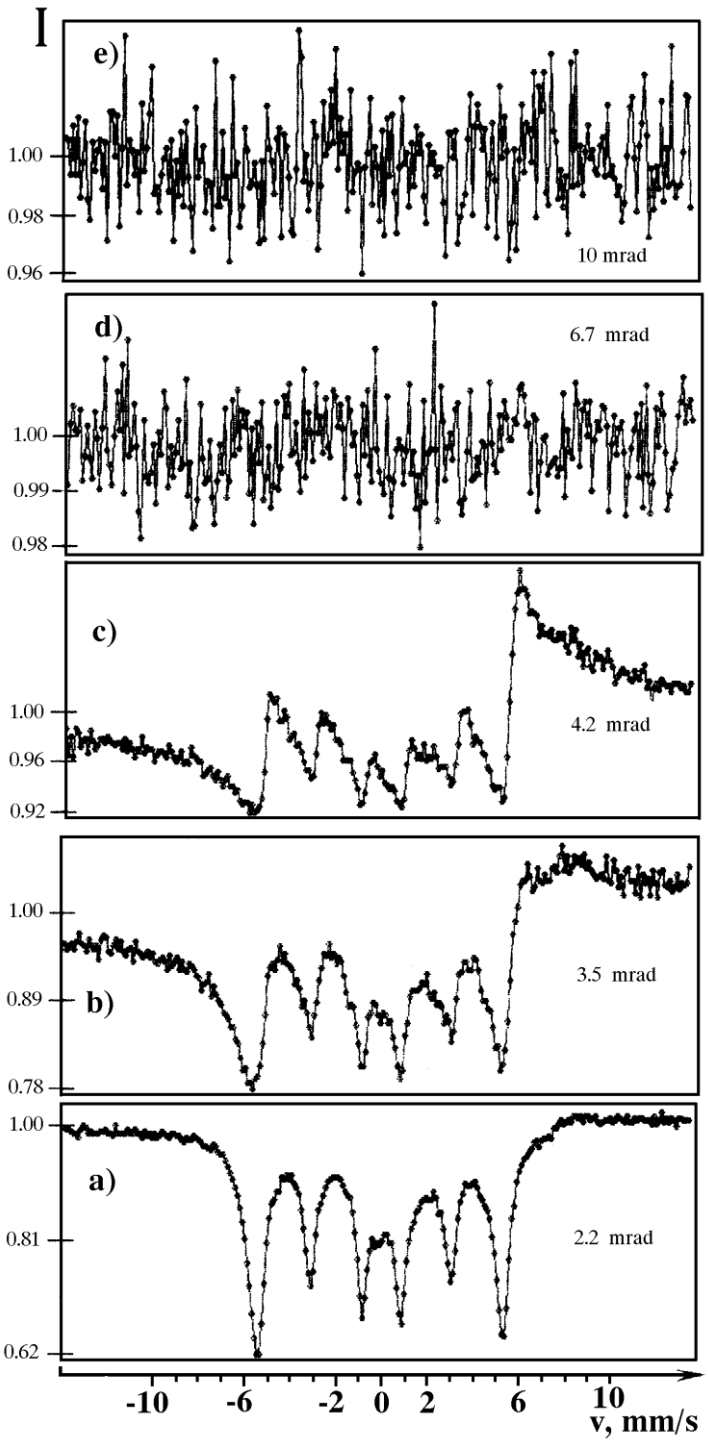


Fig.3.60 Experimental Mössbauer scattering spectra for geometry (set up) shown in Fig.2.24 at glancing angles 10 mrad $\geq \gamma \geq$ 2.2 mrad. The scatterer is an $\alpha$-$^{57}$Fe (a = 90%) layer about 30 nm thick deposited on a polished beryllium disk 50 mm in diameter and 10 mm thick.

A correct estimation of the contribution from Rayleigh scattering to the total intensity of the scattered radiation is important when attempting to describe how the line shape depends on the geometry of the experiment. The appearance in the Mössbauer spectrum of a dip instead of a peak may in the first instance be associated with resonant absorption which leads to a sharp reduction of the penetration depth (at TER it is the path length) where Rayleigh scattering occurs (see Sec.2.5 and 4.4). At $\gamma$ = 2.2 mrad the path length of Mössbauer radiation in the near surface layer is maximal and the contribution of Rayleigh scattering to the Mössbauer spectrum is minimal ( compare Figs. 3.60a and c). At $\gamma \geq$ 6.7 mrad there is no Mössbauer spectrum. The $\gamma$ -rays penetrate the sample to a greater depth than the layer under investigation, and the contribution of nonresonant scattering channels to the total intensity of scattered $\gamma$ -rays is much greater. As a result we cannot see any Mössbauer spectrum in an acceptable measurement time (see Figs. 3.60d and e).

We can exclude the interference effects by detection of the secondary radiation for this type of experiment, at least for the M1 transition in $^{57}$Fe. As the secondary radiation one can record not only electrons, but X-rays and even $\gamma$-rays, if the $\gamma$-ray detector counts do not mirror reflected $\gamma$-rays, but all radiation backscattered by the sample under investigation in $2\pi$ radians. Experimental observations of TER using electron detection were discussed in [3.144-145]. The first practical application of TER - the use of this effect to transmit resonance gamma radiation over long distances - is described in [3.146].

Now, in the geometry of Fig.2.24, let us detect electrons using a dual proportional counter. Any electron back-scattered at $\gamma \leq \gamma_{cr}$ escapes the surface. Moreover, about 20 % of electrons scattered into the lower hemisphere will also reach the surface. The number of electrons escaping the sample surface after a scattering event may be expected to be $\approx$ 15 times as large as the number of $\gamma$-quanta. It is essential that interference effects do not influence the line shape, as was the case when $\gamma$-quanta are detected (compare the sets of spectra on Figs.3.60 and 3.61). For a scattering angle of $90^{\circ}$, the spectrum is a superposition of Lorentzian lines. As the scattering angle is decreased below $\gamma_{cr}$, the shape of the spectrum becomes distorted, and a broad component characteristic of ferric oxides appears. One can say that for electron detection the shape of the Mössbauer spectrum does not change drastically as the scattering angle $\gamma$ varies (compare the spectra in Figs. 3.60 and 3.61).

Sometimes oxide layers thicker than those on the sample characterized by the spectra in Fig.3.61 developed during the evaporation, but in all cases the experimental spectra are a superposition of a sextet from the bulk $\alpha$-Fe layer, a smeared sextet from oxides and a doublet from very fine ferric oxides. Some asymmetry in the spectrum shape at positive and negative velocities makes interpretation of the data difficult. The method of analysis of thin layers under TER of Mössbauer

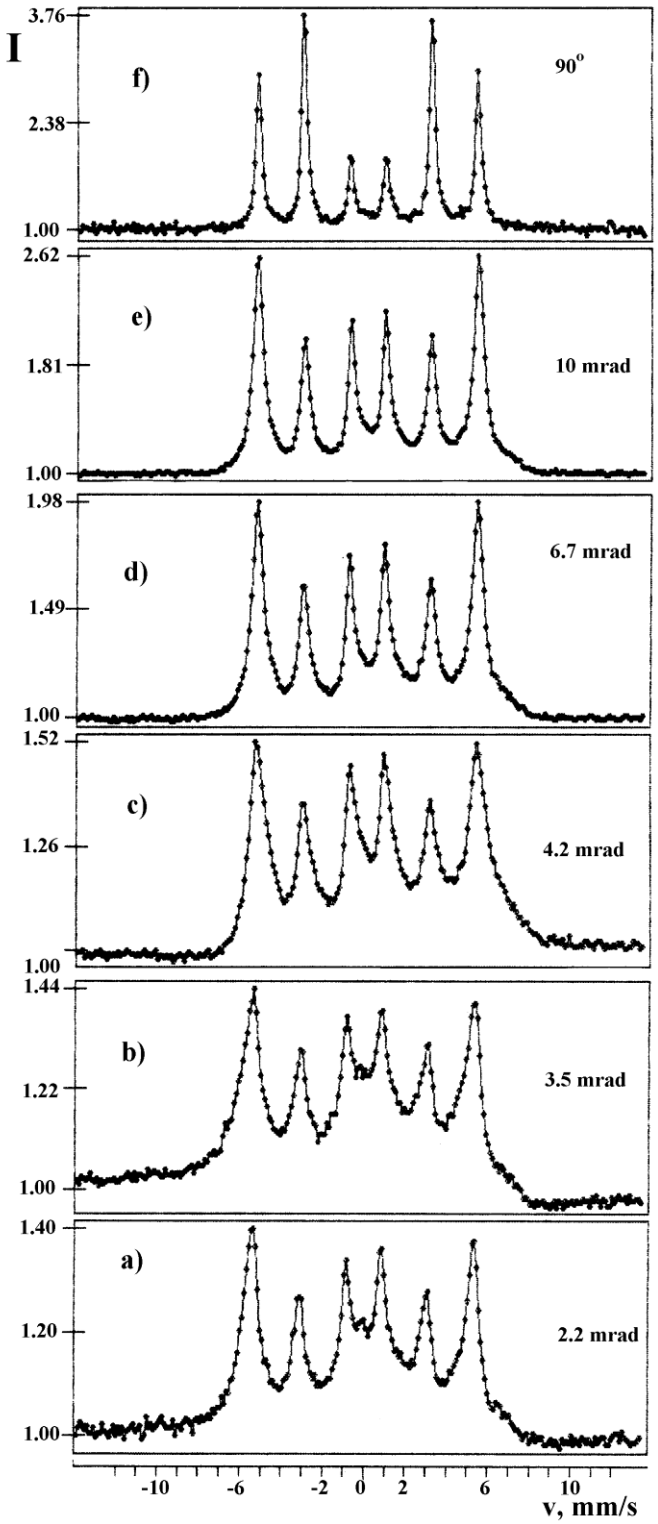


Fig.3.61 Experimental CEM spectra at glancing angles 10 mrad $\geq \gamma \geq$ 2.2 mrad and at normal incidence. The scatterer is an $\alpha$-$^{57}$Fe (a = 90%) layer about 30 nm thick deposited on a polished beryllium disk.

radiation was developed in [3.147]. The calculation of the secondary radiation yield consists of four stages: determination of the amplitude of the specularly reflected wave; determination of the field amplitude at different depths inside the film and calculation of the escape of secondary radiation for the weight functions proposed by D. Liljequist (see Sec. 3.3 and 3.4). The results of the calculation and the fitting of the experimental spectra are very sensitive to the model of surface layer structure and to the density of the top layer. Typical results of such fitting for a model in which an $\alpha$-Fe layer is covered with oxides (fine oxides which are responsible for the doublet in the Mössbauer spectrum correspond to the oxide top layer and the smeared sextet describes the intermediate layer in which the magnetic interaction is characterized by a broad distribution of hyperfine parameters) are shown in Fig. 3.62.

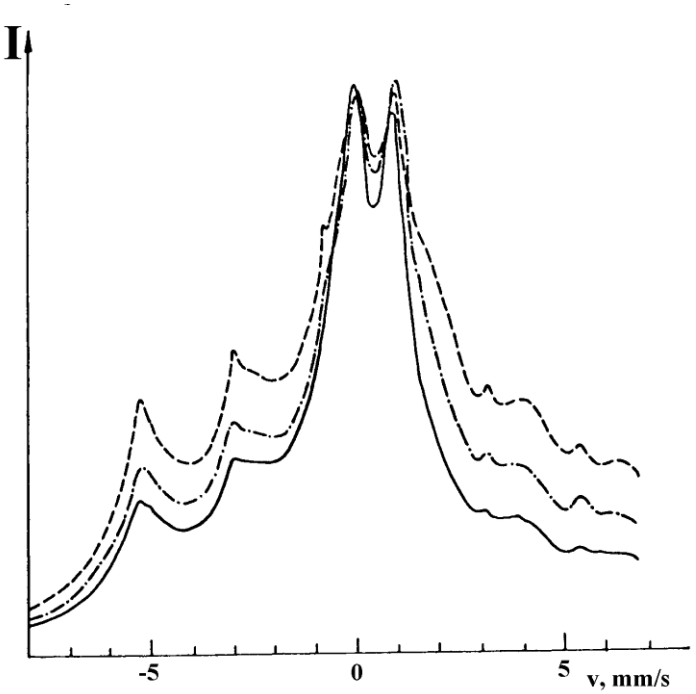


Fig.3.62 Theoretical CEM spectra at a glancing angle of 3.8 mrad for two different values of the density of the top layer: normal (solid line), decreased by a factor of two without changing the "effective thickness" of this layer (dash- dotted line), and for the case when 50 % of the nuclei characterized by the smeared sextet are included in the first layer (dashed line).

From the analysis of the experimental spectra one can conclude that the most finely dispersed oxides (the doublet in the spectrum) are predominant on the near-surface layer. As $\gamma$ decreases to $\gamma_{cr}$ the relative area under the spectrum increases by a factor of more than 5. However, it is difficult to be certain of the depth distribution of the oxides producing the smeared-out sextet. The proportion of these oxides is likely to be less in the near-surface layer than near to the $\alpha$-Fe layer below. On the basis of the theory of CEMS spectra in the total

reflection geometry for the model suggested in which the layers partly penetrate each other, the results are quite acceptable.

After oxidation of the samples the spectra may be more complicated and with $\gamma$-ray detection we practically cannot do any quantitative phase analysis. For example, with the above mentioned sample after oxidation at 175°C for 4 hours and then 270°C for 4 hours the signal from $\alpha$-iron has practically disappeared, (see Fig.3.63). The analysis of the same samples with electron detection enable us to easily discern the signal from $\alpha$-Fe and to do near surface layers analysis (compare spectra on Figs.3.63 and 3.64).

One can say that there are no interference phenomena in TER with electron detection and the method is suitable for surface analysis.

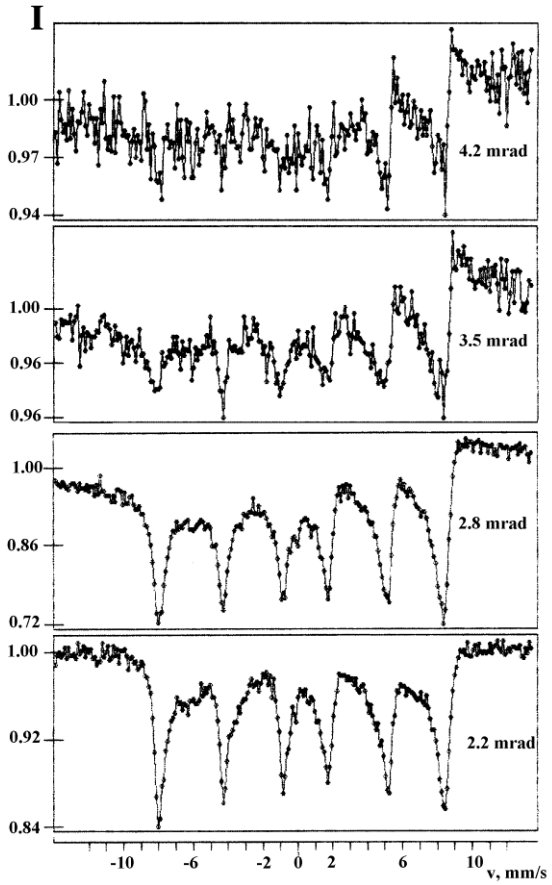


Fig.3.63 Experimental Mössbauer scattering spectra for set up shown in Fig.2.24 at glancing angles 4.2 mrad $\geq$ ã $\geq$ 2.2 mrad. The scatterer is an $\alpha$-$^{57}$Fe (a = 90%) layer about 30 nm thick, deposited on a polished beryllium disk, oxidyzed at 175°C for 4 hours and then 270°C for 4 hours.

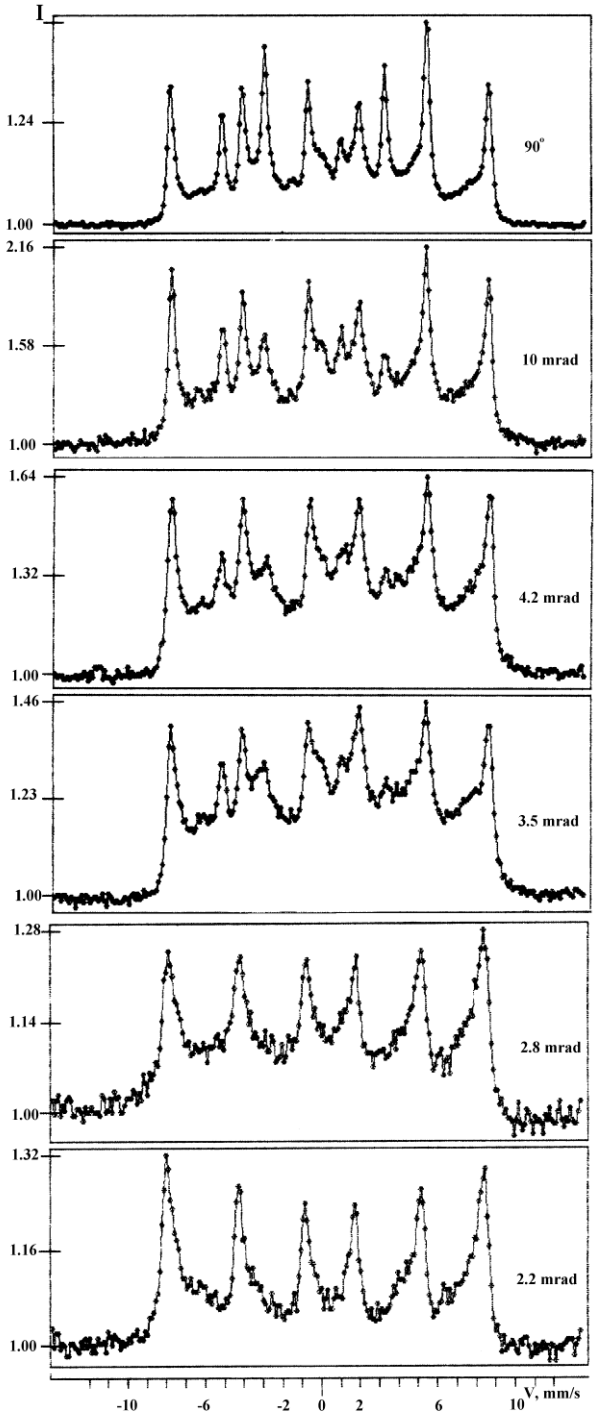


Fig.3.64 Experimental CEMS spectra for set up shown in Fig.2.24 at glancing angles 10 mrad $\geq \gamma \geq$ 2.2 mrad and at normal incidence. The scatterer is an $\alpha$-$^{57}$Fe (a = 90%) layer about 30 nm thick, deposited on a polished beryllium disk, oxidyzed at 175°C for 4 hours and then 270°C for 4 hours.

However, a thorough analysis of the spectra in Fig.3.61 shows us that near $\gamma_{cr}$ the intensities of the baseline at positive and negative velocities are different and the difference changes at $\gamma_{cr}$. For the interpretation this quasi interference phenomenon [3.148] one needs to consider the escape of electrons to the surface of a bulk sample. The photoelectric effect on K- and L-shells of Mössbauer atoms leads to the emergence of electrons with an energy equal to the energy of conversion electrons from the same shells. Generally in Mössbauer spectroscopy the background due to the photoelectric effect determines only the effect value $\varepsilon$, but not the spectrum shape. This is not the case near $\gamma_{cr}$, because at TER the amplitude of the mirror reflected electromagnetic wave has an anomalous dependence on $\gamma$-ray energy (relative velocity). As a result the electron escape also has an anomalous dependence on $\gamma$-ray energy which produces a difference in background intensity at energies above and below the resonance energy. This anomaly is observed near $\gamma_{cr}$ and is very small far from $\gamma_{cr}$.

On reflection at angles less than $\gamma_{cr}$, the electromagnetic field intensity falls off rapidly. The penetration depth for the radiation (i.e. the thickness L of the layer under study) is taken to be equal to the depth at which the intensity is reduced by a factor of e. At $\gamma < \gamma_{cr}$ the penetration depth for the radiation is much less then the escape depth for the electrons and all of this radiation can be transformed into secondary radiation. If the reflectivity is less, then the intensity of photo electrons is greater. A similar dependence was found in TER of X-rays in [3.149].

At $\gamma > \gamma_{cr}$ the penetration depth for the radiation grows rapidly. The number of electrons escaping depends on the amplitude of the electromagnetic wave near the surface. More photo electrons escape in the region where the amplitude of the electromagnetic wave is greater. The asymmetry of the baselines in Fig.3.61b and c has changed. The growth in the photo electron intensity near $\gamma_{cr}$ was observed in [3.150]. The magnitude of the asymmetry is determined by weight functions. In our calculations [3.148] it was shown that if the intensity of photo electrons is about 10 % of the intensity of resonance electrons one can explain the experimental results. That is, even for enriched samples the yield of photo electrons must be take into account to interpret the experimental Mössbauer spectra.

Thus, at angles less than $\gamma_{cr}$ resonant scattering occurs in a very thin layer. No energy resolution is required here, and, at the same time, such surface selectivity cannot be attained even with a $\gamma$-spectrometer having $R \approx 1.3$ %, $\theta = 45°$ (see Fig.3.29). Similar selectivity is likely to be reached only with electrostatic $\gamma$ -spectrometers whose accuracy of energy determination is about 1 eV and the half-width is 10 eV at 7.3keV [3.54,55,59]. It is interesting that the authors of [3.138,139] did not take special measures to polish very thoroughly the surface under investigation and, probably, the surface roughness was greater than the thickness of the analyzed layer. One can say that the $\gamma$-quanta "see" an averaged plane surface.

An essential characteristic of any method of research is the time required to obtain information with a specified statistical accuracy. The problem of separating signals of interest from the background and problems of statistical accuracy are general and very important for the whole of Mössbauer spectroscopy, but it is of special importance for TER. This is partly due to the limited strength of Mössbauer sources and the fact that the intensity of the detected scattered radiation is generally only a small fraction of the incident intensity. The intensity loss of the scattered radiation at TER of more then three orders of magnitude makes it necessary to compare both the sensitivity of the two methods and the quality of the spectra obtained using $\gamma$-ray and electron detection. The quality of a spectrum is directly related to the quantity of information contained in the spectrum and is a more general parameter then the sensitivity.

The quality of a spectrum is determined by the intensity and the effect value. Let us compare the data for $\gamma$-ray and electron detection for the set up presented in Fig.2.24. For a source of about 200 mCi and using electron detection the intensity for a 256 channel spectrum is about 100 - 300 counts per hour and maximal at $\gamma$ = 10 mrad. The greatest effect value $\varepsilon$ is also at $\gamma$ = 10 mrad, $\varepsilon$ = 160 %. At $\gamma$ ~ 3 mrad $\varepsilon$ ~ 45 %. Using $\gamma$-ray detection the intensity increases as the grazing angle $\gamma$ decreases, and is about 150 - 200 counts per hour per channel, that is, a little more than that obtained using electron detection. The effect value is close to 40 %. At $\gamma < \gamma_{cr}$, the effect value increases due to the enhanced signal-to-noise ratio since the photoelectric effect mainly determining the background takes place only in a very thin layer. One can say that at $\gamma$ = 2.2 mrad the quality of spectra are approximately the same, but at larger grazing angles the quality of spectra using $\gamma$-ray detection is poor and the spectra disappear at 10 mrad. The simultaneous detection of X- or $\gamma$-rays by dual proportional counter is very useful for the interpretation of experimental data, but , unfortunately, it requires approximately an order of magnitude longer measurement time, which is not acceptable for most applications.

The extremely rigid limitations imposed on collimation of the incident radiation result in a large source-scatterer distance and a very low count rate. The moderate brilliance of traditional Mössbauer sources has until recently prevented wide spread use of the method. New methods of extracting Mössbauer radiation from synchrotron beams are opening up a new stage in the development of TER. The high brilliance, extremely narrow bandwidth ($10^{-6}$ - $10^{-8}$ eV) and angular width of about 0.4 arc sec with no additional collimation of this radiation will stimulate application of the method to surface studies. Modern TER Mössbauer spectrometers [2.57] can operate with an ordinary Mössbauer source as well as with a synchrotron beam. The specific feature of the spectrometer is that it allows Mössbauer spectra to be recorded in a wide range of glancing angles over three independent detection channels: $\gamma$-ray, electron or X-ray detection.

### 3.10. Other Methods of Detection in CEMS

In addition to the proportional counters, other types of gas-filled detectors are used in CEMS. One of them is the parallel-plate avalanche counter (see, e.g.[3.151]). In Mössbauer spectroscopy such detectors have been used by WEYER [3.29] as resonance detectors and at higher counting rates. These counters have found application in surface studies [3.152,153].In a uniform electric field between two electrodes electrons and ions will cause avalanches to spread towards the electrodes. The average number of electrons in an avalanche increases exponentially with the distance from the location of the primary ionization event. When the primary ionizations are uniformly distributed in the active counter volume and because of the statistical fluctuations in the number of electrons (particles) in an avalanche, an energy resolution for the conversion electrons is not possible.

A typical design of the counter is presented in Fig.3.65 which consists of two systems of parallel electrode plates (A and B).

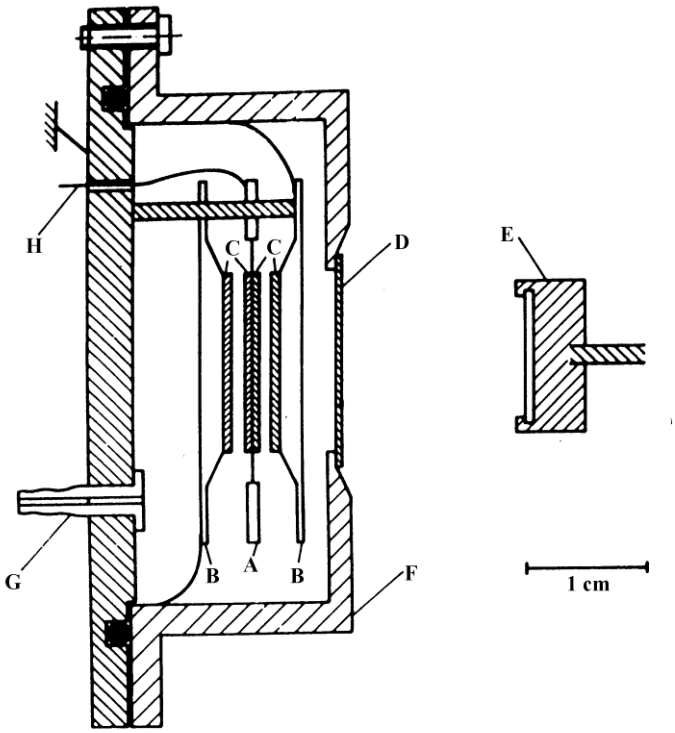


Fig.3.65 Parallel-plate avalanche counter (from [3.29]).A, B - parallel-plate electrode system; C - resonance absorber material; D - thin entrance window; E - source; F - counter housing; G - gas inlet; H - high voltage.

The substance under investigation (C) covers the cathode surface and the incident resonant radiation passes through the anode B made of a low-Z material. The counters were used with a pair of electrodes, one of them being a metal mesh placed above the surface of the sample for studies of comparatively thick samples with an imperfect surface. The gas- filled counter volume is connected to a gas reservoir through a gas inlet tube (G). Gases of acetone vapour or a He + 10 % $CH_4$ gas mixture at 10 to 40 Torr were used. The reduced pressure is needed to ensure the long-term stability of the counter and for suppressing the detection efficiency for very high-energy $\gamma$-quanta. This counter is an effective tool for the registration of low-energy (0.3 < 1 keV) electrons, which are practically impossible to detect with the proportional counter.

An advantage of the avalanche counters is their possible use for the study of large-area samples. Besides, the use of a needle-shaped anode allows areas approximately 2 mm diameter to be studied. [3.154]. The main disadvantages of the detectors are the dependence of the counting rate on the applied voltage and the gas-fill composition, and also the more complicated design as compared with the flat proportional counter.

The design and operating principles of the avalanche counters used in CEMS, as well as a comparative analysis of the integral mode of operation of proportional counters, have been considered in [3.5,29,155]. The analysis had shown that with the avalanche counter a greater observed effect is obtained. Thus, for example, with a scatterer of $\alpha$-Fe (2.14 % $^{57}$Fe) $\varepsilon_2$ = 18 % compared with $\varepsilon_2$ ~8 % for the same scatterer when a proportional counter is used. With the parallel-plate avalanche counters, the spectra quality may be higher. Problems arising in studies of non-conducting surfaces (the cathode is an insulator) have been successfully overcome [3.156].

If the internal conversion of a Mössbauer transition is followed by emission of Auger electrons, which have much lower energy than the conversion electrons, parallel-plate avalanche counter allows a new method of depth selective analysis to be used. Indeed, if the energy of Auger electrons is low these may be difficult to detect in a gas proportional counter since their energy may not exceed the noise level. Due to the efficiency of this counter for the low-energy electrons, Auger and conversion electrons may be distinguished by their different signal heights under favorable conditions.

This was demonstrated by WEYER [3.157] in surface studies of natural tin foils which were oxidized in air and used as either cathodes or anodes of a parallel-plate avalanche counter. After the internal conversion of the 24 keV M1 transition of $^{119}$Sn mainly two groups of electrons are emitted (see Table 3.1): L-,M- conversion electrons ($E \geq 19.6$ keV, $C_i \approx 0.83$) and Auger electrons related to $L_1$- vacancies ($E \leq 3$ keV, $C_i \approx 0.74$) and to M-shell vacancies ($E \leq 0.8$ keV, $C_i \approx 0.8$).

Because of the large energy difference between the conversion and Auger electrons, it is suggestive to assume that the signals with different pulse heights supply information on near-surface layers of different thickness. The intensity of the conversion electrons in the low energy tail of the transmission probability decreases approximately exponentially with increasing energy loss. Thus the intensity of these electrons decreases by more than two order of magnitude for energies below 3 keV, i.e. the maximum energy of the Auger electrons. Therefore, in this energy region the Auger electrons intensity exceeds that of the conversion electrons by about an order of magnitude.

In the pulse-height spectrum from the detector the different windows were set for the different Mössbauer spectra. The spectra are a sum of two sub-spectra: the bulk - β-Sn and a $SnO_2$ - surface layer. The ratio of the effect values for these two sub-spectra for the sample may be used as a measure of the surface selectivity of the method. The ratio varied from 1 to 6 which depends on the detector configuration. The layer thickness was estimated to be 15 nm and the surface sensitivity < 5nm. The depth scale as determined by the range of Auger electron, from the outer shells for many Mössbauer isotopes is $\leq$ 10 nm. It is an intriguing property of the parallel-plate avalanche counter that the gas mixture and pressure and the geometrical dimension can easily be adjusted over a wide range as to meet the requirements which lead to a larger pulse height for low energy than for high energy electrons. Because of the high electron detection efficiency this enables the measurement of reasonable spectra in a relatively short time for $^{57}$Fe, $^{119}$Sn, $^{151}$Eu, $^{161}$Dy and $^{169}$Tm.

In addition to the techniques based on the gas-filled counters other electron detection methods have been used in Mössbauer spectroscopy. First, scintillation detectors may be considered. Thin organic (crystal or plastic) scintillators are used for detecting electrons. The low quantum yield of such scintillation detectors results in an unfavorable signal-to- noise ratio on detecting electrons with the energy of about 10 keV. An advantage of these detectors is the recording of CEM spectra at low temperatures and from samples placed in any gas environment (not destroying the scintillator). This is not possible with gas-filled ionization-detectors or channeltrons.

In order to use scintillator detectors in CEMS, coincidence techniques may be used. Thus, for example, in [3.158] to observe CEM spectra from $^{119}$Sn, a film-plastic scintillator on a prism-shaped acrylic-resin light guide was placed between two photomultiplier tubes. The output signals from the tubes were fed to a coincidence circuit and summed. With a scatterer of $SnO_2$ the effect value exceeded 1000 %.

Electrons of lower energies are especially difficult to detect. An example is CEMS of $^{57}$Fe, where the average energy of electrons of interest is much lower than 7.3 keV.

Furthermore, certain energies are lost upon the passage of electrons through the reflector of the crystal scintillator. This results in an especially unfavorable signal-to-noise ratio. Nevertheless, scintillators are used at present for detecting the $^{57}Fe$ K- conversion electrons in resonance detectors (organic scintillators) [3.159]) and in $\gamma$-spectrometers for DCEM involving the detection of the $\approx$ 7 keV electrons [3.160] wherein an inorganic scintillator $Y_2SiO_5(Ce)$ has been used (1 mg/cm$^2$ thick and cooled down to -30°C).

Gas scintillation proportional counters with a good energy resolution (e.g., R $\approx$ 8% at 6 keV) have not been constructed for CEMS. However, techniques based on the detection of conversion electrons by light scintillations do find application in CEMS. The composition of a gas mixture and the detector designs most efficient for detecting low-energy electrons have been described [3.161,162]. For the proportional mode of operation a mixture of He + 1 % $N_2$ is recommended. In the operating mode of the ordinary scintillation detector the concentration of nitrogen may be lowered to 0.005 %, or a He-Ne mixture may be used. This operating mode is most efficient for obtaining CEM spectra from surface fractures, i.e., when the applied electric field may be considerably distorted or streamers and discharges may occur.

The counter described in [3.163] has another operating principle. If a K-conversion or Auger-electron enters the electric field region between the two electrodes to which a potential difference is applied, microdischarges are produced. Scintillations following the microdischarges have a duration of $10^{-8}$ to $10^{-7}$sec. These can be detected by photomultipliers and the resulting background pulses formed by the random noise of the photomultiplier may be eliminated by use of a discriminator. The voltage required for microdischarges to appear is applied to the photocathode of the photomultiplier allowing scatterers of any shape to be studied. The relaxation of atomic shells excited by resonant scattering will be followed by the emission of low-energy electrons and also by the emission of light. Mössbauer spectra can be obtained by detecting these photons from an approximately 100 nm thick layer [3.164].

The coincidence technique used in CEMS must now be considered in more detail. It has already been mentioned that one of the limitations of depth selection is that electrons of various energies are detected together, and only in the APK energy interval is the situation somewhat simplified. The coincidence technique allows the selection of only the K-shell conversion electrons if the coincidence circuit is controlled by a signal from the K-X-rays [3.165]. Depending on whether the coincidence circuit is used or not, electron spectra obtained from a stainless steel scatterer with a flat proportional counter 2.5 cm thick (R $\approx$ 18 % at 6.5 keV) are quite different [3.166]. The energy resolution of this counter allows selection of at least four non-overlapping intervals within the 0-7.3 keV energy range. The comparison of Mössbauer spectra corresponding to these intervals demonstrates the good depth sensitivity of the technique. On scattering from a uniform bulk scatterer, the depth dependence of the Mössbauer effect value can be used as a criterion for testing the weight functions chosen for conversion electrons. For depth selection in CEMS, two multiwire proportional chambers may be used with an X-$e^-$ coincidence circuit [3.167].

Semiconductor detectors can also be used in CEMS. Their main problem is the possible absorption of electrons of interest in the entrance window. However, silicon n-type surface barrier detectors with a 50 $mm^2$ entrance window have been used to obtain $^{57}Co$ electron spectra with an energy resolution of 660 eV on the 7.3 keV line and 600 eV on the 13.6 keV line [3.168]. Based on this electron detector and the "miniorange"-type magnetic filter, a DCEM spectrometer has been developed [3.70]. Electrons escaping the sample surface in the 3 keV energy interval for the 7.3 keV electrons, and in the 6 keV interval for the 14 keV electrons were focused by the miniorange onto the detector window. The spectrometer allowed depth selectivity in the 1000 A| - 5000 A| range.

Thus, in conclusion, almost any detector of low-energy radiations can, after proper adaptation, be used in CEMS. The detectors and techniques are summarised in Table 3.6.

Table 3.6
Detectors and electron detection techniques in CEMS

| with Energy Resolution | | without Energy Resolution |
|---|---|---|
| Electron Spectrometers | Magnetic | Parallel-plate Avalanche Counters (PPAC) |
| | Electrostatic | Channel Electron Multipliers (CEM) |
| Ionization Detectors | Proportional Counters | Gas Scintillation Detectors |
| | Multiwire Proportional Counters | Microchannel Plates |
| | Semiconductor Detectors | Windowless Multipliers |
| | Gas Scintillation Proportional Counters | Organic Scintillation Detectors |
| | X-rays Controlled Proportional Counters | Detection of Light Produced by Microcharges |
| | | Geiger-Müller Counters |

### 3.11. Channeltrons and the Detection of Very-Low Energy Electrons

Channel electron multipliers (channeltrons) have played an important role in CEMS. Channeltrons, microchannel plates and windowless electron multipliers constitute a special group of detectors for CEMS. These have no entrance windows and are designed for vacuum operation which can be used to advantage in CEM spectrometers operating both at high and low temperatures. In addition, there is no problem of electron absorption by the entrance window as found in the gas-filled and scintillation counters (cf. Fig.3.26a and b). Initially, CEMS using these detectors (Mössbauer spectroscopy) has found numerous applications in low-temperature and clean surface studies. Then a new method of surface study has appeared - CEMS based on the detection of very low energy electrons.

Detectors in this group have no energy resolution. The pulse-height distribution at the output of these detectors is similar to the noise distribution. Windowless multipliers as detectors were first used in DCEMS [3.46,49], and then in conventional CEMS [3.170]. Being less convenient than channeltrons, they have not found wide applications in Mössbauer spectroscopy.

In contrast, channeltrons are widely used both in CEMS and in DCEMS. Both commercial channeltrons [3.45,171,172] and specially designed channel electron multipliers have been used for CEMS [3.173]. The entrance diameter is about 2 cm and the efficiency of the channeltron for low-energy electrons is high reaching 90 % for the energy of about 300 eV (see Fig.3.66).

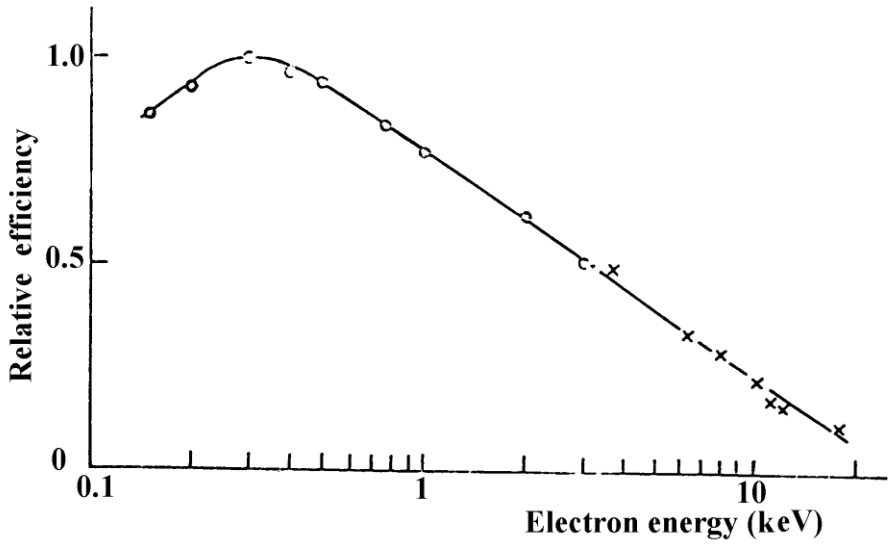


Fig.3.66 Efficiency of the channel electron multiplier (from [3.54]).

There are at least three technique in CEMS, where the use of the channeltron has proved to be most effective, (i) low temperature CEMS studies [3.173-176], (ii) studies of very clean surfaces and (iii) the detection of electrons with an energy less than 100 eV.

One design for a CEM spectrometer operating at the liquid He temperature is given in Fig.3.67. The beam of $\gamma$-quanta enters the helium dewar through a beryllium window and falls at 45° upon the surface of the sample, which is in thermal contact with the He reservoir. Electrons are focused onto a channeltron at room temperature by the longitudinal magnetic field that can be changed by varying the current through the coils. To prevent the oil vapours from entering the cryostat, a liquid nitrogen trap was used. Nevertheless, the gases remaining in the cryostat volume at a pressure of $\approx 10^{-6}$ Torr condense on the colder sample surface causing the electron counting rate to decrease in two days by 30 %. A disadvantage of this experimental arrangement is the large sample-detector distance, resulting in a low electron count rate. An advantage is the possibility to change the magnetic field and detect electrons in various energy intervals which allows a depth selection to be made.

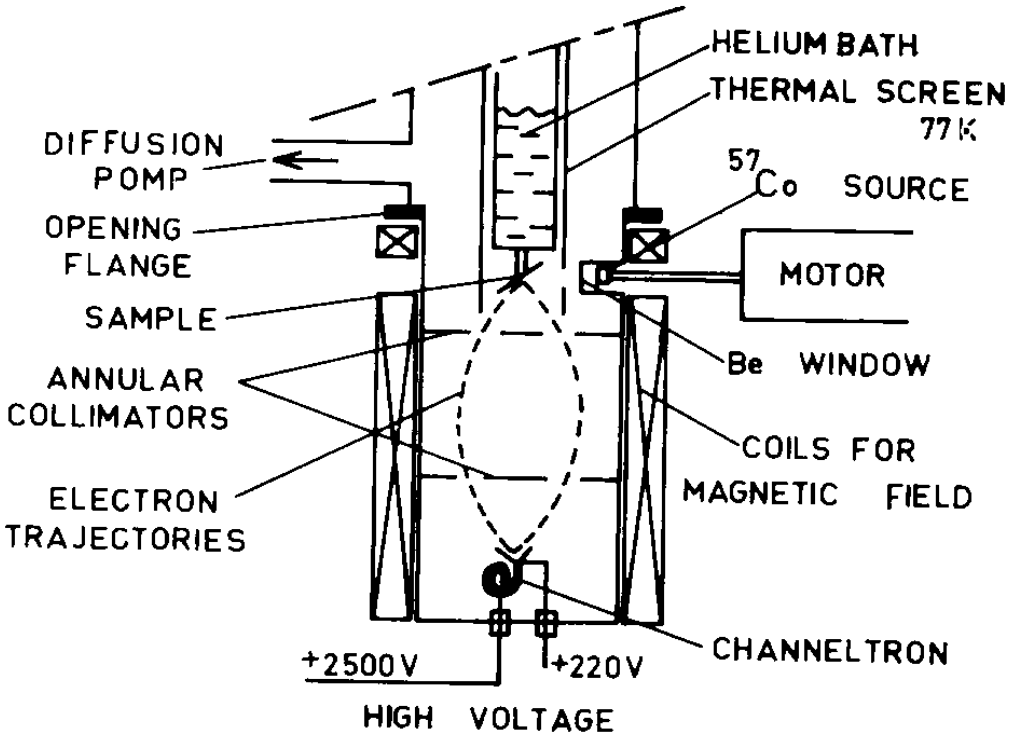


Fig.3.67 CEMS spectrometer used to measure the spectra at 4.2 K (from [3.174]).

If a channeltron and a scatterer are at the same temperature, they can be placed close to each other and a considerable increase of the count rate may be achieved. The commercially available channeltrons are not recommended for use at low temperatures (below 250 K). However, some specially designed detectors have been reported to operate in the temperature interval between 4.2 K [3.174] and 500 K [3.177,178]. Thus, for example, the spectrometer described in [3.174] with a channeltron enable the measurement to be made at 4.4 K one hour after changing the sample. This is much quicker than with a spectrometer with a channeltron described in

[3.178]. The spectrometer has a very high signal-to-noise ratio. The working potential U of the channeltron has to be adjusted at each temperature. Thus, if at room temperature U ≈ 1800 V, in order to compensate for the gradual decrease in the output pulse-height the working potential needs to be changed to about 2300 V at 4.2 K. The technique is characterized by the record effect value on $^{119}$Sn of 2000 % when using a source of $Ca^{119m}SnO_3$ and an absorber of $^{119}SnO_2$ at 4.2 K. The high sensitivity of such spectrometers results in a high sensitivity to the presence of resonant atoms. Thus, it has been shown in [3.179] that for $^{197}$Au (E = 77.3 keV) the CEM spectrum at 4.2 K is of substantially higher quality than the corresponding transmission spectrum. Advantages of the best CEM spectrometers with channeltrons involve their easy sample access, high cooling rate, capability of simultaneous transmission measurements and adaptability to on-line experiments [3.178].

To increase the count rate, detection efficiency or the effect value, a bias potential is sometimes applied to the sample or to the input of a channeltron. The statistical quality of spectra is, as a rule, nearly as good as for the gas-filled ionization detectors. The effective technique of collecting secondary electrons by applying a bias potential between the sample surface and a channeltron has been used [3.180] to develop a spectrometer for low temperature measurements (see Fig.3.68). The beam of $\gamma$-quanta is incident at 45° to the sample surface. The sample is the first electrode in a system of electrodes used to attract the secondary electrons to the entrance of channeltron and to accelerate them to an energy corresponding to the maximum detection efficiency.

Instead of channeltrons, microchannel plates are sometimes used. These are an array of miniature channel electron multipliers with plates of a large total area. Microchannel plates often have a hole in the centre for the direct beam of $\gamma$-quanta to pass through. Such microchannel plates have been used, in particular, for studies of various angular dependences [3.181] and in DCEMS [3.62,69,182]. At the same time, as compared with channeltrons, the use of microchannel plates may require longer measuring times to accumulate a statistically reliable spectrum. This is because of the larger total area of the inner walls of multiplication tube channels in comparison with a channeltron of an appropriate entrance diameter. This results in an enhanced efficiency of microchannel plates in detecting $\gamma$-radiation [3.183].

In Monte Carlo simulations an electron is usually considered to be absorbed by the solid when its energy has dropped to the I value (see Sect.3.1). Actually, these very low energy electrons (below 50 eV) - secondary electrons will be present in the sample and the mean free path between collisions for electrons with an energy below 10 eV may be about 10 nm. Thus, the secondary electrons may also escape the surface of the sample under study. In Mössbauer spectroscopy these electrons may be assumed to be produced by the scattering

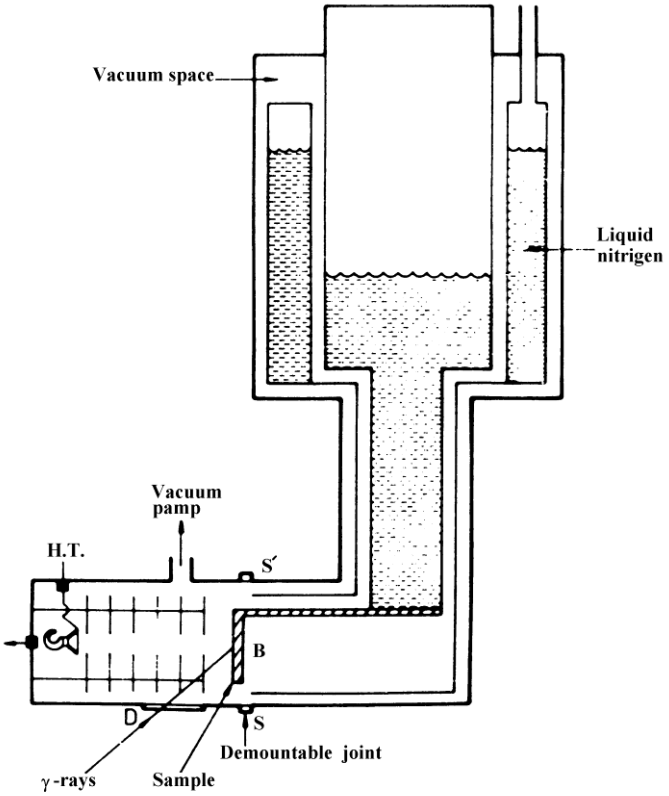


Fig.3.68 CEMS spectrometer used to operate at 4.2 K (from [3.180]).

and absorption of higher-energy electrons including the K-shell conversion, KLX-Auger electrons and LMY-Auger electrons.

If resonant scattering does not produce directly a number of very low energy electrons in the near-surface layer then the detection of such electrons leads to the thickness of the analyzed surface layer being approximately the same as that derived from conventional integral CEMS.

It was reported that the number of very low energy electrons may be considerable. There is an intensity maximum at $\approx$ 5 eV and Mössbauer spectra recorded with the electrons practically do not differ from the spectra in conventional CEMS [3.184,185]. Unfortunately, the authors have not made serious attempts at studies of the nature of electrons with energy below 50 eV and their role in CEMS. However these papers and the subsequent experimental studies [3.186-189] stimulated the interest to the method which is abbreviated as LEEMS (Low Energy Electron Mössbauer Spectroscopy).

Up to now when considering resonantly excited $^{57}$Fe nuclei only atomic relaxation processes which start with the ejection of K- or L- (rarely, M-shell) conversion electrons followed by Auger electrons or by X-rays were discussed (see Fig.3.69). Conversion electrons, KLL, KLM and KMM Auger electrons, photo- electrons and Compton-scattered electrons which are produced by $\gamma$-rays (with the energy above several hundred eV) in this context may be regarded as "high energy" electrons emitted by the atom. Secondary electrons result from the interaction of the above electrons with matte

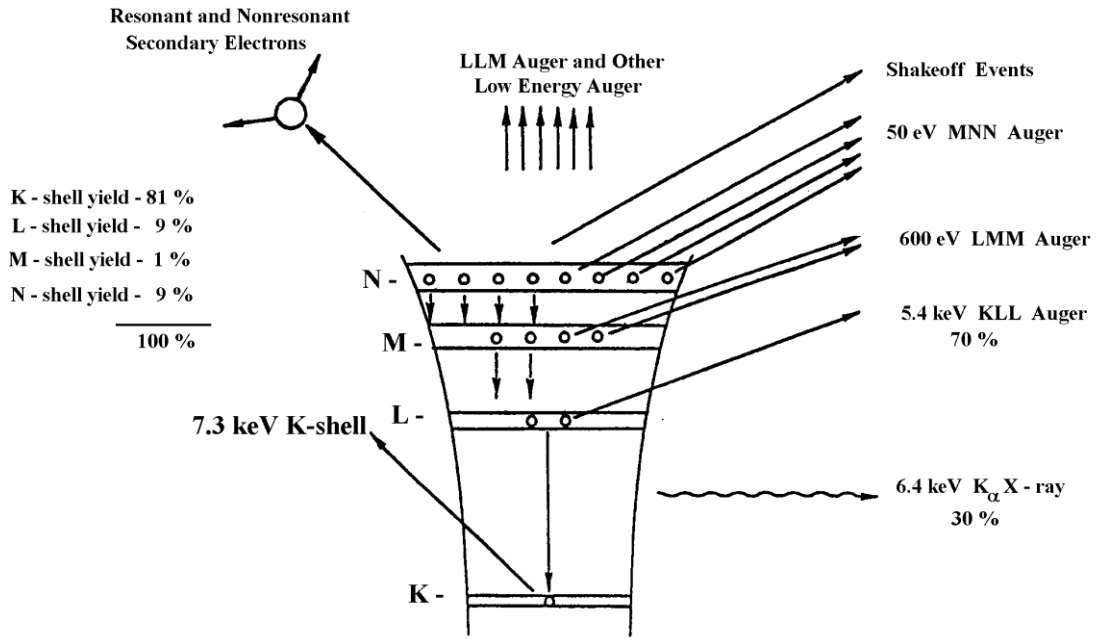


Fig.3.69 Diagram showing one possible electronic relaxation pathway following K-shell internal conversion. Note that one internal conversion can result in 8 ionizations [3.191].

Besides, there are electrons which are primarily produced with a very low energy. Two processes contribute to the intensity of the electrons. These are very low energy Auger electrons (LMM, MMM, MMN) and shake-off electrons. The atomic relaxation process following the Mössbauer effect has been investigated by LEE, ZABINSKI and TATARCHUK [3.190], ZABINSKI and TATARCHUK [3.191] and by LILJEQUIST and LANG [3.192] by means of a theoretical consideration, a simulation procedure and experimental investigations. Following internal conversion and, possibly, shake-off events,further relaxation is possible either through Auger transitions or X-ray fluorescence. Any vacancy filled by an Auger transition creates two new vacancies (see Fig.3.69) which may subsequently relax via an Auger transition. The Auger cascade is responsible for a multiplication of the low energy electron signal. The probability of shake-off events and the effect of orbital depletion were also calculated in [3.191] for each transition in the Auger cascade. The results of the simulation of 50 000 nuclear decays were recorded either for the specimen to be composed of isolated atoms or for the specimen in which approximations were made to ascribe metallic character to the specimen. ZABINSKI and TATARCHUK demonstrated (see Table 3.8) that shake-off electrons and very low energy Auger electrons are about 20 % of the total resonant signal. Six electrons, on the average, are ejected from each isolated relaxing atom and 7.2 electrons are ejected into continuum per internal conversion event in metallic iron. From the Table 3.8 it follows that in an isolated atom 75 % of electrons below 15 eV are the result of shake-off events and 25 % are the result of

**Table 3.8.**
Electron origination energy vs electron origin [3.188]

| Electron energy, eV | Electron origin | Probability, % | |
|---|---|---|---|
| | | Isolated atom | Metallic iron |
| 0- 15 | MMM, shake-off* | 20.0(75:25)** | 23.5(83:17)** |
| 29- 100 | MMM,MMN,Shake-off* | 32.1(6:94)** | 33.9(5:95)** |
| 50- 800 | LMM | 22.3 | 19.8 |
| 5400-7000 | KLL | 9.69 | 8.62 |
| 7300 | K-shell conversion | 14.1 | 12.5 |
| 13600 | L-shell conversion | 1.58 | 1.39 |
| 14400 | M-shell conversion | 0.19 | 0.18 |
| | | 100.0 | 100.0 |

* Shake-off electrons produced concurrently from one of the higher energy electrons/events
** Fraction of these electrons produced by (shake-off: Auger).

Auger transitions. Most of the low energy Auger electrons have the energy below 100 eV, and most of the shake-off electrons have the energy below 15 eV.

Experimental data [3.62,185,189,193] show a sharp peak in the number of electrons (related to Mössbauer events) at energies below 20 eV. To develop procedures for recording Mössbauer spectra it was first necessary to collect energy- dispersive and depth-selective spectra from "standard" specimens of known composition and thickness. The standard specimen must have a thin, chemically distinct surface layer where scattering and attenuation within the layer were minimal. A bulk-like signal was required for comparison with the surface signal and to determine the behavior of low-energy electrons generated exclusively by multiple scattering. The "standard specimen", therefore, was fabricated [3.186-189] from a naturally enriched bulk metallic iron foil with a very thin overlayer of $^{57}$Fe oxides on the surface, as shown in Fig.3.70. The signal-to-noise ratio was calculated and measured at first for the films and samples with a 1.0 nm thick overlayer on the $\alpha$-Fe substrate. For this purpose a CEM spectrometer was constructed with seven electron detectors based on the spiraltron electron multiplier, the entrance diameter being 2.54 cm. The 1 nm thick surface layer of $^{57}$Fe was oxidized in air and thereby chemically labelled as $Fe^{3+}$. The ratio of the area under the spectrum from this layer to the area under the spectrum from the substrate was 1.43. Studies of the dependence of this ratio and absolute intensities of electron beams produced by resonant and non-resonant processes allowed the

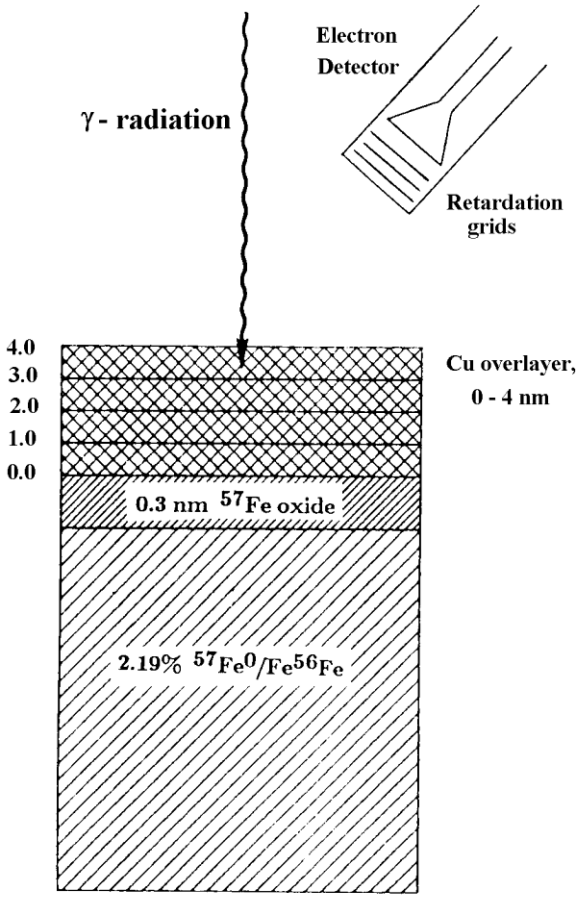


Fig.3.70 Schematic diagram of one of the "standard specimens" used by Zabinski and Tatarchuk and consisting of a 2 mm thick iron foil with a 95 % enriched 0.3 nm $^{57}$Fe oxide coating (from [3.189] )

role of the low-energy electrons generated as a result of resonant scattering to be determined.

At a bias voltage of -15 V applied to a retarding grid of the detector the detected intensity is reduced by 50 %, and the relative contribution of the top $Fe^{3+}$ layer 1 nm thick into the total spectrum decreases by a factor of 2. A small positive bias potential results in an increase in the count rate by $\approx$ 30 %. A 5 nm copper overlayer vacuum evaporated onto the sample proved to be effective in preferential absorption of the electrons from the $Fe^{3+}$ overlayer. Thus, electrons with E < 15 eV appear to supply information on a surface layer to a depth of $\approx$ 5 nm.

It is known [3.67,72,89,193] that by detecting LMM-Auger electrons in CEMS, the thickness of the analyzed layer may be made very small. This is about the thickness which is obtained by recording very low energy electrons, but the intensity is lower and more sophisticated equipment is needed. It was a reason why this method is not commonly used now.

Thus, the resonant very low energy electrons which are detected in CEMS provide surface-specific signals which decrease exponentially with application of metallic

overlayers up to 5.0 nm in thickness. The intensity of other very low energy electrons, arising from straggling and multiple- scattering events deep within the sample, decrease only slightly with the overlayer thickness. The detection of very low energy electrons offers the advantage of short data acquisition times ( about 77 % of the electrons emitted from the Fe atom are low energy Auger and shake-off electrons), and increased surface sensitivity compared to established procedures relying on the collection of electrons near 7.3 keV.

Considered above in Sections 3.2-3.8 methods of deconvolution of spectra obtained by collecting "high" energy electrons in relatively narrow energy intervals may not be directly applicable to very low energy electrons. However, adaptations of these methods permitted deconvolution of CEMS data collected from very low energy electrons whose intensities decay exponentially with depth [3.189]. These electrons may be used to obtain depth profiles of layers between the surface and 5.0 nm by determining the exponential functions which describe their intensity as a function of depth below the surface. Linear combinations of the attenuation functions may be used to depth deconvolute spectra arising from layers at various depths. Deconvolution procedures relying on K-conversion electrons from $^{57}$Fe require long collection times due to the smaller number of electrons available in the 6.4 - 7.3 keV range. Experimentally [3.194], the LEEMS intensity was found to be about 6 times that of DCEMS.

The weight functions when the detection of very low energy electrons is taken into account were elaborated in [3.192] The effect of detector characteristics and detector arrangements were also taken into account. The weight functions which are more analogous to the "conventional" DCEMS weight functions arise by the selection of very low energy electrons of different energies, as has been shown experimentally by ZABINSKI and TATARCHUK [3.189]. A theoretical recipe for the accurate determination of a weight function of interest in general appears to be difficult, due to the complex tangle of electrons of many different origins, the material-dependent variations in the secondary electrons generation and the complexity of the description of electron scattering at these very low energies. By comparison, the weight functions of "conventional" CEMS and DCEMS can at present be computed considerably more accurately [3.192].

## References

3.1 I.M. Bronschtein and B.C. Frayman, Vtorichnaya Electronnaya Emissiya, Nauka, Moskva, 1969, p. 407.
3.2 J.I. Goldstein and H. Yakowitz (eds.), Practical Scanning Electron Microscopy, Plenum Press, New York, 1975.
3.3 S.A. Vorob'ev, Prohozdenie β-Chastiz cherez Kristalli, Atomizdat, Moskva, 1975, p. 142.
3.4 B.J. Tatarchuk and J.A. Dumestic, in Chemistry and Physics of Solid Surfaces, Vol. 5, Springer, Berlin, 1984.

3.5 Yu.F. Babikova, P.L. Gruzin and Yu.V. Petrikin, Electronnaya NGR-Spectroscopiya, Moscov. Injener.-Fiz. Institut, Moskva, 1985.
3.6 V.E.Cosslett and R.N. Thomas, Brit. J. Appl. Phys., 15 (1964) 1283-1300.
3.7 V.E. Cosslett and R.N. Thomas, Brit. J. Appl. Phys., 16 (1965) 779-791.
3.8 P.L. Gruzin, Yu.V. Petrikin and A.M.Rodina, Atomnaya Energiya, 38, No.3 (1975) 165.
3.9 D. Liljequist, Electron Penetration in Solids and its Application to Mössbauer Spectroscopy, Thesis, University of Stockholm, 1979 p. 64.
3.10 M.Grozdanov, Ts. Bonchev and V. Lilkov, Nucl. Instr. Meth., 165 (1979) 231-236.
3.11 Ts. Bonchev, M.Grozdanov and L. Stoev, Nucl. Instr. Meth., 165 (1979) 237-241.
3.12 H.A. Bethe, Ann. Phys. (Leipzig), 5 (1930) 325-337.
3.13 D. Liljequist, J. Phys. D: Appl. Phys., 10 (1977) 1363-77.
3.14 D. Liljequist, J. Phys. D: Appl. Phys., 11 (1978) 839-858.
3.15 D. Liljequist, T. Ekdal and U. Baverstam, Nucl. Instr.Meth., 155 (1978) 529-538.
3.16 A.P. Minkova, B.D.Slavov and Tz. Bonchhev, Bulg. J. Phys., 2, No. 6 (1975) 592-601.
3.17 A. Proykova, A. Minkova, B. Slavov and Tz. Bonchev, Bulg. J. Phys., 5, No. 3 (1978) 248-259.
3.18 D. Liljequist and M. Ismail, Nucl. Instr. Meth. Phys. Res., A239 (1985) 273-280.
3.19 T.S. Lee and B.J. Tatarchuk, Hyperfine Interactions, 42 (1988) 1149-1152.
3.20 W. Bothe, Z. Phys., 54 (1929) 161-173.
3.21 H. Bethe, M. Rose and L. Smith, Proc. Am. Phil. Soc., 78 (1938) 573-585.
3.22 V.E. Cosslett and R.N. Thomas, in The Electron Microprobe, ed. by T.D. McKinley, K.F.J. Heinrich, D.B. Wittry and N.Y.Willey, New York, 1966, pp. 248-268.
3.23 K. Siegbahn (ed.), Alpha-, Beta-, and Gamma-Ray Spectroscopy, North Holland, Amsterdam, 1966.
3.24 K.P. Mitrofanov and V.S. Shpinel, Zh. Eksp. Teor. Fiz., 40 (1961) 983-987.
3.25 E.F. Kankeleit, Z. Phys., 164 (1961) 422.
3.26 Zw. Bonchev, A. Jordanov and A. Minkova, Nucl. Instr. Meth., 70 (1969) 36-40.
3.27 J.J. Spijkerman, J.C. Travis, P.A. Pella and J.R. DeVoe, NBS Technical Note, 541 (1971) 65.
3.28 J.J. Spijkerman, in Mössbauer Effect Methodology, ed. by I.J. Gruverman, Vol. 7, Plenum Press, New York, 1972, pp. 85-96
3.29 G. Weyer, in Mössbauer Effect Methodology, ed. by I.J. Gruverman and C.W. Seidel, Vol. 10, Plen. Publ. Corp., New York, 1976, pp. 301-319.
3.30 R.A. Krakowski and R.B. Miller, Nucl. Instr. Meth., 100 (1972) 93-105.
3.31 S. Valkealahti and R.M. Nieminen, Appl. Phys., A32 (1983) 95-100.
3.32 G.P. Huffman, in Mössbauer Effect Methodology, ed. by I.J. Gruverman and C.W. Seidel, Vol. 10, Plenum Press, New York
1976, pp. 209-214.
3.33 M. Ismail and D. Liljequist, Hyperfine Interactions, 29 (1986) 1509-1512.
3.34 D. Liljequist, Nucl. Instr. Meth., 179 (1981) 617-619.
3.35 J.D. Martinez and J. Parelada, Nucl. Instr. Meth. Phys. Res., B6 (1985) 547-551.
3.36 T. Toriyama, K. Saneyoshi and K. Hisatake, J. de Physique, 40, suppl. No.3 (1979) C214-16.

3.37 F.A. Deeney and P.J. McCarthy, Nucl. Instr. Meth., 166 (1979) 491-495
3.38 D. Liljequist, The theoretical prediction of bulk and surface phase signals as functions of surface layer thickness, Stockholm USIP Report, October (1980) 80-107.
3.39 F. Salvat and J. Parellada, Nucl. Instr. Meth. Phys. Res., B1 (1984) 70-84.
3.40 T.S. Lee, T.D. Placek, J.A. Dumestic and B.J. Tatarchuk, Nucl. Instr. Meth. Phys. Res., B18 (1987) 182-193.
3.41 U.Bäverstam, C. Bohm, R. Ringstrom and T. Ekdahl, Nucl. Instr. Meth., 108 (1973) 439-443.
3.42 U. Bäverstam, T. Ekdahl, C. Bohm, B. Ringstrom, V. Stefansson and D. Liljequist, Nucl. Instr. Meth., 115 (1974) 373-380.
3.43 U. Bäverstam, T. Ekdahl, C. Bohm, D.Liljequist and B. Ringstrom, Nucl. Instr. Meth., 118 (1974) 313-316.
3.44 T. Toriyama, M. Kikawa, M. Fujioka and K. Hisatake, Japanese Journ. Appl. Phys. Suppl. 2, part 1, (1974) 733- 736.
3.45 P.L. Gruzin, Yu. V. Petrikin and R.A. Stukan, Prib. Tekh.Eksp., No. 3 (1975) 48-49.
3.46 J.P. Schunk, J.M. Friedt and Y. Ljabador, Revue de Physique Appliq., 10 (1975) 121-126.
3.47 T. Bressani, P. Macciotta, G. Puddu and S. Serci, in Application of the Mössbauer Effect, ed. by Yu.M. Kagan and I.S. Lyubutin, Vol. 2, Gordon and Breach Scie. Publ., Amsterdam, 1985, pp. 755-760.
3.48 H.M. Van Noort, F.J. Ferguson, C.J.G. Verwer, A.A. van Gorcum, J.M.E. van Laarhoven and C.J.M. Denissen, Nucl. Instr. Meth. Phys. Res., B34(3) (1988) 391-395.
3.49 U. Bäverstam, C. Bohm, T. Ekdahl, D. Liljequist and B. Ring- strom, in Mössbauer Effect Methodology, ed. by I.J. Gruverman and C.W. Seidel, Vol. 9, Plenum Press, New York, 1974, pp. 259-276.
3.50 D. Liljequist and T. Ekdahl, Computation of weight functions or Depth Selective Conversion Electron Mössbauer Spectroscopy, Stockholm USIP Report (1978) 78-17.
3.51 Ch. Sauer, A. Holzwarth, Zs. Kajcsos and W. Zinn, Nucl. Instr. Meth., B34 (1988) 377-382.
3.52 J. Itoh, T. Toriyama, K. Saneyoshi and K. Hisatake, Nucl. Instr. Meth., 205 (1983) 279-286.
3.53 D. Liljequist, Scanning Electron Microscopy, Sem. Inc. AMF O-Hare, Chikago, 1983, pp. 997-1017.
3.54 D. Varga, I. Kadar, A. Kover, I. Cserny, G. Morik, V. Brabec, O. Dragoun, A. Kovalik and J. Adam, Nucl. Instr. Meth., 192 (1982) 277-286.
3.55 Ch. Briançon, B. Legrand, R.J. Walen, Ts. Vylov, A. Minkova and A. Inoyatov, Nucl. Instr.Meth., 221 (1984) 547-557.
3.56 U. Bäverstam, B. Bodlung-Ringstrom, C. Bohm, T. Ekdahl and D. Liljequist, Nucl. Instr. Meth., 154 (1978) 401-403.
3.57 N. Benczer-Koller and B. Kolk, in Workshop on New Directions in Mössbauer Spectroscopy - 1977, ed. by G.J. Perlow, AIP Conf. Proceed. Vol. 38, Amer. Inst. Phys., New York, 1977, p. 107.
3.58 T. Yang, B. Kolk, T. Kachowski, J. Trooster and N. Benczer-Koller, Nucl. Instr. Meth., 197 (1982) 545-556.

3.59 I.P. Jain, Y.K. Vijay, L.K. Malhotra, A. Verma and R. Chandra, Hyperfine Interactions, 35 (1987) 1045-1048.
3.60 J. Parellada, M.R. Polcari, K. Burin and G.M. Rothberg, Nucl. Instr. Meth., 179 (1981) 113-118.
3.61 T. Shigematsu, H.D. Pfannes and W. Keune, Phys. Rev. Lett., 45 (1980) 1206-1209.
3.62 V.Yu. Ryzhykh, M.I. Babenkov, B.V. Bobykin, V.S. Zhdanov and A.K.Zhetbaev, Nucl.Instr.Meth. Phys.Res., B47 (1990) 470-473.
3.63 T. Toriyama, K. Saneyoshi, J. Itoh and K. Hisatake, Nucl. Instr. Meth. Phys. Res., B4 (1984) 170-185.
3.64 J. Korecki and U. Gradmann, Hyperfine Interactions, 28 (1986) 931-934.
3.65 J. Parellada, M.R. Polcari, K. Burin and G.M. Rothberg, Nucl. Instr. Meth., 118 (1974) 313.
3.66 H.M. Van Noort and A.A. van Gorkum, J. Phys., E21(6) (1988) 587-91.
3.67 Z.M. Stadnik, H.R. Borsje, A.E.M. Swolfs, W.H.A. Leenders and J.C. Fuggle, Rev. Sci. Instrum., 60(4) (1989) 708-12.
3.68 P. Auric, A. Baudry, M. Boge, J. Rocco and L. Trabut, Hyperfine Interactions, 58 (1990) 2491-2496.
3.69 B. Stahl, G. Klingelhöfer, H. Keller, Th. Reitz and E. Kankeleit, Hyperfine Interactions, 58 (1990) 2547-2554.
3.70 S.C. Pancholi, H. De Waard, J.L.W. Petersen, A. Van der Wijk and J. van Klinken, Nucl. Instr. Meth., 221 (1984) 577-581.
3.71 T. Shigematsu, H.D. Pfannes and W. Keune, in Mössbauer spectroscopy and its chemical applications, ed. by J.G. Stevens and G.K. Shenoy, Advances in chemistry series, Vol.194, American Chemical Society, p.125.
3.72 M.Domke, B.Kyvelos and G.Kaindl, Hyperfine Interactions, 10 (1981) 1137-1142.
3.73 V.P. Alekseev, M.V. Lokhanin and R.A. Stukan, Prib. Tekh.Eksp., No.8 (1988) 37-40 / Instrum. Exsp. Tech. (Engl. Transl.), 1(3) (1988) 554-8.
3.74 C. Song, J. Trooster and N. Benczer-Koller, Phys. Rev. B9 (1974) 3854-3863.
3.7| T. Yang, J. Trooster, T. Kachnowskii and N. Benczer- Koller, Hyperfine Interactions, 10 (1981) 795-800.
3.7| Ts. Bonchev, A. Minkova, G. Kushev and M. Grozdanov, Nucl. Instr. Meth., 147 (1977) 481-486.
3.7| A. Proykova, Bulg. J. Phys., 6 (1979) 28-37.
3.7| T. Yang, A. Krishnan, N. Benczer-Koller and G. Bayreuther, Phys. Rev. Lett., 48 (1982) 1292-1295.
3.7| D. Liljequist, M. Ismail and T. Ekdahl, A Monte Carlo study of the effects of energy resolution and angular selection in Conversion Electron ME Spectroscopy, Stockholm USIP Report 83-09 (1983) 32.
3.|| A. Proykova, Nucl. Instr. Meth., 174 (1980) 327-329.
3.8| P. Topalov and A. Proykova, Nucl. Instr. Meth. Phys. Res., A236 (1985) 142-144.
3.8| D. Liljequist and M. Ismail, Phys. Rev., B31 (1985) 4131.
3.83 D. Liljequist, K. Saneyoshi, K. Debusmann, W. Keune, R.A. Brand, W. Kiauka and M. Ismail, Phys. Rev., B31 (1985) 4137.
3.8| D. Liljequist, T. Ekdahl and U. Bäverstam, Nucl. Instr. Meth., 155 (1978) 529-538.

3.8| D. Liljequist and B. Bodlung-Ringström, Nucl. Instr. Meth., 160 (1979) 131-136.
3.8| D. Liljequist, C. Bohm and T. Ekdahl, Nucl. Instr. Meth., 77 (1980) 495-497.
3.8| D. Liljequist and C. Bohm, GAIN - An Interactive Computer Program for Data Analysis in Depth Selective Conversion Electron Mössbauer Spectroscopy, Stockholm USIP Report 81- 06 (1981) 44.
3.8| G.N. Belozerskii, C. Bohm, T. Ekdahl and D. Liljequist, Nucl. Instr. Meth., 192 (1982) 539-543.
3.|| K. Saneyoshi, K. Debusmann, W. Keune, R.A. Brand and D. Li- ljequist, in Industrial Applications of the Mössbauer Effect, ed. by G.C. Stevens and C.J. Long, Plenum Press, New York, 1987, pp. 121-136.
3.|| M. Takafuchi, Y. Isozumi and R. Katano, Bull. Inst. Chem. Res. Kyoto Univ., 51, No.1 (1973) 13-18.
3.|| Y. Isozumi, D.I. Lee and I. Kadar, Nucl. Instr. Meth., 120 (1974) 23-28.
3.|| Y. Isozumi and M. Takafuchi, Bull. Inst. Chem. Res. Kyoto Univ., 53, No. 1 (1975) 63-67.
3.|| Y. Isozumi, M. Kurakado and R. Katano, Nucl. Instr. Meth., 166 (1979) 407-410.
3.9| Y. Isozumi, M. Kurakado and R. Katano, Rev. Sci. Instr., 52 (1981) 413-418.
3.9| Y. Isozumi, M. Kurakado and R. Katano, Nucl. Instr. Meth., 204 (1983) 571-575.
3.9| C.M. Yagnik and R.A. Mazak, Nucl. Instr. Meth., 144 (1974) 1-4.
3.9| M.J. Tricker and J.M. Thomas, Surf. Sci., 45 (1974) 601- 608.
3.9| J.M. Thomas, M.J. Tricker and A.P. Winterbottom, J. Chem. Soc. Faraday Trans., II, 71 (1975) 1708-1719.
3.9| M.J. Tricker, A.G. Freeman, A.P. Winterbottom and J.M. Thomas, Nucl. Instr. Meth., 135 (1976) 117-124.
3.||| M.J. Tricker, L.A. Ash and T.E. Cranshaw, Nucl. Instr. Meth., 143 (1977) 307-309.
3.101 M. Takafuchi and T. Kobayashi, Nucl. Instr. Meth. Phys. Res., B9 (1985) 223-228.
3.102 J.A. Sawicki, B.D. Sawicka and J. Stanek, Nucl. Instr.Meth., 138 (1976) 565-566.
3.103 J. Sawicki, Nucl. Instr. Meth., 152 (1978) 577-578.
3.104 J. Sawicki, J. Stanek, J. Kowalski and B.D. Sawicka, Nucleonika, 24 (1979) 1161-1167.
3.105 M. Inaba, H. Nakagawa and Y. Ujihira, Nucl. Instr. Meth., 180 (1981) 131-135.
3.106 H. Nakagawa, Y. Ujihira and M. Inaba, Nucl. Instr. Meth., 196 (1982) 573-574.
3.107 A.I. Chumakov, A.B. Dubrovin and G.V. Smirnov, Nucl. Instr. Meth., 216 (1983) 505-509.
3.108 V.V. Nemoshkalenko, Yu.V. Glushko, O.N. Razumov and N.A. Tomashevskii, Prib. Tekh. Eksp., No.5 (1983) 39-41.
3.109 V.V. Nemoshkalenko, O.N. Razumov and N.A. Tomashevskii, in Application of the Mössbauer Effect, ed. by Yu.M. Kagan and I.S. Lyubutin, Vol. 2, Gordon and Breach Scie. Publ., Amsterdam, 1985, pp. 807-812.
3.110 D.C. Cook and E. Agyekum, Nucl. Instr. Meth., 12 (1985) 229.
3.111 D.C. Cook, Hyperfine Interactions, 29 (1986) 1463.
3.112 D. Bodin and J.P. Eymery, Nucl. Instr. Meth., 16 (1986) 424.
3.113 S. Kishimoto, S. Isozumi, R. Katano and H. Takekoshi, Nucl. Instr. Meth. Phys. Res., A249 (1986) 349-353.

3.114 Y. Isozumi, S. Kishimoto, R. Katano and H. Takakoshi, Rev. Sci. Instr., 58 (1987) 293.
3.115 S. Kishimoto, Y. Isozumi, R. Katano and H. Takakoshi, Nucl. Instr. Meth. Phys. Res., A262 (1987) 413-418.
3.116 R. Katano, T. Fujii, T. Kobayashi, K. Fukumura and Y. Isozumi, Nucl. Instr. Meth. Phys. Res., A280(2-3) (1989) 2857.
3.117 Y. Isozumi, S. Ito, T. Fujii and R. Katano, Rev. Sci. Instrum., 60(10) (1989) 3262-4.
3.118 X-Z Zhou and A.H. Morrish, Nucl. Instr. Meth. Phys. Res., B18 (1987) 215-219.
3.119 A. Kastner, G. Lugert and G. Bayreuther, Hyperfine Interactions, 42 (1988) 1145-1148.
3.120 U. Fano, Phys. Rev., 72 (1947) 26-37.
3.121 E. Mathieson and P.W. Sanford, Proc. Intern. Symposium on Nuclear Electronics, Paris, 1963 (ENEA 1964), p. 65.
3.122 V.P. Lazutkov and E.M. Lotvinov, Prib. Tekh. Eksp., No.3 (1988) 59.
3.123 L. May and D.K. Shediker, Nucl. Instr. Meth., 55 (1967) 183-188.
3.124 G.D. Alkhazov, A.P. Komar and A.A. Vorob'ev, Nucl. Instr. Meth., 48 (1967) 1-12.
3.125 G.D. Alkhazov, Nucl. Instr. Meth., 89 (1970) 155-165.
3.126 G.D. Alkhazov, Jurnal Tehn. Fiz., 16, No. 12 (1971) 2513- 2523.
3.127 M.W. Charles and B.A. Cooke, Nucl. Instr. Meth., 61 (1968) 31-36.
3.128 H. Sipila, Nucl. Instr. Meth., 133 (1976) 251-252.
3.129 M.L. Jarvinen and H. Sipila, Nucl. Instr. Meth., 193 (1982) 53-56.
3.130 G.U. Nienhaus, F. Drepper, F. Parak, R.L. Mössbauer, D. Bade and W. Hoppe, Nucl. Instr. Meth. Phys. Res., A256 (1987) 561-586.
3.131 G. Charpak, Nucl. Instr. Meth., 196 (1982) 1-9.
3.132 G. Bibbo and P.W. Sanford, Nucl. Instr. Meth., 179 (1981) 189-194.
3.133 Y. Yonekura, T. Toriyama, J. Itoh and K. Hisatake, Hyperfine Interactions, 15/16 (1983) 1005-1008.
3.134 I.K. Solomin and M.F. Kruglov, Fiz. Tverd. Tela, 26 (1984) 519-523.
3.135 A.I. Chumakov and G.V. Smirnov, Zh. Eksp. Teor. Fiz., 89 (1985) 1810. [Sov. Phys. JETP 62 (1985) 1044].
3.136 A.I. Chumakov, G.V. Smirnov, M.V. Kruglov and I.K. Solomin, Phys. Stat. Sol. (a), 98, No. 1 (1968) 11-25.
3.137 A.I. Chumakov and G.V. Smirnov, Nucl. Instr. Meth. Phys. Res., B28(2) (1987) 307-310.
3.138 U. Gonser, P. Schaaf and F. Aubertin, Hyperfine Interactions, 66, No. 1-4 (1991) 95-100.
3.139 P. Schaaf, A. Kramer, L. Blaes, G. Wagner, F. Aubertin and U. Gonser, Nucl. Instr. Meth. Phys. Res., B53, No. 2 (1991) 184-88.
3.140 P. Schaaf, A. Kramer, F. Aubertin and U.Gonser, Zeitschrift fur Metallkunde, 82, No. 11 (1991) 815-19.

3.141 A.S. Kamzin and L.A. Grigor'ev, Sov. Techn. Phys. Lett., 16, No. 8 (1990) 616-17. (Translation of Pis'ma v Zhurnal Tekhnicheskoi Fiziki, Vol. 16, Iss. 15-16 (1990) 38-41).
3.142 A.S. Kamzin and L.A. Grigor'ev, Soviet Physics - Technical Physics, Vol. 35, Iss. 7 (1990) 840-3. (Transl. of Zhurnal Tekhnicheskoi Fiziki, Vol. 60, Iss. 7 (1990) 151-6).
3.143 A.S. Kamzin and L.A.Grigor'ev, Instruments and Experimental Techniques, Vol. 34, No. 2 (1991) 307-10. (Transl. of Pribory i Tekhnika Eksperimenta, Vol. 34, Iss. 2 (1991) 74-7).
3.144. J.C.Frost, B.C.C.Cowie, S.N.Chapman and J.F.Marshall, Appl. Phys.Lett., 47(6) (1985) 581.
3.145. G.N.Belozerski, V.G. Semenov and A.Y.Sokolov, |V Vsesouznoe soveschanie po kogerentnomu vzaimodeystviu izluchenii s veschestvom, Latviyskaya SSR, Urmala, 1988, Proceed. of Conf., Moskva, 1988, p.236.
3.146. R.V.Pound and W.T.Vetterling, Journ. de Phys., C2, 40 (1979) 2.
3.147 M.A. Andreeva, G.N.Belozerskii, S.M.Irkaev, V.G.Semenov, A.Yu. Sokolov and N.V. Shumilova, Phys. Stat. Sol., Vol. A127, No. 2 (1991) 455-64.
3.148 M.A.Andreeva, G.N.Belozerskii, O.V. Grishin, V.G. Semenov, S.M. Irkaev and V.I. Nikolaev, JETP Letters, Vol. 55, Iss. 1 (1991) 63-6. (Transl. of Pis'ma v Zhurnal Eksperimental'noi i Teoreticheskoi Fiziki, Vol. 55, Iss. 1, Date: 10 Jan. 1992, pp.62-5).
3.149 R.S.Becker, J.A.Golovchenko and J.R. Patel, Phys.Rev.Lett., 50 (1983) 153.
3.150. I.K. Solomin and M.F. Kruglov, Fizika Tverdogo Tela, 26 (1985) 519.
3.15| J. Christiansen, P. Hindennach, U. Morfeld, E. Recknagel, D. Riegel and G. Weyer, Nucl. Phys. A99 (1967) 345.
3.15| S. Damgaard, M. Oron, J.W. Petersen, Yu. V. Petrikin and G. Weyer, Phys. Stat. Sol. (a), 59 (1980) 63-67.
3.15| Yu.V. Petrikin, V.N. Alekseev and V.A. Bychkov, Zavodskaja Laboratoria, No. 11 (1983) 46-48.
3.154 Yu. Babikova, O.M. Vakar, A.A. Kasimovskii and Yu.V. Petrikin, Prib. Tekhn. Eksp., No.3 (1983) 40-43.
|.|5| Yu.V. Petrikin, Yu.V. Baldokhin, A.A. Kiselev and A.P. Kuprin, Prib. Tekh. Eksp., 2 (1989) 81-85 / Instrum. Exp. Tech. (Engl. Transl.), 32(2) (1989) 344-8.
3.156 J.R. Gancedo and M. Gracia, Hyperfine Interactions, 29 (1986) 1479-1482.
3.157 G. Weyer, Hyperfine Interactions, 58 (1990) 2561-2566.
3.158 K. Endo, A. Kato, M. Mizui and H. Sano, Proc. Intern. Conf. Appl. of the Mossb. Effect, Jaipur, India, December 1981, New Delhi, 1982, pp. 912-914.
3.159 B.I. Rogozev and D.A. Sarichev, in Application of the Mössbauer Effect, ed. by Yu.M. Kagan and I.S. Lyubutin, Gordon and Breach Scie. Publ., Amsterdam, 1985, pp.737- 741.
3.160 Zs. Kajcsos, Ch. Sauer, R.A. Brand, W. Zinn, R. Kurz, M.A. Ligtenberg and G. van Aller, Hyperfine Interactions, 46 (1989) 707-714.
3.161 V.S. Vartanov and B.G. Zemskov, Izmeritelnaja Tehnika, 3 (1987) 51-53.
3.162 V.S. Vartanov and B.G. Zemskov, Izmeritelnaja Tehnika, 2 (1988) 58-60./ Meas. Tech. (Engl. Transl.), 31(2) (1988) 58-61.
3.163 V.L. Gurachevskii, M. Mashlan, O.V. Misevich and A.L. Holmezkii, Prib. Tekhn. Eksp., No. 6 (1985) 31-35.

3.164 G.N. Belozerskii, Fizika Tverdogo Tela, 25, vip. 8 (1983) 2522-2524.
3.165 J.J. Bara and B.F. Bogacz, Nucl. Instr. Meth. Phys. Res., A238 (1985) 469-471.
3.166 J.J. Bara and B.F. Bogacz, Hyperfine Interactions, 29 (1986) 1575-1578.
3.167 Yi Qun Zhang, Jun Jie Zhu and Shi Jie Cao, Hyperfine Interactions, 29 (1986) 1505-1508.
3.168 J.L.W. Petersen, Nucl. Instr. Meth., 221 (1984) 582-585.
3.169 J.A.Sawicki, in Industrial Applications of the Mössbauer Effect, ed. by J.G.Stevens and C.J.Long, Plenum Press, New York, 1987, pp.83-120.
3.170 M. Carbucicchio, Nucl. Instr. Meth., 144 (1977) 225-229.
3.171 V.A. Bychkov, P.L. Gruzin, Yu.V. Petrikin and L.A. Sharova, Zavodskaja Laboratoria, 44, No.8 (1978) 970-973.
3.172 R. Oswald and M. Ohring, J. Vac. Sci. Technol., 13 (1976) 40-51.
3.173 J.A. Sawicki, T. Tyliszcak and O. Gzowski, Nucl. Instr. Meth., 190 (1981) 433-435.
3.174 O. Massenet, Nucl. Instr. Meth., 153 (1978) 419-421.
3.175 K.K. Kadyrzhanov, A.N. Ozernoi and V.Yu. Ryzhykh, in Application of the Mössbauer Effect, ed. by Yu.M. Kagan and I.S. Lyubutin, Vol. 2, Gordon and Breach Scie. Publ., Amsterdam, 1985, pp. 777-779.
3.176 V.A. Bychkov, R.V. Kopylov, Yu. V. Petrikin and S.Yu. Shirokinskii, Prib. Tekhn. Eksp., No. 2 (1988) 53-55.
3.177 J. Kowalski, J. Stanek, T. Tyliszczak and J.A. Sawicki, Nucl. Instr. Meth., 216 (1983) 299-301.
3.178 J.A. Sawicki, Nucl. Instr. Meth. Phys. Res., B16 (1986) 483-487.
3.179 J.A. Sawicki, T. Tyliszczak, J. Stanek, B.D. Sawicka and J. Kowalski, Nucl. Instr. Meth., 215 (1983) 567-568.
3.180 R. Atkinson and T.E. Cranshaw, Nucl. Instr. Meth., 204 (1983) 577-579.
3.181 A.P. Amuljavichus and R.Yu. Davidonis, Prib. Tekhn. Eksp., No. 3 (1986) 76-78.
3.182 H. Sato and M. Mitsuhashi, Hyperfine Interactions, 58 (1990) 2535-2540.
3.183 Yu.V. Petrikin, A.P. Krupin and A.A. Novakova, Vsesojuznoe Soveschanie po Prikladnoi Messbauerovskoi Spectroscopii "Volga", Sept. 2-7, 1988 (Moskovskii Injenerno-fizicheskii Institut, Moskovskii Gosud. Universitet), p.37.
3.184 T. Tyliszczak, J.A. Sawicki, J. Stanek and B.D. Sawicka, J. Phys. Colloq. (Paris), 41 (1980) C1-117.
3.185 J.A. Sawicki and T. Tyliszczak, Nucl. Instr. Meth., 216 (1983) 501.
3.186 J.S. Zabinski and B.J. Tatarchuk, Nucl. Instr. Meth. Phys., B31 (1988) 576-583.
3.187 J.S. Zabinski and B.J. Tatarchuk, Hyperfine Interactions, 41 (1988) 737-740.
3.188 J.S. Zabinski and B.J. Tatarchuk, Thin Solid Films, 166 (1988) 213-24.
3.189 J.S. Zabinski and B.J. Tatarchuk, Nucl. Instr. Meth. Phys. Res., B51 (1990) 41-52.
3.190 T.S. Lee, J.S. Zabinski and B.J. Tatarchuk, Nucl. Instr. Meth. Phys. Res., B30 (1988) 196-202.

3.191 J.S. Zabinski and B.J. Tatarchuk, Nucl. Instr. Meth. Phys. Res., B42(3) (1989) 379-88.
3.192 D. Liljequist and H. Lang, Nucl. Instr. Meth. Phys. Res., Sect.B., B52 (1990)
3.193 S. Stanek,T. Shigematsu, W. Keune and H.D. Pfannes, J. Magn. and Magnet. Mater., 35 (1983) 347.
3.194 G. Klingelhöfer and E. Kankeleit, Hyperfine Interactions, 58 (1990) 2547-2554.